ABSTRACT

Title of thesis:	DESIGN, FABRICATION, AND TESTING OF A CHITOSAN BASED OPTICAL BIOSENSOR
	Michael Annona Powers, Master of Science, 2006
Thesis directed by:	Associate Professor Reza Ghodssi
	Department of Electrical and Computer Engineering
	The Institute for Systems Research

This work presents the design, fabrication, and testing of an original concept for an optical biosensor device intended for use in a microfluidic network. The device uses planar waveguides intersecting a microfludic channel with biofunctionalized patterned sidewalls to detect biomolecules via fluorescent labeling. The optical-biological interface is provided through chitosan, a natural biopolymer derived from crab shells. Chitosan is electrodepositable, and this material platform was developed to enable spatially selective and temporally selective assembly of biospecies in the sensor using electrical signals. Several design concepts were evaluated against several design goals which are fundamental to lab-on-a-chip systems. The unique fabrication process flow integrates waveguides and microfluidic channels which are fabricated in a single step with a thick polymer layer on a Pyrex substrate. Key to the success of the device was the

development of a process to pattern indium tin oxide (ITO, a transparent semiconductor) on the sidewalls of deep (130 um) fluid channels. The device was tested in several modes of operation and the proof of concept was shown. The device could be adapted to sense proteins, enzymes, and other optically active bio components. Here, its application as a DNA hybridization sensor is demonstrated.

A FABRICATION PLATFORM FOR OPTICAL BIOMEMS USING CHITOSAN

By

Michael Annona Powers

Thesis submitted to the Faculty of the Graduate School of the
University of Maryland, College Park in partial fulfillment
of the requirements for the degree of
Master of Science
2006

Advisory Committee:

    Professor Reza Ghodssi, Chair
    Professor William Bentley
    Professor Gary Rubloff

DEDICATION

To My Family

ACKNOWLEDGEMENTS

TABLE OF CONTENTS

1 Introduction and Motivation

The development of the integrated circuit in the 1960s had a profound impact on computing and the way information is stored, processed, and communicated. Critical to this great innovation in information technology was the science of miniaturization- the scaling down of vacuum tubes into transistors, followed by the high density integration of millions of transistors on a single silicon chip. This is arguably the best example of the revolutionary effect that miniaturization can have in one particular industry and there has been much effort toward finding the next revolution in miniaturization. Information has no definite size, so there are clear advantages in handling information with micro-scale machines. In many ways, biomedicine is a prime candidate as it has characteristics very similar to information technology. Unlike information, biological components have definite size, albeit very small. Biological components operate on the molecular level, and thus can be manipulated in finer ways with smaller machines. Although existing techniques can manipulate biological components in large "test-tube" scales - akin to vacuum tubes - manipulating biological components with microfluidics on small scales – analogous to integrated circuits - may greatly expand our abilities in conducting biomedical research, clinical therapy, and pathogen detection. To fulfill this goal, it is necessary to develop platforms for "biofabrication" integrated with traditional microelectronic and MEMS approaches. The ideal platform would be controllable with electrical signals, robust, easy to functionalize with a wide range of active biospecies, highly transparent at visible wavelengths, and operable in water and at physiological conditions. This thesis develops an original method for using top-down lithography and electrically mediated assembly of bio-molecular components to create a biophotonic

sensor that can detect DNA, with future possibilities in detecting proteins and cellular functions. Components of the traditional techniques for biophotonics- such as cuvette based fluid analysis, "gene-chip" technology, and fiber-optic based "optrode" sensing are integrated by way of microfluidics on one microfabricated device.

1.1 Traditional Techniques for Biophotonics

Although there are many methods available for biosensing, using light to detect biospecies is an especially attractive option for several reasons. First, as stated in the introductory paragraph, biological components are small and the smallest tools are necessary to interact with biology at the molecular level. Light can be guided and focused to interact with small volumes. Furthermore, molecules can be engineered to interact with light in specific ways. Second, photonic approaches are inherently non-contact. Avoiding direct contact with material other than what is inert (glass, elastomers, etc.) is highly advantageous because it alleviates the risks of bio-fouling, bio-incompatibilities, contamination, and other practical problems. Third, most biology takes place in aqueous environments, which has wide wavelength windows that are transparent to visible and IR light. Water creates damping in mechanical systems and conduction in electrical systems. These effects can pose operational difficulties. Fourth, there is an extensive array of light manipulation tools developed for telecommunications applications that can be adapted to biophotonic applications. High sensitivity photodetector technology and sophisticated optics has enabled single (or a few) molecules to be detected under near ideal conditions. [1, 2, 3, 4] Additionally, a wide range of specific light-interacting chemistries has already been developed and commercialized by companies such as Molecular Probes in Eugene, OR. [50].

Biophotonics deals with the chemistry of color and all organic molecules respond to electromagnetic waves to some degree. Chromophores are molecules which have a pronounced color response, as in pigments and dyes. Their responses at different wavelengths correlates to the energy structure of the electron orbitals. Fluorophores are radiative chromophores and release energy stored by photon absorption by photon emission. This section covers topics of biophotonics that are of relevance to this work, including cuvette spectrophotometry, microarrays, and optrode techniques. Other useful methods, including FTIR Spectroscopy (Fourier Transform Infrared Spectroscopy) and Raman Spectroscopy, can be found in reference [5].

1.1.1 Fluid Cuvette Spectrophotometry

Spectrophotometers are analytical instruments implementing absorption analysis in a cuvette and are popular optical analytical tools currently available to biologists and biochemists. The cuvette is a small, transparent square vessel typically made from a high transmission polymer or quartz (for UV applications) to hold a solution for analysis. Analysis is typically done in one of two ways. Most organic molecules have absorption in the UV and visible spectrum, and the spectral absorption function is indicative of its composition. Absorbance bands at particular wavelengths correspond to chemical structures in the solution. This method detects the intrinsic absorption spectrum of a molecule. Alternatively, molecules with a weak response to light wavelengths used by the instrument can be enhanced with the use of specifically-bound chromophores which have a strong optical response. Measurements are taken by placing the cuvette in a spectrophotometer which intersects the optical path of a monochromated source ahead of

a detector, as shown in Figure 1.1. The absorption follows from the Lambert-Beer law, given in Equation 1.1. [5] The Lambert-Beer law at a specific wavelength. Absorption is a strong function of wavelength. The molar absorptivity is ε; the path length is l; molar concentration c; absorption coefficient α; and extinction coefficient k and wavelength λ. The initial intensity of the light at a given wavelength is assumed to be I_0 and the measured output is I_{out}. The total absorption is given by A and is the log ratio of I_0 to I_{out}.
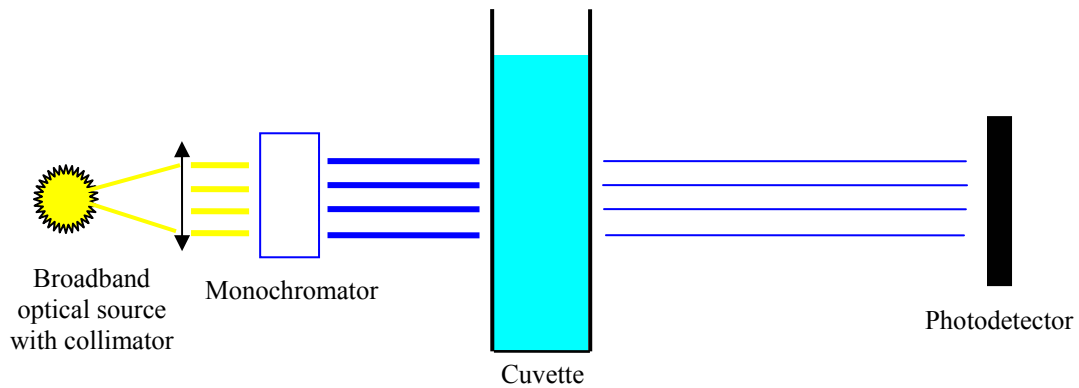
Figure 1.1: A spectrophotometer system for traditional cuvette absorption analysis. A broadband photon source is collimated and sent through a monochromator to select a very narrow spectral region. The monochromatic collimated rays pass through a transparent cuvette containing an absorbing solution. The rays then illuminate a detector to produce a current. The monochromator is adjusted to take absorbance measurements across the emission spectrum of the source.

Equation 1.1

$$A = \varepsilon l c$$

$$\frac{I_0}{I_{out}} = \exp(-\alpha l c)$$

$$\alpha = \frac{4\pi k}{\lambda}$$

The Lambert-Beer law is applicable at intensities less than that of significant nonlinear phenomena and when turbidity or other effects do not cause significant scattering that interferes with the collection of output light.

The principle of absorbance spectrophotometry is closely related to fluorescence spectrophotometry where the specimen emits a photon at a lesser energy than the absorbed energy of the incident photon. Fluorescence spectroscopy is discussed in Section 1.5.

1.1.2 GeneChip Microfabricated Technology

DNA Microarray technology is a method used for the parallel analysis of a sample against a grid of many different biorecognition elements microfabricated on a glass substrate. [6] This technique combines a vast array of biological test species, called "probes," and simultaneously introduces them to a solution containing an analyte whose components matching the probes, called "targets". Mismatching targets are typically in the analyte as well. The clear advantage to this technique is the relatively small volume of solution required to test thousands of targets in parallel against many probes as compared to doing the same experiment with test tubes. A typical microarray, such as the "GeneChip" technology commercialized by Affymetrix Corporation [7], is fabricated by a photolithographic process that builds specific base pair sequences at specific points on a grid. This is shown in Figure 1.1a where the DNA sequences at each grid location are built base by base, and each base is bonded to a desired location while undesired locations are masked to avoid bonding. The grid is then exposed to a fluorescently

labeled target molecule, which binds specifically to the complementary sequence at a particular grid point. The grid is analyzed in a fluorescent scanning microscope and the target composition of the analyte can be determined by the optical response of the grid points. A scheme illustrating the Affymetrix fabrication and microarray technology is shown in Figure 1.2.

(a)

(b)

(c)
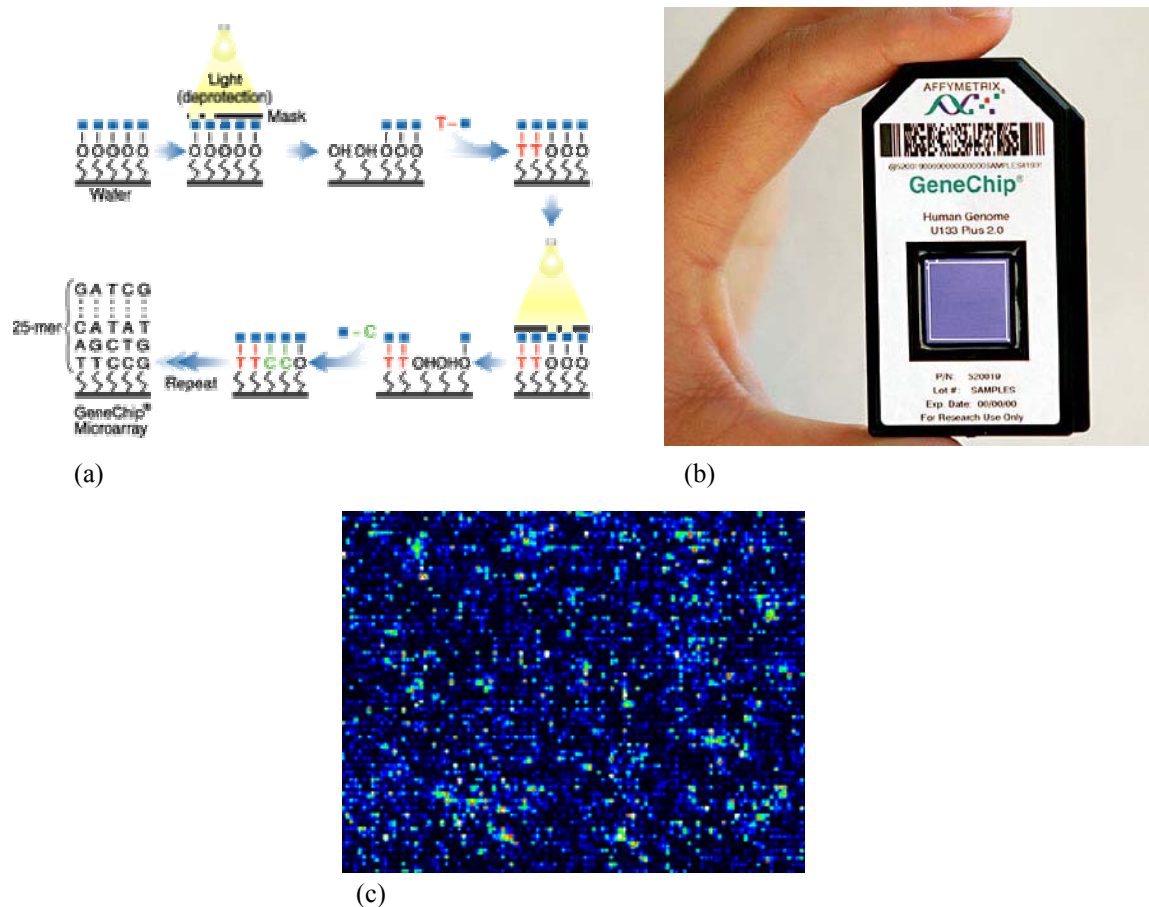
Figure 1.2: Micro-array technology. (a) The fabrication procedure for Affymetrix's microarray technology showing the step-by-step assembly of nucleotide base pairs. (b) The Affymetrix "Gene Chip" with the entire human genome. (c) A top-down view of a microarray where biologically specific sites in a grid respond to light.

1.1.3 Optrode Based Sensing

Optical fibers are dielectric optical waveguides which contain and direct light by the principle of total internal reflection. Although the use of optical fibers is mainly attributed to telecommunications applications, a wide variety of sensor applications exist. Optrode based sensing is a subset of optical fiber sensors where a fiber is used to deliver excitation light and collect emission from an optically active species which is usually in solution. Although fibers can be merely dipped in a solution for the collection of backscattering, the best approach for biosensors that are specific to a target have a biorecognition element secured to the end facet, as shown in Figure 1.3. Biofunctionalization can be implemented with membrane bound reagents, [9] where an optically active element is fixed at the end of a fiber via a semi-permeable membrane. Alternatively, functionalizing the fiber end can be achieved by silanization where the silica surface is imbued with amine groups for coupling. [8] Kuswandi et al. describe other methods for immobilization of biorecognition elements. [9] The backscattered signal increases with increasing fiber core diameter and increasing numerical aperture (NA) which maximizes the cone of bound rays in the core. In a detection system, light is delivered to a fluid via a fiber, and back scattered light is collected by the same fiber and sent to a detector via a beam splitter or directional coupler, as shown in Figure 1.4. Reference [10] details further methods for implementation of such systems. Coupling of light using the evanescent field is another possibility for interaction with medium surrounding the core. Many other sensors have been developed that utilize this technique [11,12]. Still others, developed by Dr. Vildana Hodzic and Dr. Christopher

7

Davis at the University of Maryland, have employed tapered single mode fibers as DNA

hybridization biosensors. [13]
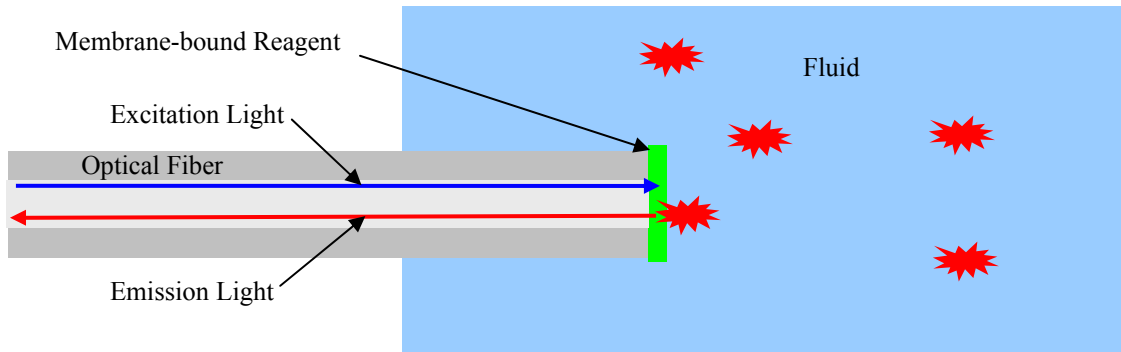
Figure 1.3: Optrode-based sensing. Excitation and emission light is indicated by the blue and red

arrows, respectively.
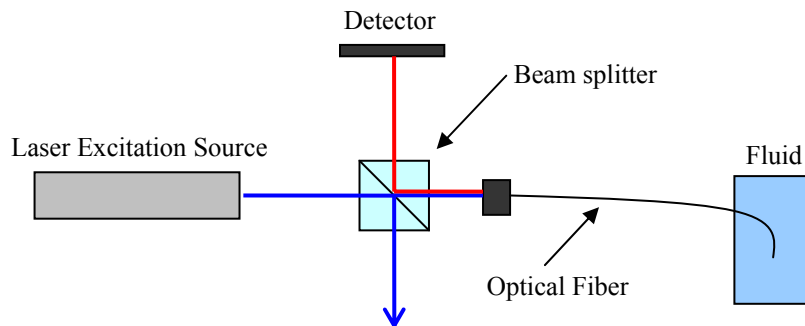
Figure 1.4: An optrode-based sensing system

1.2 Biophotonic Labs on a Chip

Lately, there has been much interest in integrating all of the functions of a typical

biochemical analysis lab on a single chip. Such systems have been labeled as micro-

Total Analysis Systems (micro-TAS) or Lab-on-a-Chip (LOC) systems. The central

theme in all of these devices is the use of microfluidic channel networks to move

reactants and products to where they are needed in a controlled fashion. In-channel

8

sensors are typically required for feedback control systems and analysis. There are many sensor designs proposed for such microfluidic networks. Current Lab-on-a-Chip designs have proposed non-optical sensor methods using magnetic labeling [14,15], radioactive labeling [16], mechanical sensing [17,18,19,20], and cellular sensing by patch-clamp analysis [21]. For decades, the optical microscope has been an essential, if not the most important, tool in biology. For this and the reasons detailed in Section 1.1, industrial and academic research has focused on photonic sensing. Together with MEMS components and microfluidics, the traditional approaches seen in Section 1.1 can be integrated in a single unit. The many different approaches for optical biosensors are classified as either intrinsic sensors or extrinsic sensors.

In intrinsic sensors, the biorecognition element alters the optical properties of a waveguide or light conducting medium. Classic examples of such intrinsic optical sensors make use of specific binding of reagents to the surface of waveguides to change the local index of refraction. Mach-Zehnder interferometers can have one arm of the optical path sensitized with a biorecognition element. Upon attachment of the target species, the sensitized arm experiences a change in the waveguide's effective index which results in modulation at the output of the interferometer. [22] Evanescent wave coupler biosensors are also possible where the biorecognition element modifies the refractive index between waveguides in an evanescent coupler to change the coupling ratios. [10] Surface Plasmon Resonance (SPR) biosensors are very popular and have achieved commercial success. Surface plasmon waves propagate along a metal-dielectric boundary. In these devices, a prism is used to excite an SPR wave by coupling at a

specific angle to the dielectric metal interface. A biorecognition element on the metal layer indicates the presence of a bonded target by changing the critical angle for excitation. [23]

In contrast to intrinsic sensors, extrinsic sensors do not have their optical properties modified by the environment, however they provide coupling to and from optically active elements in the system. Like the optrode sensors, the focus of this thesis is on MEMS-based extrinsic sensors, and has been the subject of review papers, including Verpoorte's paper in Lab-on-a-Chip. [24]

1.2.1 Microoptics and Microfluidics

Microfluidic MEMS components have attracted significant interest in the hopes of achieving the same benefits for biochemical operations as integrated circuits have achieved for electrical operations. To date, techniques exist for fluid channel control in a way intended to be similar to control logic in digital integrated circuits, including multiplexing and routing. Thorsen et. al. demonstrated a microfluidic array that demonstrates these characteristics and is remarkably similar to random-access-memory structures. [54] Although published in 1999, Burns et. al. demonstrated an integrated DNA analysis device that required only an external LED source and pressure source for fluid flow. [25] The device, while rumored to be very expensive to manufacture in its limited quantities, demonstrated the merits of integrated DNA analysis by electrophoretic separation and fluorescence detection. Balslev et. al. fabricated an integrated optical system including an integrated microfluidic dye laser as a fluorescent excitation source in

SU-8. [26, 27] Although these devices accomplished a great deal towards micro-TAS and LOC goals, they lack surface biofunctionalization and instead perform the analysis in a volume of fluid. This can hamper their flexibility and increase the size of the microfluidic networks.

The integration of microfluidics and optical elements can be performed in multiple ways but fall into a few broad categories. It is important to make the distinction between "in-plane" and "out-of-plane" optics. In-plane devices have all of the optical components and optical path in the plane of the chip, as metal traces in an integrated circuit would be. Out-of-plane devices have the optical path extend outward from the plane of the chip, much as the micro-array devices detailed in Section 1.1.2 which relies on external optics focused down on the chip. A "mixed" device could have some optics in-plane and some optics out-of-plane. In-plane systems carry a considerable advantage over out-of-plane or mixed systems due to the increased feasibility of single-chip integration. Otherwise, it is necessary to employ the use of external optics which are bulky, expensive, and sensitive to alignment.

In-plane systems typically use ridge, strip, buried, or fiber optic waveguides which are intersected and broken by a microfluidic channel. Mogensen et. al used integrated waveguides fabricated in SU-8 to create a microfabricated absorbance cell where a microfluidic channel takes the place of a cuvette. [72] Additionally, Mogensen developed Silica-on-Silicon waveguides for cellular sensing purposes. [28] Liang et. al. have adopted a similar approach using fiber optic waveguides. [29] Both authors use a

scheme depicted in Figure 1.5. When light is injected into the input end of the waveguide the Lambert-Beer law absorption due to the fluid in the channel produces a spectrally dependent absorption curve which is detected in an output waveguide. The spectral response is indicative of the chemical composition of the illuminated area.
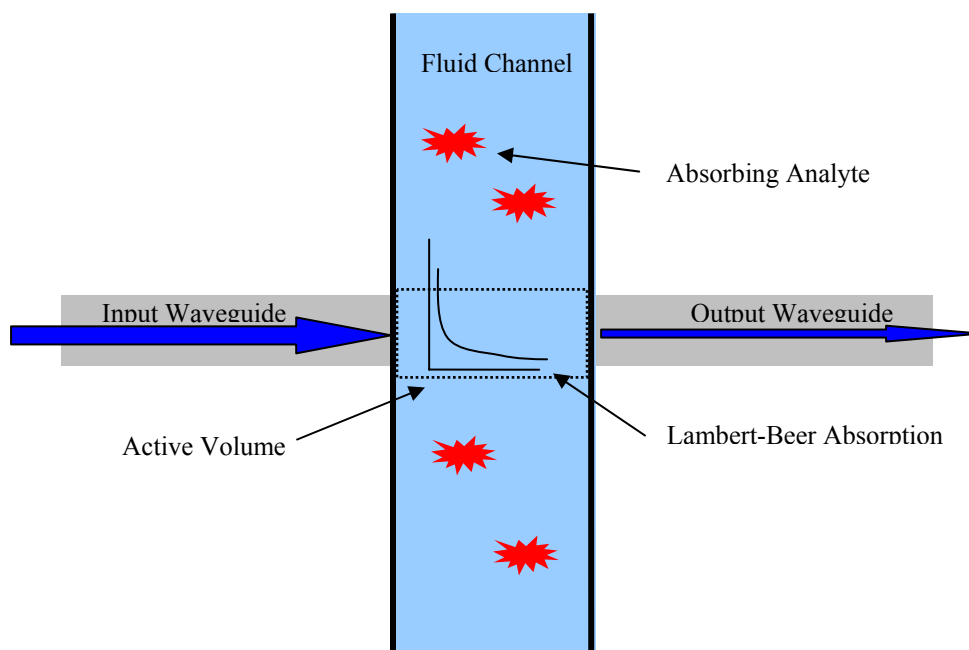
Figure 1.5: A Planar absorbance cell. Light is injected into an input waveguide and measured from the output waveguide after Lambert-Beer law absorption in a microfluidic channel.

In addition to optical detection by absorption, detection by fluorescent emission is also possible. The chief problem for fluorescent detection is the fact that, unlike absorbance cases where the light is directed through the solution, fluorescent emission is emitted approximately equally in all directions[1]. Thus, fluorescent emission exhibits low

---

[1] Fluorescent molecules are actually dipole radiators, but in random orientations the radiation pattern can be considered uniform in all directions. For further details see [48].

brightness (Flux Area^{-1} Steradians^{-1}) and techniques using the same approach as Liang and Mogensen can be difficult. Roulet et. al. resorted to an out-of-plane method with surface microlenses to maximize the capture cross-section of fluorescence emission. [30] Kruger et. al. [31], Cui et. al. [32], Lin et. al. [33], and Hubner et. al [34] have used planar waveguides and fiber optics for particle sensing and fluorescence spectroscopy. Camou et. al. demonstrated the use of lenses on planar waveguides to maximize the capture of fluorescent emission. [35]

The state of the art detection limits for these devices depend on the characteristics of the molecule being sensed, the excitation frequency, intensity, optical geometry, the loss of the optical system, and the sensitivity of the detector. Using a Photo-Multiplier Tube (PMT) and interference filter, Hubner et. al. were able to achieve a detection limit of 250 pM for Fluorescein dye, with high quantum efficiency and emission maximum around 525 nm, but only 100 nM for Bodipy dye with an emission maximum around 660 nm. Liang et. al., in contrast, were able to detect the emission from a 3 nM concentration of fluorophores.

The aforementioned devices demonstrate the optrode-like sensing detailed in Section 1.1.3 where the specimen interacted with light emanating from the waveguide end. Waveguide sensing can also make use of the evanescent field extending into the cladding region. Sophisticated guided wave optics such as ring resonators for concentration enhancement are possible and will be discussed in Section 5.

Any devices like those depicted in Figure 1.5 suffer from two drawbacks stemming from the fact that the analysis is performed in the liquid state instead of a film on a fixed surface. First, a biorecognition element or optically active element must be mixed in a solution, and delivered to the detector area. Thus, mixing and fluid control elements must be integrated on chip or implemented in cumbersome off chip pumps and valves. Second, as with the optrode case discussed in Section 1.1.3, immobilization of the biorecognition element in the optically active area will locally enhance the amount of analyte in the area where it is useful. This is a significant advantage since it decreases the total amount of analyte required by not dispersing it in a large fluid volume that extends well beyond the optically active area. The optically active area is defined by the overlap of the area illuminated by the excitation light and the area from which most fluorescence is within the numerical aperture of the collection optics.

1.3 Chitosan Biosensor Platform

1.3.1 Biofunctionalization in Biosensors

The chief challenge for biosensors is the integration of a biologically sensitive medium, or biorecognition element, with the inorganic transduction elements. These transduction elements could be mechanical, electrical, magnetic, or optical. One well-developed and popular technique is stamping, or "soft-lithography," pioneered by George Whitesides and his group at Harvard and MIT. [36] This can be a robust technique using thiol coupling. Thiol molecules have a sulfhydryl (-SH) group attached to a carbon chain.

14

The sulfur molecule has been shown to have good bonding to patterned gold substrates, and the carbon atom can bond to a wide variety of other molecules. The development of the soft-lithography technique by Whitesides and his group paved the way for many advances in biosensors which exploit this versatile coupling between biology and microfabricated components. [37]

Although soft-lithography completed the link between microfabrication and biology, it has some significant disadvantages which have prompted the development of improved fabrication technologies. First, the process flow of a sensor using the soft-lithography technique poses some problems for the end-user. The equipment to perform the "stamping" procedure requires precise and accurate positioning systems and complicated robotics to achieve good results. This equipment is expensive and not practical for end-users who are not microfabrication experts. Therefore, the biofunctionalization step must either be performed at the time of manufacture, or with expensive on-site equipment. Since many biological molecules are environmentally sensitive and subject to decomposition, the device must be used soon after completion of the fabrication, which is not always practical. Furthermore, stamping methods cannot be used to pattern material in a microfluidic channel after the device has been sealed. Second, stamping applies only monolayers of molecules and the density of active surface sites is strictly limited by the surface area of the biofunctionalized region. For many devices, it would be advantageous to have a biofunctionalized volume in a gel-like network rather than a surface. Volume functionalization methods could increase the number of active sites in surface area limited devices. Third, stamping is an inherently planar process. It is not possible with

current techniques to pattern structures such as microfluidic sidewalls and sloped structures that are possible with grayscale MEMS. [38] What is needed is a technology platform that can be dynamically mediated with external stimuli and is not subject to the geometrical limitations of stamping. It is for these reasons that chitosan biofabrication technology has been developed by the research groups of Dr. Gregory Payne, Prof. William Bentley, Prof. Reza Ghodssi, and Prof. Gary Rubloff, at UMBC, UMCP and UMBI.

1.3.2 Formulation and Deposition of Chitosan

Chitosan is a derivative of chitin, which is the exoskeletal structural material of crustaceans such as insects and crabs. A natural polysaccharide of glucosamine, chitosan is formed by the deacetylation of chitin. During that process, at high temperature and high pH, the acetyl groups on chitin become amine groups, as shown in Figure 1.6. [39] A solution is considered to be chitosan when the ratio of deacetalization (chitosan / chitin) exceeds 50%.
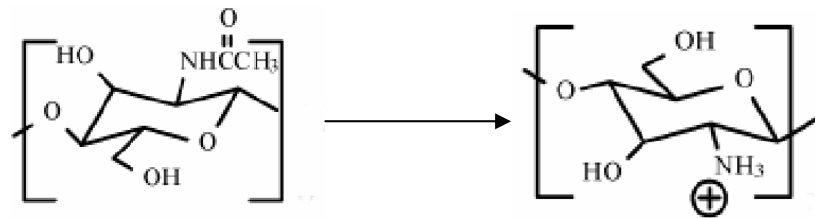
Figure 1.6: The deacetylization of chitin into chitosan. Note that the acetyl group on chitin is converted to a protonated amine group in soluble chitosan.

16

The pH dependent solubility of chitosan enables the dynamic patterning of the material and makes it very useful in biosensor applications. Localized pH gradients can be produced by the electrolysis of water. Previous work has demonstrated the pH responsive solubility and deposition in response to electrical stimuli-induced local pH changes [39]. Additionally, further work has demonstrated that chitosan can be electrodeposited when conjugated (attached) to reactive species [40]. The results of these demonstrations have significant consequences. Like soft-lithography based biofunctionalization schemes, chitosan demonstrates spatial selectivity (that is, accurate and precise patterning of an intended geometry of biofunctionalized material). However, the patterning procedure can be dynamically driven, is less complicated, and can be carried out without the use of sophisticated equipment. Figure 1.7 shows the electrolysis process that deposits chitosan on patterned conductive surfaces.
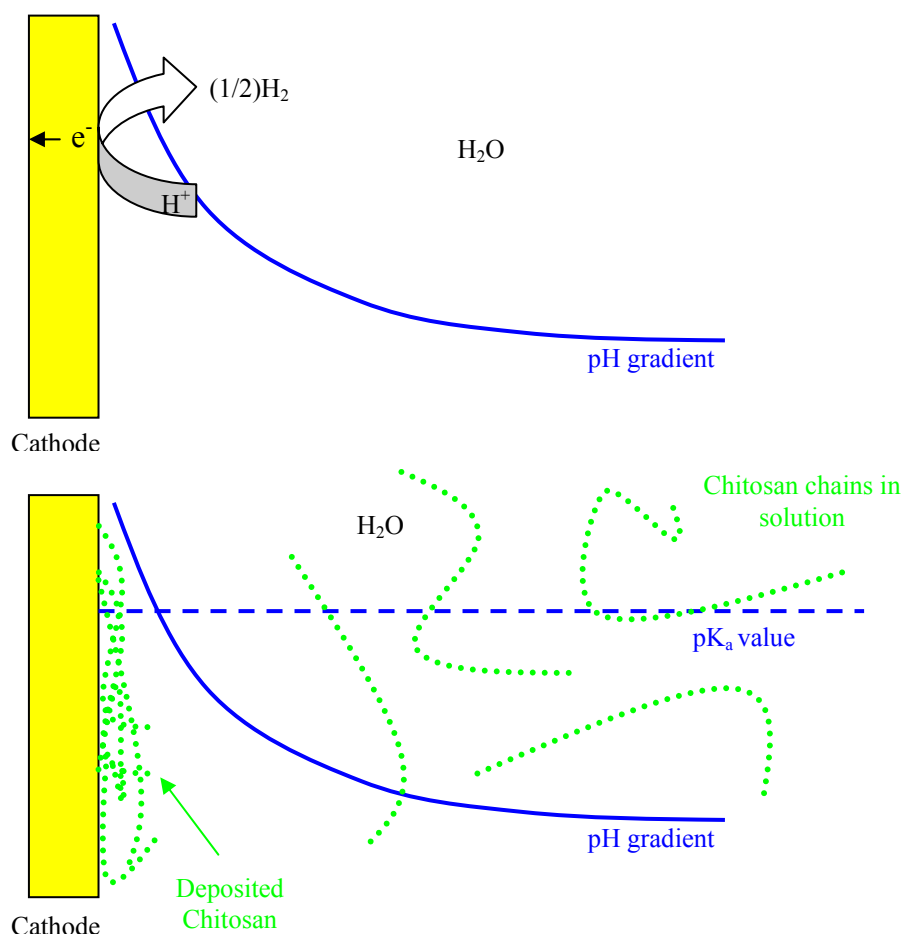
Figure 1.7: (a) Top: Electrolysis of water creates a localized pH gradient at the cathode. Hydrogen evolution at the cathode increases the OH⁻ concentration and increases the pH. (b) Bottom: Chitosan is soluble at low pH, below its pK_a value, and is insoluble at high pH where it deposits on the cathode.

The physical process of deposition is the result of two factors, electrostatic attraction and pH dependent solubility. The relative contribution of each factor changes the film properties. Chitosan deposition can be broadly categorized as either a "thin-film, glassy" morphology or a "hydrogel" morphology. The deposition type depends on the current density of the electrodeposition. Generally, it has been speculated that the hydrogel type

depositions are dominated by pH gradient deposition where the pH above the pK_a value extends for a significant distance away from the electrodes (on the order of hundreds of microns) due to high current density. At lower current densities, the pK_a threshold extends about a micron to a few microns away from the electrode and the electrostatic attraction of the soluble, protonated chitosan strands dominates the net deposition process. The film that results is very smooth, clear, and more dense than hydrogel depositions.

Soluble   Insoluble
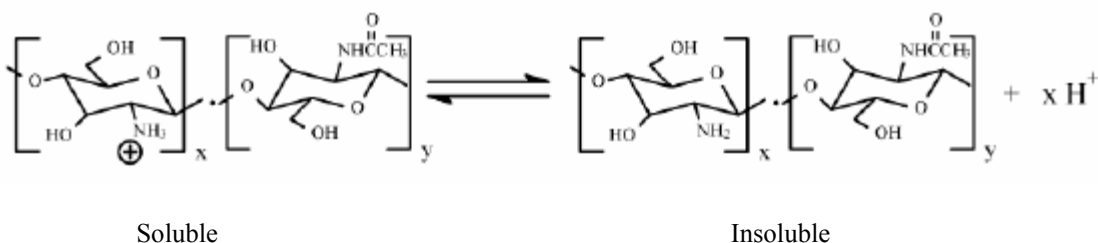
Figure 1.8: A molecular view of chitosan deposition. The fraction of chitosan is x and y is the fraction of chitin. At high pH, the positively charged amine group on chitosan is deprotonated and a hydrogen ion is produced.

Figure 1.8 shows the chemistry of the deposition of chitosan. [39] When soluble, the amine group on chitosan is protonated and positively charged. When the pH exceeds chitosan's amine group pK_a value of 6.3, it becomes deprotonated and insoluble in water. This pK_a value is very favorable because it causes chitosan to transition in the region of physiological pH values and makes it compatible with a wide variety of bioprocesses. Other polysaccharides are electrodepositable, however they have higher pK_a values. Polylycine, for example, has a pK_a value of 10.5, which is too basic for fragile biomolecules such as proteins as it makes conjugation reactions unfeasible.

Table 1.1 gives the current density deposition parameters for chitosan. The deposition characteristics can vary and are not always the same between runs. Chitosan is also known for its significant inconsistencies between batches. As a bio-derived material, each batch may have slightly different deposition conditions with respect to salt content, molecular weight, and base pH. Listed in Table 1.1 are the generally observed parameters for deposition.

Table 1.1: Chitosan Deposition Parameters [41]

Current Density	Deposition Type
1.25 A m^{-2}	No Deposition
3.75 A m^{-2}	Thin Film Deposition
6.25 A m^{-2}	Transitional Hydrogel Deposition (white, loose film)
7.5 A m^{-2}	Start Hydrogel Deposition
12.5 A m^{-2}	Hydrogel Deposition

1.3.3 Conjugation and Biofunctionalization of Chitosan

The fact that chitosan electrodeposition can be controlled with electrical signals is of considerable importance, but chitosan alone has no intrinsic biological function. However, one can conjugate other biomolecules, such as proteins, enzymes, and DNA, with a specific biofunctionality onto chitosan resulting in a conjugate structure that has the electrically responsive properties of chitosan and the specific biochemical properties and activity of the conjugate species. Chitosan can be conjugated prior to deposition or following deposition as a thin film or hydrogel. The conjugation operations link other molecules to the amine groups on chitosan. Previous work has used NHS chemistries to

conjugate Fluorescein dye to chitosan before and after deposition. [40]. A scheme for
this reaction is given in Figure 1.9. [42]
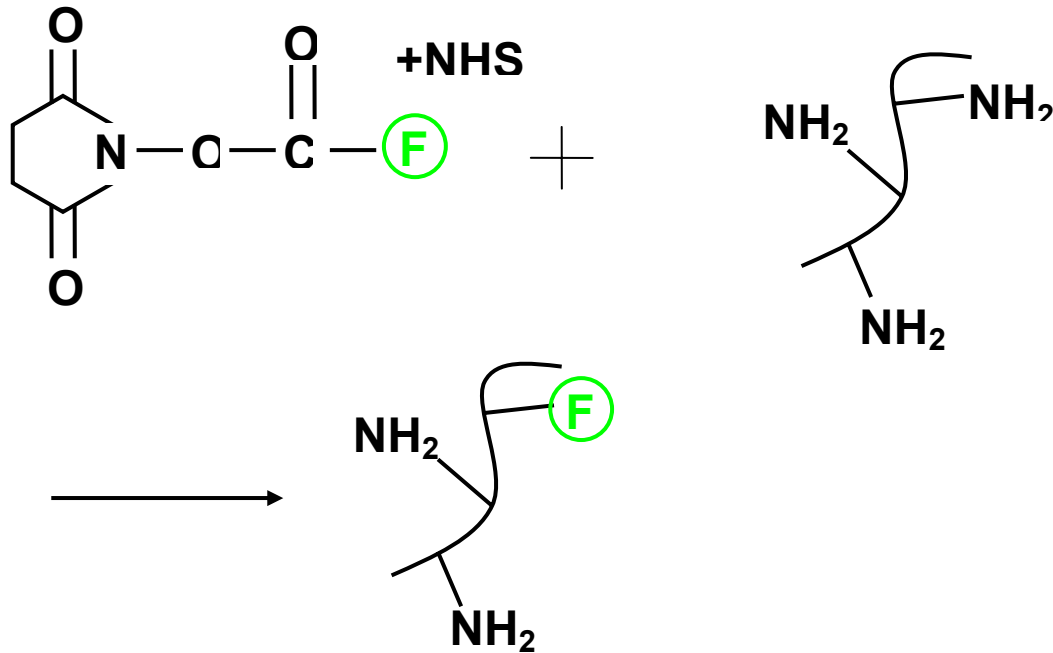
Figure 1.9: Preparation of fluorescently labeled chitosan.

Chitosan can also be conjugated with large molecules such as proteins and enzymes,
which enables the spatially and temporally selective deposition of these reactive
biomaterials. Further, genetic engineering may enable "fusion tail" additions to allow
controlled conjugation of proteins to chitosan. A simplified scheme of this operation is
shown in Figure 1.10. [43]
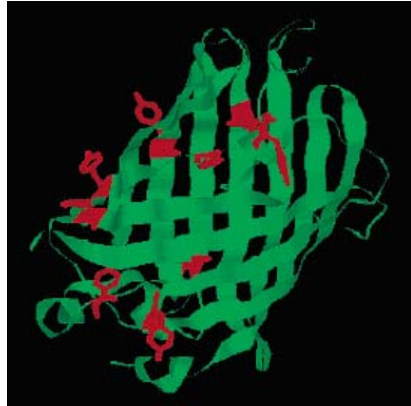
a) GFP
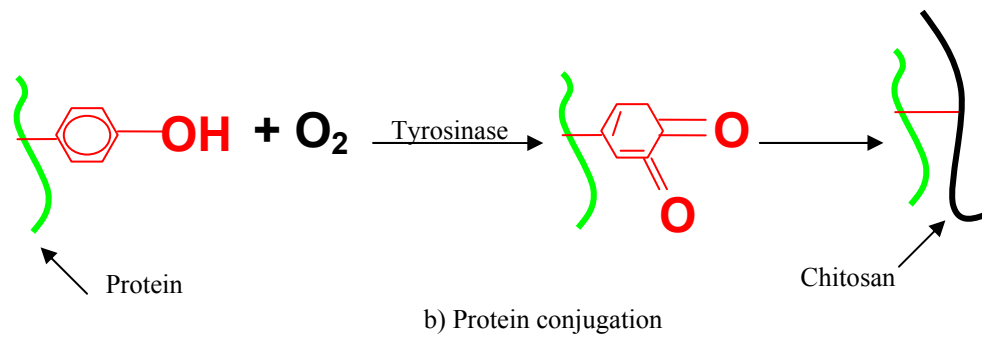
Protein

Chitosan

b) Protein conjugation

Figure 1.10: Protein-chitosan conjugation. The Tyrosyl "fusion tail" residues on GFP are shown in red in part (a). With the action of the tyrosenase enzyme, the tyrosyl residiues are oxidized into Quinone groups which can form covalent bonds with chitosan.

The work in this thesis focuses specifically on the functionalization of deposited chitosan with single stranded DNA (ssDNA) probes. The DNA hybridization probe technique, which will be described in a later section, requires that ssDNA be tethered to the chitosan. Fortunately, the versatility of chitosan lends itself well to this purpose. Three types of ssDNA have been obtained through DNA synthesis. The structure of these molecules is given in Figure 1.11. Probe ssDNA has a fluorophore conjugated on one end, and is complementary to the target ssDNA (Figure 1.11a). The target ssDNA has a fluorophore conjugated to the opposite end (Figure 1.11b). Labeled probes (Figure

1.11c) have ssDNA terminated with an amine group on one end and a fluorophore on the other. This probe serves as a label to verify that the ssDNA can be covalently bound to the chitosan.
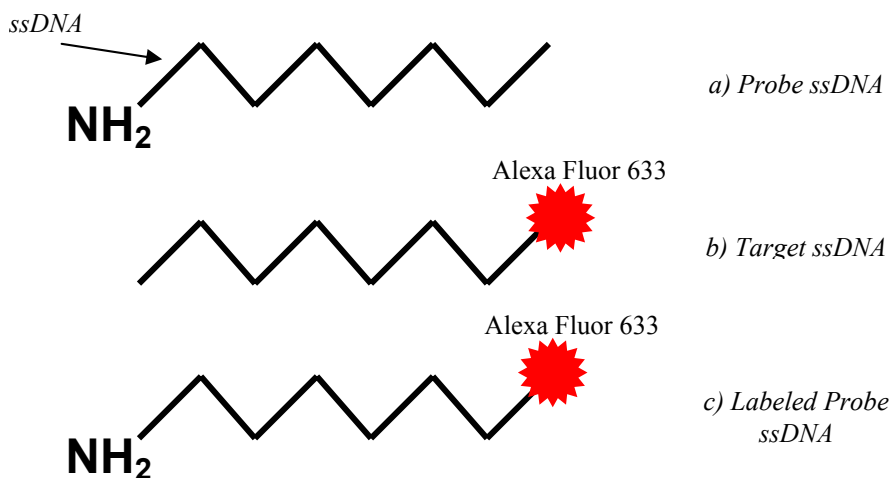
Figure 1.11: DNA probe (a), target (b), and labeled probe (c).

The covalent bonding of the ssDNA probe to the amine groups on the chitosan can be accomplished by means of glutaraldehyde cross-linking chemistry. This method is similar to that used by Grahm et. al. [44] and was adapted for use in this situation with the assistance of Dr. Hyunmin Yi [42] of UMBI. Glutaraldehyde is a powerful cross linker with aldehyde groups (-CHO) on the end of a carbon chain. The aldehyde groups can covalently bond to the amine groups on the chitosan. Some of the glutaraldehyde cross-links to the chitosan itself by forming amine-aldehyde bonds with both ends of

glutaraldehyde, while other sites remain with a free aldehyde end. This free aldehyde can couple to amine terminated ssDNA strands, as shown in Figure 1.11. The availability of free aldehydes for subsequent bonding to ssDNA is determined by steric hindrance, [45] which allows or disallows binding of molecules based on their spatial relationships, e.g. blocking.   The structure of the solid chitosan material, which is influenced by the deposition parameters, can affect this. Figure 1.12 shows the scheme of the coupling reaction.
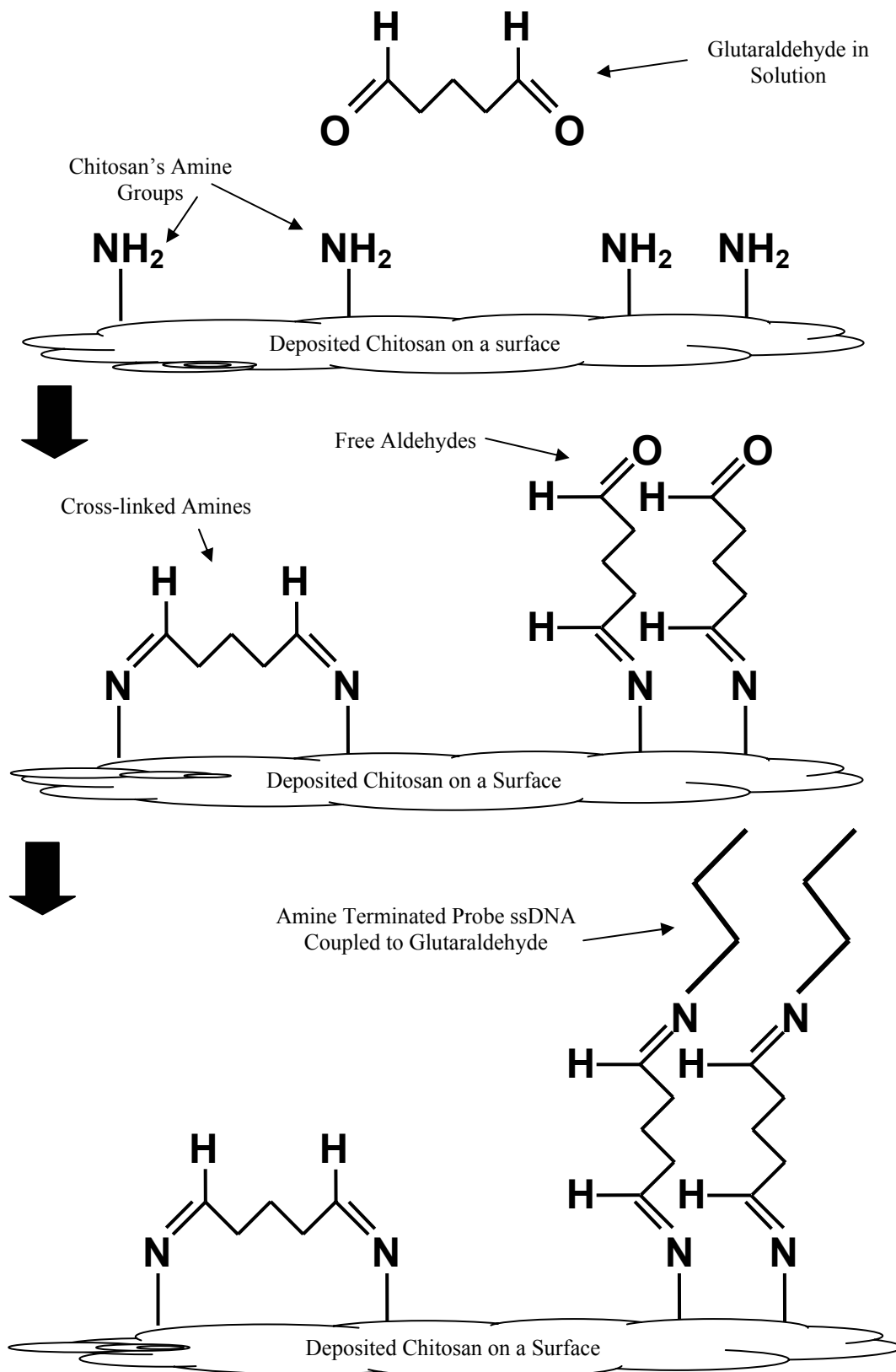
Figure 1.12: (a) amine - aldehyde coupling. (b) chitosan crosslinking and DNA coupling

25

The ability to couple probe ssDNA to chitosan is especially important since it allows the user to confer very specific chemical properties to a film that has been deposited with spatial and temporal selectivity. This formulates the key biorecognition element which will be important in the DNA sensor tests discussed in Chapter 4.

1.4 DNA and DNA Hybridization

DNA has been considered to be the basis for all modern biology since its discovery by Watson and Crick in 1953. It is the genetic code that specifies the structure and composition of life and is found in the nucleus of all eukaryotic cells and in the cytoplasm of prokaryotic cells. DNA is a polymer comprised of Deoxyribose sugar monomers for a structural backbone, as shown in Figure 1.13. [46] The actual DNA code that specifies proteins is specified by bases. There are 5 possible bases, Adenine (A), Guanine (G), Cytosine (C) are found in DNA and RNA while Thymine (T) is only in DNA and Uracil (U) is in RNA. Three base-pair combinations constitute a "Codon" of DNA. A unit of the sugar monomer with a nitrogen base and a phosphoric acid molecule (H_3PO_4) comprise a nucleotide, the building block of a DNA Chain. The nucleotides are commonly abbreviated by the first letter of their Nitrogen base.
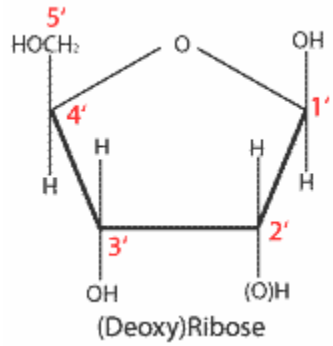
Figure 1.13: Molecular form of the Deoxyribose sugar backbone of DNA. Ribose, the structural element of RNA, contains Oxygen at the 2' position while Deoxyribose, of DNA, does not. The 5' and 3' ends are labeled appropriately.

Figure 1.14 depicts the nucleotide base unit, sugar backbone, and double helix structure of DNA. [47] From this figure, it is important to note the negative charges on the backbone as this is a significant consideration for the DNA hybridization reactions described in this thesis.
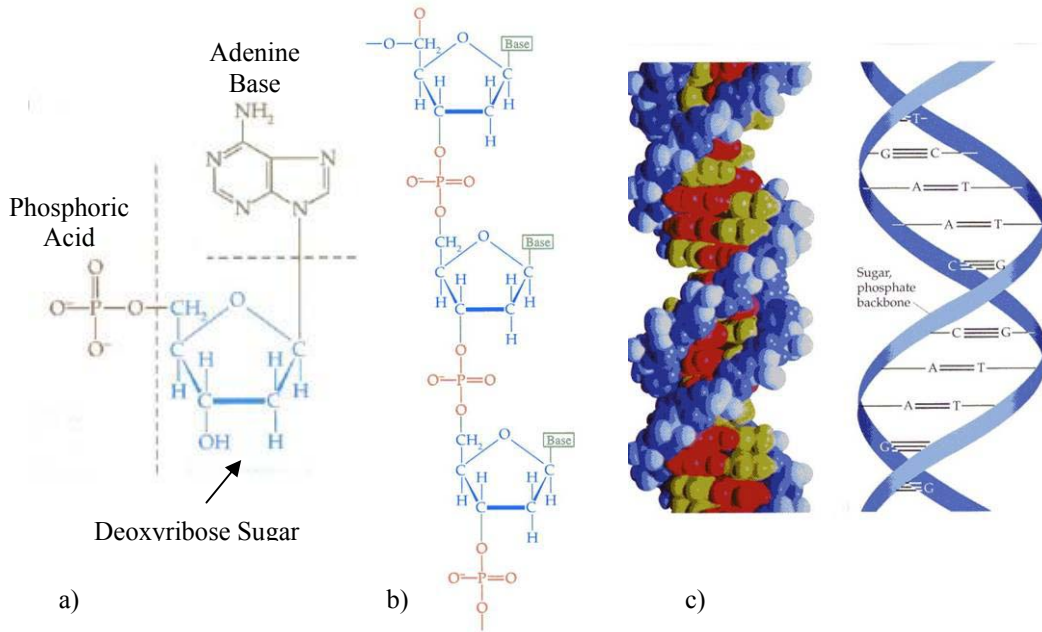
Figure 1.14: (a) The Adenine nucleotide with the phosphoric base unit, sugar unit, and adenine unit. (b) Single-stranded structure of the DNA Deoxyribose-phosphoric acid. (c) Double-helix structure.
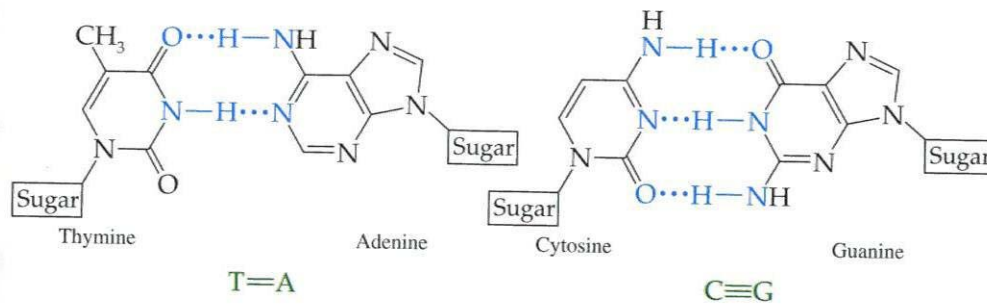
Figure 1.15: Bonding between complementary DNA base pairs.

The base pair bonding for complementary DNA nucleotides is shown in Figure 1.15. [47] Thymine always matches to Adenine and Guanine always matches to Cytosine. The physical nature of the bonding is that of Hydrogen bonding and London-dispersion

interactions. Hydrogen bonding is an intermolecular force that exists in a polar molecule when close to a small electronegative ion or atom with an unshared electron pair. London dispersion is the result of attractions between instantaneous dipoles and induced dipoles. [47] When complementary single-stranded DNA is in solution, it will form bonds between complementary bases and cross-link strands that have complementary sequences. This process is known as hybridization. In the device discussed in this thesis, DNA is used as a biorecognition element. Figure 1.16 shows a general scheme of DNA hybridization on a surface. Single stranded DNA probes with a specific sequence are first tethered to a surface. Then, single stranded DNA targets that have been labeled with a fluorophore with a color indicating the sequence are introduced in solution. After equilibrium has been achieved and rinsing in a buffer, a significant fraction of the DNA probes are hybridized with a matching DNA target (colored blue). The reaction kinetics have an equilibrium ratio of occupied probes to total probes at some number less than unity. The mismatching targets (colored magenta), experience little to no bonding on the surface. This reaction forms the basis for a DNA hybridization biosensor.
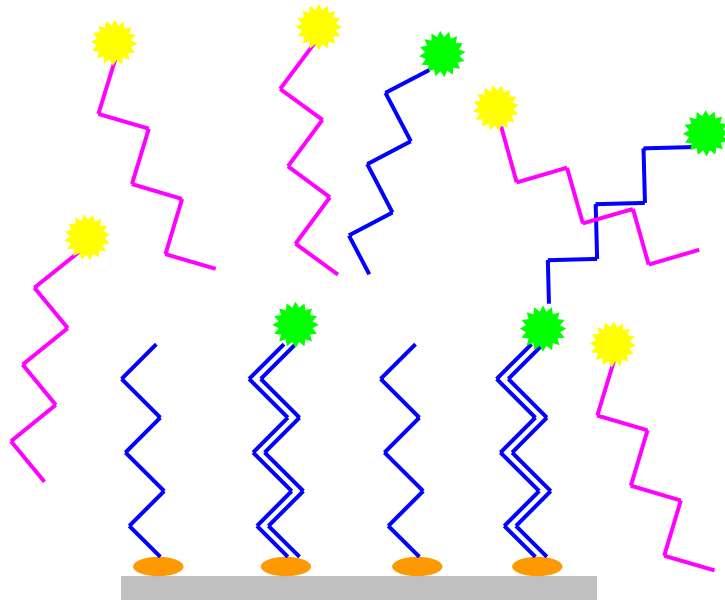
Figure 1.16: DNA hybridization on a surface. The complementary DNA strands are giving matching colors. The fluorophore colors are specifically matched to a given DNA sequence.

1.5 Molecular Fluorescence

Molecular fluorescence is one type of luminescence. Luminescence is defined as the emission of photons from an electronically excited species. This electronic excitation can come from a variety of energy sources as listed in Table 1.2. [48]

Table 1.2: Types of Luminescence

Luminescence Type	Excitation Energy Form
Photoluminescence	Photons
Fluorescence	
Phosphorescence	
Radioluminescence	Ionizing Radiation
Cathodoluminescence	Cathode Rays (Electrons)
Electroluminescence	Electric Fields
Thermoluminescence	Heating (after prior energy transfer)
Chemiluminescence	Reaction where product(s) are in an excited state
Bioluminescence	Chemiluminescence of Biological Compounds
Triboluminescence	Frictional and Electrostatic Force
Sonoluminescence	Ultrasound Acoustic Waves

When a molecule absorbs light it enters an excited state, and there are many possible ways of releasing the absorbed energy. Generally, these are classified as radiative or non-radiative. Radiative processes produce a photon, while the non-radiative processes releases the energy by a chemical, vibrational, or electronic transfer. The energy of visible radiation corresponds to electronic transitions, while the energy of infrared radiation corresponds to vibrational transitions. A scheme adapted from [48] is shown in Figure 1.17.

Phosphorescence

Delayed
Fluorescence

Intersystem
Crossing

Fluorescent
Emission

Internal
Conversion

hν

Intramolecular
Charge Transfer

Excited
Molecule

Conformational
Change

Electron
Transfer

Photochemical
Transformation

Proton
Transfer

Exiplex
Formation

Eximer
Formation
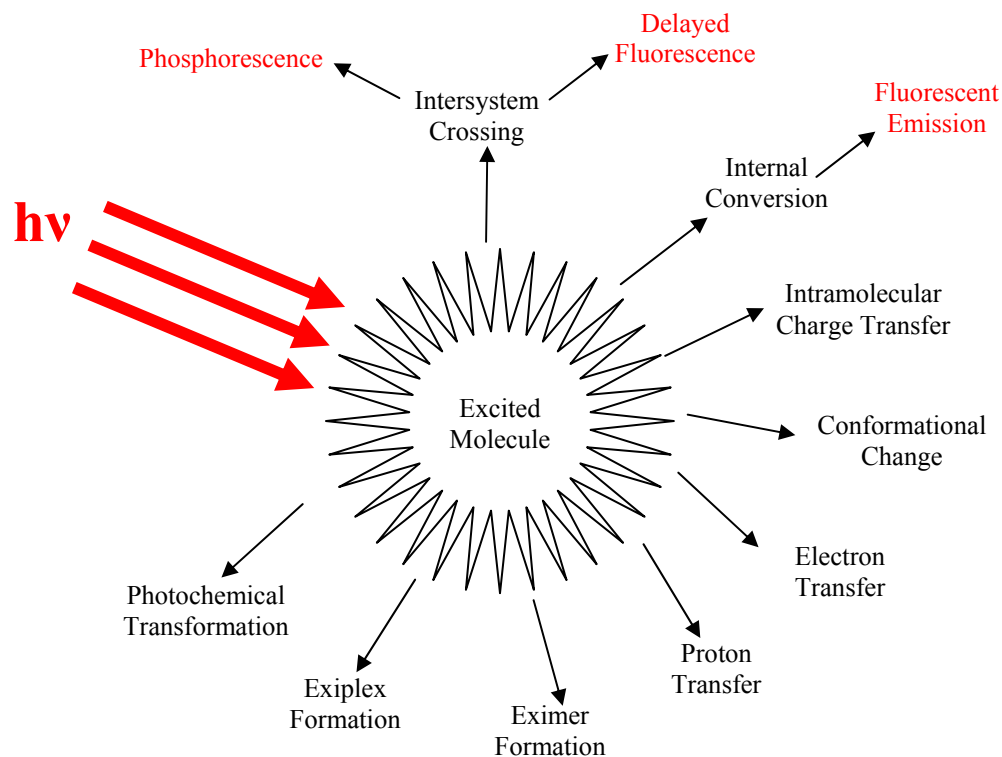
Figure 1.17: Means of releasing energy stored in a molecule by photon absorption. Adapted from Valeur [48] with modifications. The radiative release pathways are given in red, while the non-radiative releases are black.

The excitation and relaxation processes are typically illustrated in a Jablonski diagram, which is shown in Figure 1.18. At typical temperatures, all of the molecules can be assumed to be in state S_0, the ground state. A molecule is excited to a vibrational state (indicated by thin lines) in an electronic excitation band (indicated by thick lines) by photon absorption, as shown by the blue arrow. This excited vibrational state quickly decays (on the order of 10^{-13} to 10^{-11} s) to the bottom level of the S_1 electronic excitation band in a process known as Internal Conversion (IC). This process of transferring the vibrational energy to the solvent is responsible for the wavelength shift, or Stokes shift,

that is the difference between the excitation and emission spectrum in fluorescence. Most molecules usually return to the ground state from the bottom of S_1. A chromophore ("color molecule") decays by non-radiative means, however the fluorophore decays radiatively and is luminescent. The decay time from the excited state to the ground state is on the order of 10^{-10} to 10^{-7} seconds for fluorescence emission. Alternatively, Inter-System Crossing (ISC) can occur at a point with in the S_1 band instead of internal conversion, where the electron could flip its spin by spin-orbit coupling and enter a triplet state. [5] The decay constant from the triplet state to the ground state (orange transition in Figure 1.18), known as phosphorescence, is substantially longer with a decay time of about 10^{-6} to 1 second. Nonradiative decay to the ground state is not shown in Figure 1.18 but is responsible for the quantum yield that is strictly less than 1 in fluorescent substances.
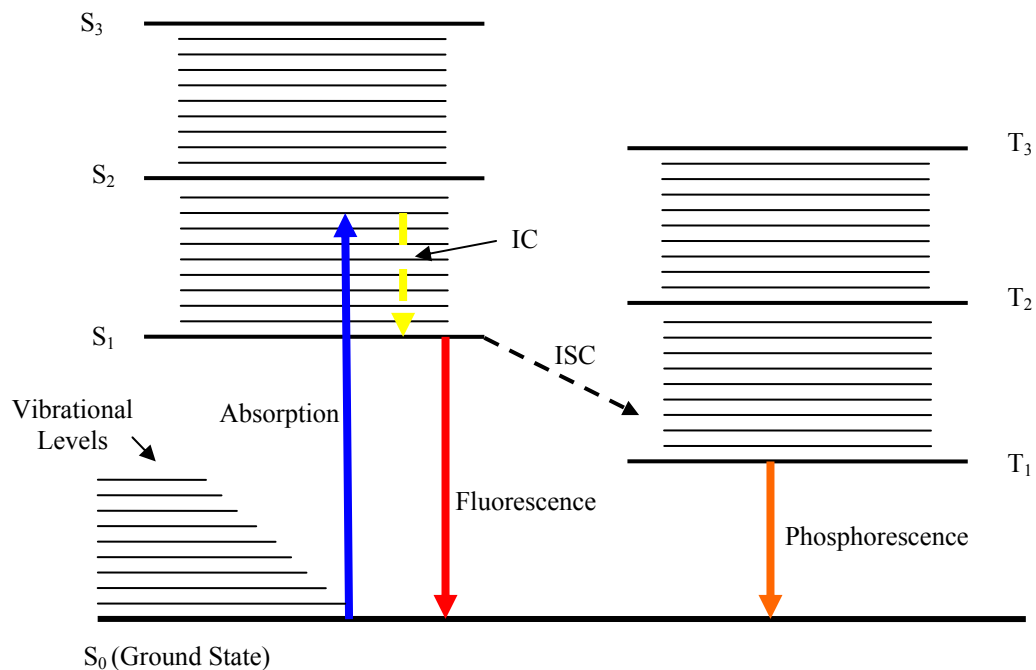
Figure 1.18: Generalized Jablonski Diagram detailing absorption, the radiative processes of fluorescence and phosphorescence, and the non-radiative internal conversion (IC) and intersystem crossing (ISC)

The absorption and emission of a generic fluorescent molecule is depicted in Figure 1.19. Generally, the absorption and emission spectrums are mirror images of one another. A global maximum for each is observed, and the separation of the emission maximum and absorption maximum is known as the Stokes shift. Smaller peaks in the spectral density functions are the result of vibrational levels in the molecule.
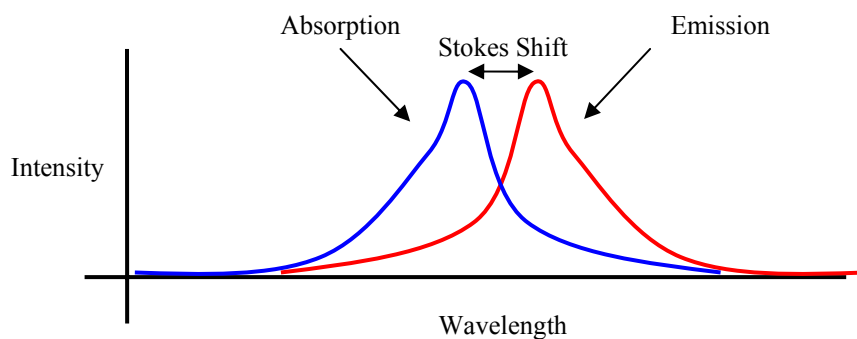
Figure 1.19: The spectrum of a fluorescence molecule showing absorption and emission spectral density functions

The electronic excitation is the promotion of an electron from a ground state orbital (usually in the HOMO – Highest Occupied Molecular Orbital) to an orbital of higher energy (usually the LUMO – Lowest Unoccupied Molecular Orbital). In general, bonds in organic compounds can be in π or σ configurations or an n non-bonding orbital. An σ bond configuration is formed by two s orbitals, an s and p type orbital, or two p type orbitals if their axes are aligned to be collinear. A π bond results from the overlap of two p orbitals with coplanar axes. [47]

Most fluorescent molecules are aromatic hydrocarbon structures. In the benzene ring structure, the overlap of π orbitals causes a delocalization of the bonds. [47] This effect reduces the energy required for π to π^* promotions and allows fluorescence to occur at visible wavelengths. [48] Excitation of σ orbitals is not typical as the characteristic energies are deep in the UV, at 125 nm. [5] Absorption is directionally dependent. For aromatic hydrocarbons, the absorption takes place in the plane of the ring structures and has a dipole absorption moment which is typically longitudinally or transversely oriented

35

to the molecule. Thus, the absorption depends on the polarization of the light where absorption is strong when the dot product of the electric field vector and the molecule dipole moment is high, and weak when the dot product is low. [48] For molecules in solution and illuminated by randomly polarized light, this dependence can be averaged out. Figure 1.20 shows the chemical structure of two of such molecules. [49, 50]
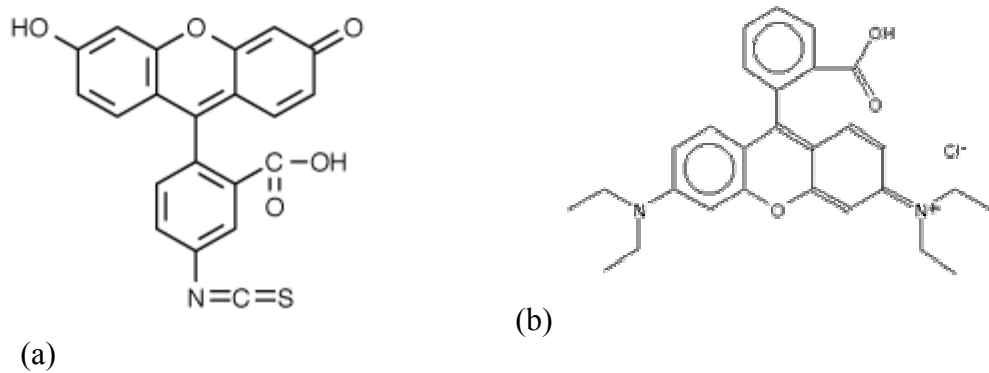
Figure 1.20: Fluorescent Molecules. (a) Fluorescein-5-iothiocyanate, (b) Rhodamine B

The fluorescence of molecules can be analyzed in the time domain or the frequency domain. In many cases, multiple sources of fluorescence will be present in the same specimen. This could be the result of the need to analyze the response of many different fluorophores simultaneously, or could be the result of fluorescence background from other sources which are intrinsically fluorescent. Time domain analysis can be used to discriminate between fluorescent molecules with similar spectra but dissimilar decay times. Polymers are a common material in BioMEMS, and some polymers are mildly fluorescent. Fortunately, this background fluorescence can be distinguished from materials that are intentionally fluorescent because background fluorescence typically has

a shorter lifetime. The shorter lifetime fluorescence, indicated by the yellow line in Figure 1.21a can be neglected by restricting analysis to fluorescence which is sustained at times beyond the first dashed line. An instrument could use a "gated detector" to only measure fluorescence occurring over a specific time interval. [10] Additionally, phase shift techniques can be used to determine the fluorescence lifetime. Since the lifetime is finite, a modulated excitation source would elicit modulated emission offset by some constant phase. This phase shift can be related to the fluorescent lifetime by taking the arctangent of the product of decay constant and modulation frequency. [5] Frequency domain is perhaps a more common mode of discrimination and can be used to differentiate between molecules of different emission spectra, as shown in Figure 1.21b. Band-pass filters can be used in an optical system to select different portions of the electromagnetic spectrum corresponding to the emission of a desired fluorophore. Figure 1.22 is a superimposed image of several frequency spectrums corresponding to different fluorophores in an example of frequency discrimination fluorescence. [50]
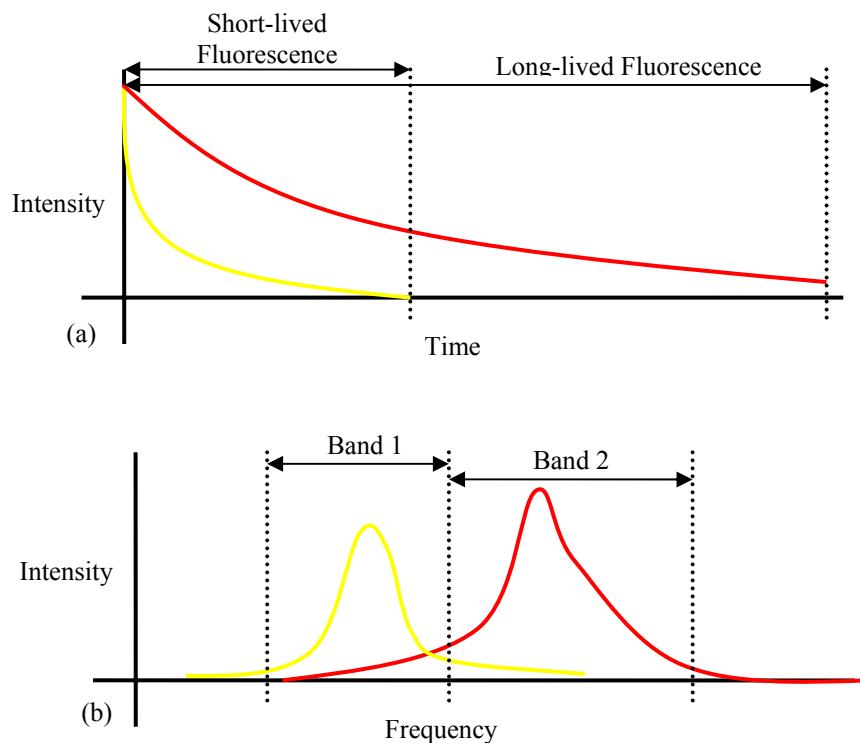
Figure 1.21: (a) Time-domain fluorescence. The fluorescence is discriminated by the decay lifetime. (b) Frequency-domain analysis. The fluorescence is discriminated by the frequency separation of the emission.
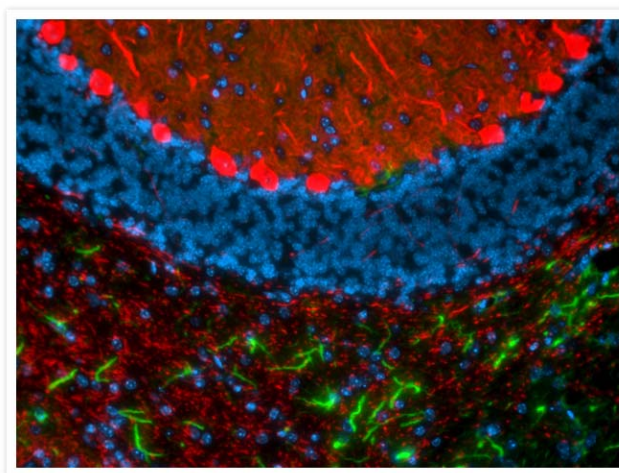
Figure 1.22: Discrimination of different chemical components by frequency-domain analysis. In this image of a mouse cerebellum, Different fluorophores with different emission frequency spectra are functionalized with chemistries with specific affinities to components of interest.

Parker's Law describing the fluorescent intensity of a liquid is analogous to that of absorption. [51] Since most fluorescent solutions are weakly absorbing, the intensity as light propagates through the medium can be taken as a constant. Equation 1.2 is Parker's law, which demonstrates similarity to that of the Lambert-Beer law for absorption. It is given for incident intensity I_0, quantum yield Φ, molar absorption coefficient ε, concentration C, and optical path length l. The constant k depends on the geometry of the optical system. The bottom equation is a simplification of Parker's Law if the intensity can be assumed to be approximately constant along length l. [51]

Essentially, the fluorescent intensity is related to the quantum yield of the fluorophore, which is the ratio of the number of photons emitted to the number of photons absorbed. Also, it is important to consider the optical constant k which relates to the cross section of the system optics, since fluorescence is spontaneous emission and is dispersed in all directions.

Equation 1.2

$$I = 2.3 \cdot I_0 \Phi \varepsilon Cl \left[1 - \frac{2.3 \cdot \varepsilon Cl}{2!} + \frac{(2.3 \cdot \varepsilon Cl)}{3!} + \dots \right] k$$

$$I = 2.3 \cdot I_0 \Phi \varepsilon Clk$$

1.6 Molecular Probes

A molecular probe is an optically responsive molecule that has characteristics which are modulated by its environment or serves as an indicator of a specific analyte to which it bonds. Some probes have both features.   Generally, however, they can be grouped into two categories and that can depend on how they are used.   Environmental probes are

those that change properties in response to the environment. For example, Fluorescein has a pH sensitive quantum yield, and Phenolphthalein increases in spectral absorbance at high pH when it is deprotonated. The intensity and spectral properties of each molecule are modified by the surrounding conditions, and bulk responses can be measured. When these types of probes have specific binding chemistry, the intent is usually to anchor them to a substrate. The other category of fluorescent probes are the "labels." These probes have a specific binding chemistry that attaches them to a molecule of interest. The properties of the fluorescent molecule are not altered, but rather the intent is to impart luminescent behavior on another molecule. Fluorescein dye can also be used in this fashion, along with Rhodamine, Texas Red, Oregon Green, BODIPY, Coumarin, and Alexa Fluor. While the intensity of each fluorescent molecule is not intentionally modified by the environmental conditions, the bulk intensity of molecules in solution or on a surface can be related to the concentration of the analyte if the concentration is not so high that self-quenching (the introduction of non-radiative decay) will occur.

Quenchers are another functional component in the molecular probe framework. These are molecules or metal conductors which, in close proximity to excited-state molecules, will provide a non-radiative decay pathway with low decay time constant. Quenchers decrease the effective quantum efficiency of fluorescence species. When fluorophores and quenchers are combined in a molecular structure, "molecular beacons" are possible. These are structures which like the environmental probes, will have their quantum efficiency modulated from a low value to a significantly higher value by the presence of other molecules in solution. In principle, the presence of the target molecule increases

(or perhaps decreases) the distance between the fluorophore and quencher, thus modulating the quantum yield. Some typical molecular beacons consist of a "hairpin DNA" structure that uses hybridization to change the relative positions of the fluorophore and quencher. [52, 53] When using molecular beacons, it is not necessary to label the target molecule which can be a cumbersome process.

2 Design

2.1 Design Approach

The design of this sensor is a fusion of two important tools for biological analysis, micro-array technology and fluorescent cuvette analysis. Micro-array technology is a planar process where probe biorecognition elements are patterned in a 2D array. The combined merits of these techniques are augmented by their integration in a microfluidic network and enabled by the chitosan platform technology. First, the traditional micro-array approach is extended by integration within microfluidic channels so that sequential biochemical reactions could be directed and controlled. The integration with microfluidic channels opens the door to microanalysis systems that have the capability for fluid channel interfaced reaction chambers and other such techniques. [54] Second, integrated waveguides provide an extra dimension of sensing over the traditional 2D micro-arrays. The integrated waveguides and fiber-optics provide a lateral way of optically interfacing with the biorecognition elements while leaving the "top-down" view of the device free for examination with a microscope or other elements and analysis equipment.

2.2 Sensor Design

The goal of this sensor, unlike some other photonic microfluidic sensors, is to implement the sensing medium on a fixed surface (using Chitosan) within the microfluidic channel.

This means that the chitosan surface must be aligned for best optical coupling to the waveguide. The design had several requirements:

1. Compatible with in-plane optics and waveguides

2. Provide good optical coupling (= efficiency)

3. Minimize backscattering of excitation light

4. Minimize the perturbation of fluid flow in the channel

5. Anticipate scaling down to smaller dimensions and integration with other components

Of these, optical coupling and elimination of backscatter drove the design decision most significantly as this directly affects the sensitivity of the device. The minimization of backscattering and maximization of optical coupling increases the Signal to Noise Ratio (SNR). Several designs were considered and are described in the subsequent sections.

2.2.1 Integrated Waveguides

In-plane operation suggests the use of planar waveguides to route light. Strictly speaking, a waveguide is a structure in which electromagnetic waves can be guided from one point to another, and remain laterally confined along the direction of travel. [55] Typically, the term "waveguide" is used when the guiding structure's lateral dimensions are comparable to the wavelength. Guided wave structures with dimensions much larger than a wavelength, where ray optics approximations are valid, are typically called Internal Reflector Device (IRD) or a "Light Pipe". For the purposes of this discussion and to maintain the most generality (because these devices could be made at smaller scales), the structures will be referred to as waveguides.

The principle of internal reflection is a consequence of Snell's Law, which describes refraction at a dielectric interface. When a wave propagating in a medium of higher index encounters an interface with material of lower index, the wave can be totally internally reflected into the higher index material when the angle of incidence to the normal of the interface is less than some critical angle θ_c. Total internal reflection is 100% efficient for perfectly flat surfaces that are far from another high index material so as to avoid evanescent coupling that is sometimes referred to as frustrated total internal reflection. Snell's law and this angle are expressed in Equation 2.1. [60]

Equation 2.1

$$n_{core} \sin \theta_{core} = n_{clad} \sin \theta_{clad}$$

$$\theta_c = \arcsin\left(\frac{n_{clad}}{n_{core}}\right)$$

Optical waveguides are defined by a region of high index material known as the core which is surrounded by a region of low index material known as the cladding. [56] There are a variety of waveguiding geometries. Among these are the strip waveguides used in this design which have a high index core fabricated on a low index substrate with other cladding, in this case air, on the other sides. A cross section of the strip waveguide design is given in Figure 2.1.

Core – n_{core} Cladding – n_{clad}

Substrate Cladding - n_s
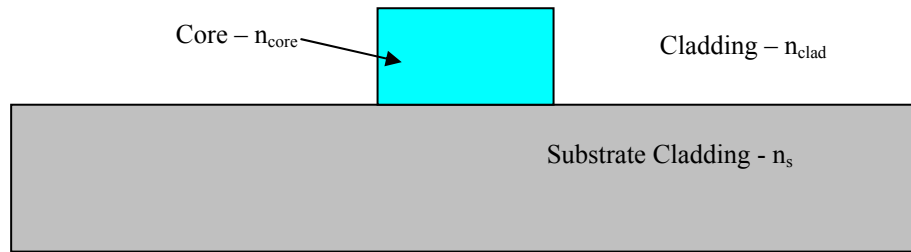
Figure 2.1: Cross section of the strip waveguide

The critical angle for total internal reflection limits the incident angles on the facet of a waveguide that will be bound within the waveguide. This "cone of acceptance" is defined by its half-angle, φ, which is given in Equation 2.2. [60] The numerical aperture can be though of as a cone extending away from the end facet of the guiding structure. Rays that are inside the cone are "bound" and propagate within the waveguide while those that strike the facet outside of the cone are radiated away from the waveguide. The light gathering capability that is determined by the cone of acceptance is more commonly given in terms of the numerical aperture, or N. A., which is also in Equation 2.2. The numerical aperture and cone of acceptance half-angle versus core and cladding index is plotted in Figure 2.2.

$$N.A. = n_0 \sin\phi = \sqrt{\left(n_{core}^2 - n_{clad}^2\right)}$$

The cone of acceptance has a strong influence on the optical coupling and efficiency of the system, as the following sections will reveal. For additional details of ray optics and refraction at dielectric interfaces, references [57,60 and 60] should be consulted.

Acceptance Angle (phi) vs. Core and Cladding Index
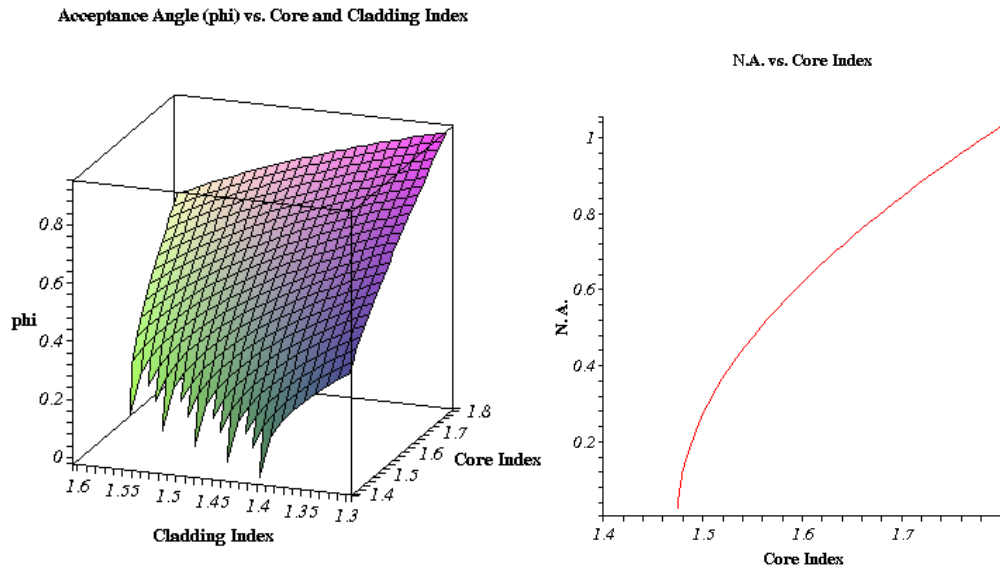
N.A. vs. Core Index

Figure 2.2: Left: N. A. versus Core and cladding optical index. Right: N. A. vs. Core Index for a fixed cladding index of Pyrex.

One of the chief design concerns for this device is the maximization of coupled power from the fluorescent emitter into the waveguide. The captured emission from a point source is subject to two constraints. First, the numerical aperture of the waveguide limits the angular extent of bound rays. The second limitation is the cross-sectional area of the waveguide. For sources close to the waveguide, the numerical aperture is the limiting

condition because the rays that fan out from a point source make larger angles with the end facet than the NA will accept. Sources that are located farther away from the waveguide make smaller than critical angles with the face of the waveguide and are thus subject to the cross sectional area limitation since the incident angles of a faraway source will be small. In coupling any optical source into the waveguide, the Brightness, "B" must be considered. The terminology for radiometry can vary. In some cases, the term Radiance may be used instead of brightness to emphasize the quantitative nature of the measurement. Brightness is given in terms of the optical flux radiated into a unit solid angle per unit area of emission (Flux Area^{-1} Sr^{-1}). Generally, the emission pattern for a source is given in spherical coordinates. The coordinate system used for this analysis is given in Figure 2.3. A Lambertian source is characterized with a radiation pattern of $B(\theta, \varphi) = B_0 cos(\theta)$. This means that a point on the surface emits equally in every direction, but the intensity falls off when viewing at an angle because the projected surface area is diminished. This radiation pattern is characteristic of LEDs that produce photons via spontaneous emission, and with diffuse reflections. Lasers and specular reflectors, on the other hand, are a good example of non-Lambertian sources. A power coupling calculation involves the brightness of the source integrated over the source area and the solid angle of the cone of acceptance. For sources close enough to the waveguide to be subject to the NA limit, this calculation is given in Equation 2.3.[58] First, the brightness of a point on the source, represented by $B(\theta, \varphi)$ is integrated over the solid angle of the cone of acceptance, where θ_{max} is the maximum angle of acceptance. Assuming a circular cross section for the emission sets the limits of the integration over φ as 0 to 2π. Next, the expression outside the brackets integrates over the entire surface area of the

47

emitter, summing the contributions of each infinitesimal area $d\theta_s\, r\, dr$ on the surface. The limits of integration are set for a circular emitting area of radius r_m in the case where the source area is less than the waveguide cross sectional area. In the case where the source is larger, r_m should be set to the waveguide radius. This calculation is, in general, dependent on the distance between the source and the waveguide. For isotropic sources far enough away from the waveguide facet such that the impinging angles are all smaller than critical, the ratio of emission area to area of the waveguide facet area will yield the fraction of coupled power.
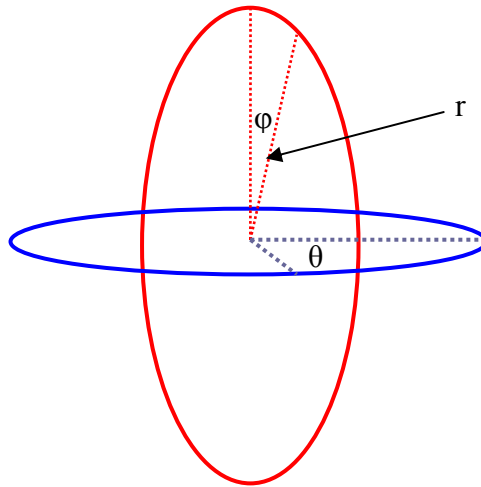
Figure 2.3: Spherical coordinate system used for this analysis. φ is the polar angle and θ is the longitudinal angle while r is the radius.

Equation 2.3

$$P = \int\limits_{A_f}\int\limits_{\Omega_f} B\!\left(A_s, \Omega_s\right) d\Omega_s\, dA_s$$

$$P = \int\limits_{0}^{r_m}\int\limits_{0}^{2\pi}\left[\int\limits_{0}^{2\pi}\int\limits_{0}^{\theta_{0,max}} B(\theta,\phi)\sin\theta\, d\theta\, d\varphi\right] d\theta_s\, r\, dr$$

48

For the purposes of analyzing the designs in this section, we will take the approach of calculating the cross-section of captured emission of a point source located at the center of the sensor's active area and express the cross-section as a pure number which will be the fraction of the total emission. In this case we will consider the emission of a point source with a uniform spherical intensity. This could be the radiation of a single molecule, although the radiation pattern of a single molecule is toroidal as that of a dipole antenna. [13, 48] With many randomly oriented molecules excited by randomly polarized light, making the spherical assumption reasonable to ascertain the capture cross-section.

2.2.2 Initial Candidates

Initially, three design candidates emerged that fulfill the goals of the chitosan-based biosensor. They were named the C-Cell, Z-Cell and I-Cell, corresponding to the geometry of their optical paths. Figure 2.4 illustrates each of these designs.

a) I-Cell
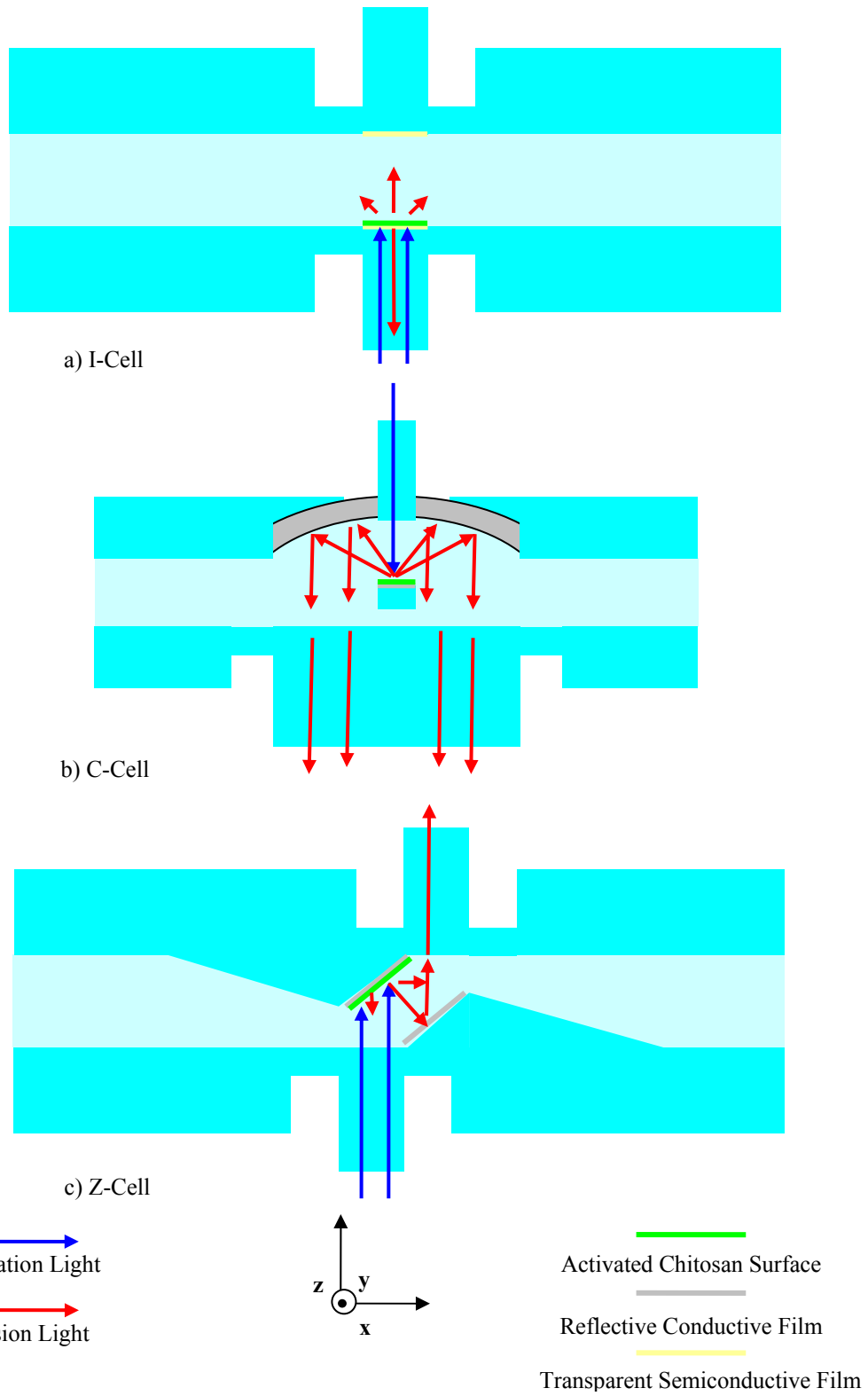
b) C-Cell

c) Z-Cell

Excitation Light

Emission Light

Activated Chitosan Surface

Reflective Conductive Film

Transparent Semiconductive Film

Figure 2.4: Fluorescence Detection Cell Design Candidates: (a) I-Cell, (b) C-Cell, (c) Z-Cell

2.2.2.1 I-Cell

For the I-Cell, the emission source is located close to the end facet of the waveguide. The critical angle of acceptance θ_c is given by Equation 2.2 and related to φ in the construction of Figure 2.5. The design parameters are given in Table 2.1. A sequential application of Snell's Law of the marginal ray captured by the waveguide is shown. Geometrical analysis shows that when the point source is located from the end facet of the waveguide with a distance greater than d, the limiting factor is the cross sectional area of the end face of the waveguide since all the rays from the point source will make angles smaller than φ at the end facet. On the other hand, for separation distances less than d, the constraint will be the numerical aperture of the waveguide. The expression for d for that limiting condition on the circular cross sections is given in Equation 2.4.

Equation 2.4

$$d = \frac{L}{2 \tan \phi}$$

Table 2.1: I-Cell Design Parameters

Variable	Parameter	Value
w_w	Waveguide width	150 μm
w_c	Channel Width	200 μm
L	Thickness of the Polymer	130 +/- 13 μm
q	Distance between surface and waveguide start	
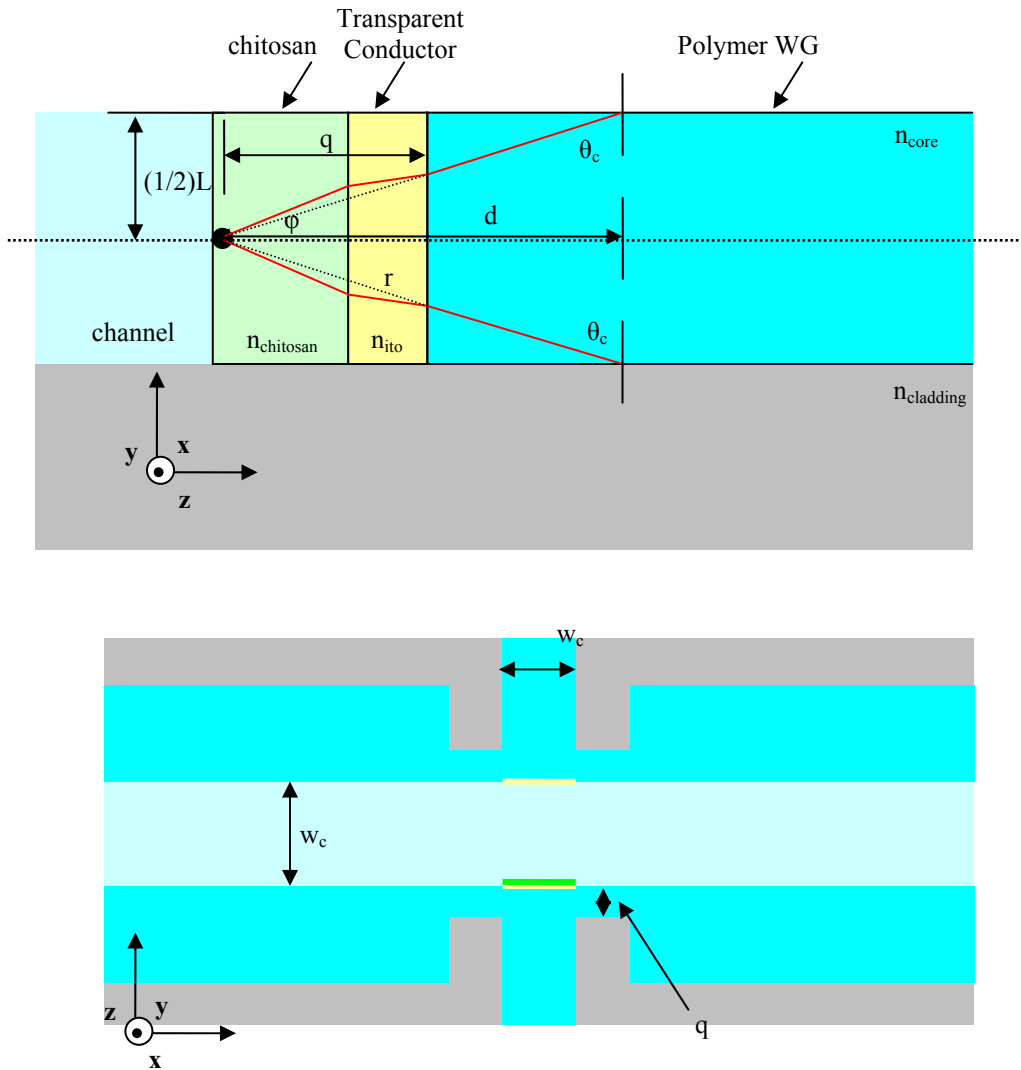
Figure 2.5: Construction for finding the cross section of the I-Cell. A sequential application of Snell's Law for the marginal ray captured by the waveguide is shown.

For a SU-8 polymer core and Pyrex cladding d is 154 μm and in this case the separation between source and facet (q) is expected to be less than d. As long as q is less than d, the numerical aperture will limit the cross-section. The calculation involves finding the solid angle. The formula for the surface area of a sphere in spherical coordinates is given in

Equation 2.5. Integrating θ from 0 to 2π, and φ from 0 to π yields the expected formula

for the total area, $4\pi r^2$.

Equation 2.5

$$\sigma_{wg} = \int\limits_{\theta_1}^{\theta_2}\int\limits_{\phi_1}^{\phi_2} r^2 \sin\phi \, d\phi \, d\theta$$

To determine the cross section, it is first necessary to determine the limits of integration

on θ and φ. We take r to be 1 for the unit circle. Finding r can be obtained by the

construction in Figure 2.5 although the solid angle is invariant with respect to the radius

of the sphere. The limits of integration are given in Equation 2.6. The dimensions of the

waveguide and the fact that the cross section of the waveguide is rectangular instead of

square does not influence limits of the integral because it does not expand the cone of

bound rays of a point source, but it increases the facet area, or propagation distance

between internal reflections, and d.

Equation 2.6

$$\frac{\pi}{2} - \phi_{max} \le \phi \le \frac{\pi}{2} + \phi_{max}$$
$$0 \le \theta \le 2\phi_{max}$$

For the design, it is assumed that the source surface area is at least as large as the

waveguide's surface area. A radiometric calculation as in Equation 2.3 would involve

finding the cross section at every point and integration across the source's area.

Essentially, the dimensions of the waveguide do not affect the efficiency for a point

source, rather, they add additional contributions of point sources if the emission area is

matched to the waveguide facet area. Larger area cores capture more of the off-axis

points. Figure 2.6 plots the capture cross section in terms of the capture efficiency for the I-Cell with varied core and cladding indices.
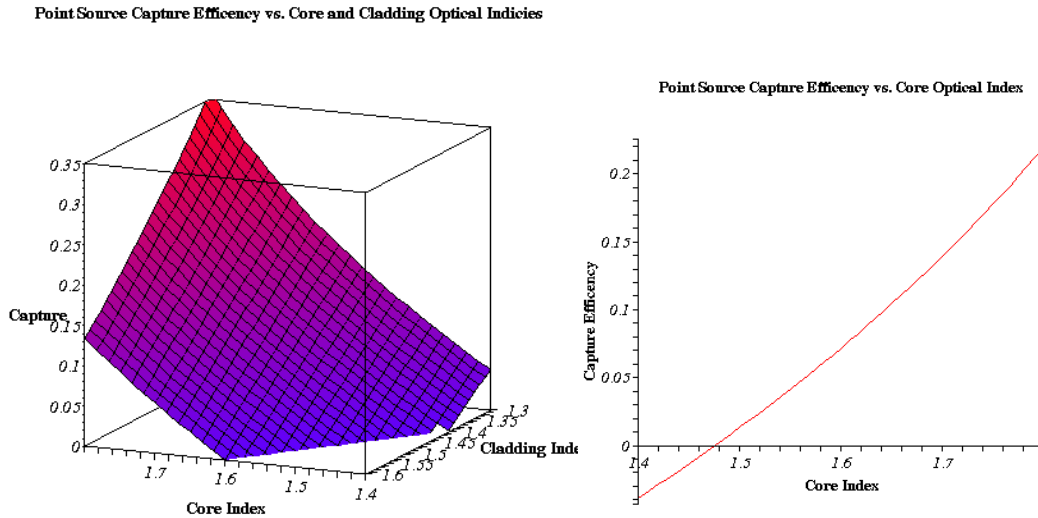

Figure 2.6: Point source capture efficiency for the I-Cell for (Left) Core and Cladding optical indices and (Right) Core index with fix cladding index of Pyrex.

In addition to the geometric losses associated with the capture cross section, light is lost by absorption, scattering, and reflection.

Reflection occurs at the dielectric interfaces between the chitosan and the transparent conductor, and the transparent conductor and polymer waveguide. The reflective losses vary slightly in each design implementation and can be predicted in advance. The Fresnel equations describe the reflection that occurs at dielectric interfaces. The reflection depends on the angle of incidence, polarization, and direction of the reflection (external or internal). Equation 2.7 gives the Fresnel reflection from a dielectric interface. [60] Since the cone of acceptance makes relatively small angles with the interface, we can use the normal incidence equation as a good approximation.

Equation 2.7

$$R = \left(\frac{1 - \dfrac{n_2}{n_1}}{1 + \dfrac{n_2}{n_1}} \right)^2$$

Table 2.2: Reflection at normal incidence.

Interface	*Reflection*
Chitosan – ITO	2%
ITO – SU-8	1%
Water – SU-8	0.9%
Chitosan – Water	0.4%

It is important to note that resonant cavity, e.g. a Fabry-Perot etalon, would be formed if the reflectances were high. This would result in wavelength dependent comb-filter effects. The reflectances here are very low, so Fabry-Perot effects can be neglected. Essentially, it can be regarded as an etalon with extremely low Finesse.

Absorption occurs in the volume of the chitosan, the transparent conductor, and polymer waveguide. Absorption in the solution is generally negligible. Most of the losses due to absorption will be due to the polymer waveguide which is not part of the cell design. The absorption in the Chitosan will mainly be due to re-absorption by neighboring fluorophores and will depend on analyte concentration. It will be similar for all of the designs. The I-Cell, however, has the transparent conductor layer whose absorbance is not negligible. Commercially available ITO (a readily available transparent conductor) coated slides from Fisher Scientific have transmission of 96%. For a first consideration in the design phase, we will take this into account.

The practical reality of fabrication always introduces sources of scattering that may arise in the volume of the waveguide (volume scattering) and roughness on the surface of the waveguide (surface scattering). The magnitude of surface scattering's contribution to total loss is decreased with an increasing waveguide cross-section area to perimeter. So, the 400 μm waveguide will have less propagation loss than the others. In general, the magnitude of scattering effects are not known *a priori* and will be left for analysis in the Fabrication and Testing sections.

Another important goal in the design is the elimination of backreflection (or backscattering) of excitation light. For fluorescence analysis, any excitation light that reaches the detector or spectrometer is noise. Since the fluorescent cross section is low, and the actual conversion of excitation light to emission light is also in the tens of percent, even small percentage values of backscattering can completely overwhelm the emission signal. The spectral separation of the excitation and emission means that they can be selectively attenuated with interference or other filters. No filter is perfect, however, and even filters with high out-of-band attenuation may not bring the excitation intensity down below the emission intensity in conditions with high backreflection. It is important to observe that the same effects that cause loss of the excitation light by reflection also cause backreflections of the excitation light. This design minimizes backreflection by using a reflective mode of signal collection where the backscattered fluorescence is collected by the waveguide and the excitation light propagates away from the collector waveguide.

Table 2.3 presents the theoretical efficiency of the I-Cell as 6.78%. This means that fraction of the emission will make it to the waveguide, but does not count the propagation loss through the waveguide or the rest of the system.

Table 2.3: Theoretical Efficiency of the I-Cell

Aspect	*Efficiency*
Cross Section	7.26%
Chitosan – ITO Transmission	98.3%
ITO – SU-8 Transmission	98.9%
ITO Absorptive Transmission	96%
Efficiency into Waveguide	**=6.78%**

Figure 2.7 shows the L-Edit mask implementation of the I-Cell. This design is the result of several iterations and does not include a waveguide for transmission type measurements. The measurement method will be discussed in Chapter 4.
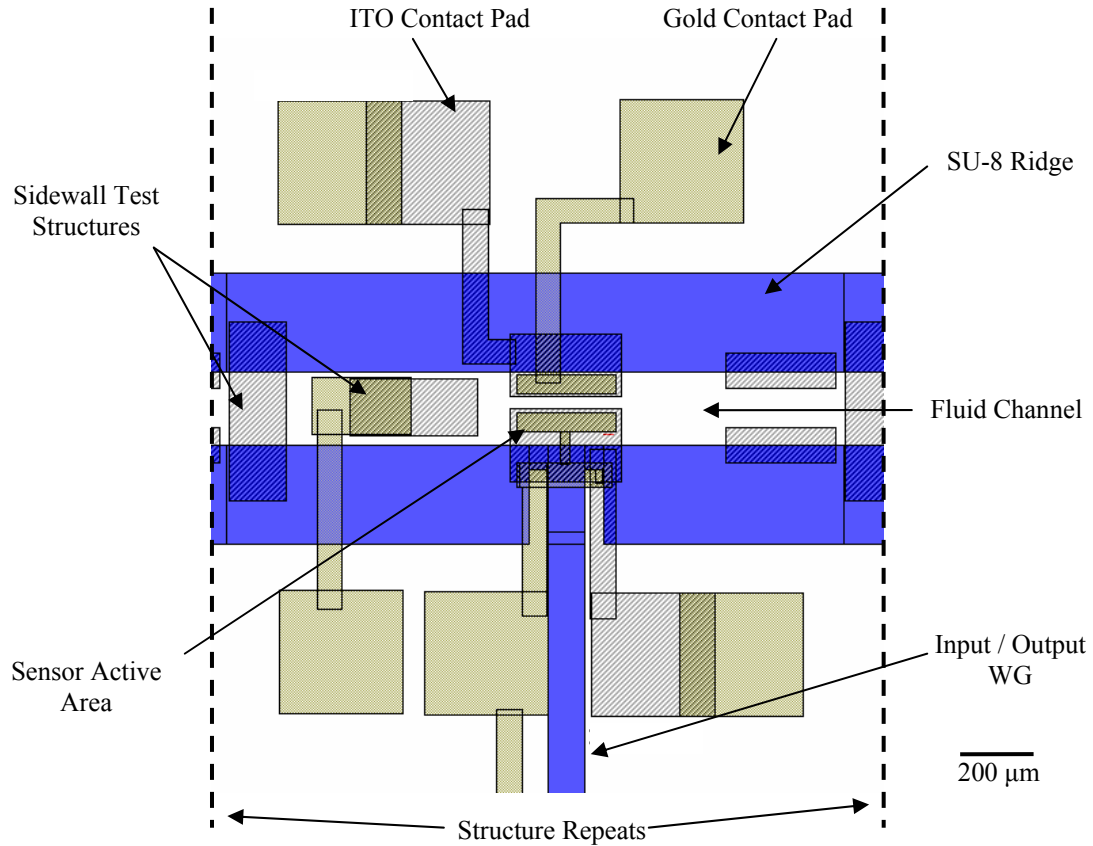
Figure 2.7: L-Edit mask implementation of the I-Cell.

2.2.2.2 C-Cell

The C-Cell in Figure 2.4a is named such due to the cylindrical mirror that is placed in front of a chitosan coated polymer "pedestal" located in the middle of the fluid channel. The pedestal is located at the focal point of the mirror. Basic ray optics dictates that rays from the focal plane will be collimated by the mirror. The focal point equation is given in Equation 2.8. [59, 60] The focal length of the mirror used in this design is 150 μm.

Equation 2.8

$$f = -\frac{R}{2}$$
$$R < 0 \; concave$$
$$R > 0 \; convex$$

58

The purpose of this mirror is to collect the emission and collimate the rays to send through a large output waveguide which is 400 μm in width, corresponding to the diameter of the mirror. The excitation light is delivered through a smaller waveguide, 50 μm in diameter, which interrupts the mirror. Sidewall mirrors on polymer structures have been proven to be feasible in a number of applications in the literature [61, 62]. The design parameters for the C-Cell construction in Figure 2.8 are given in Table 2.4.

Table 2.4: C-Cell Design Parameters. Material parameters are not included.

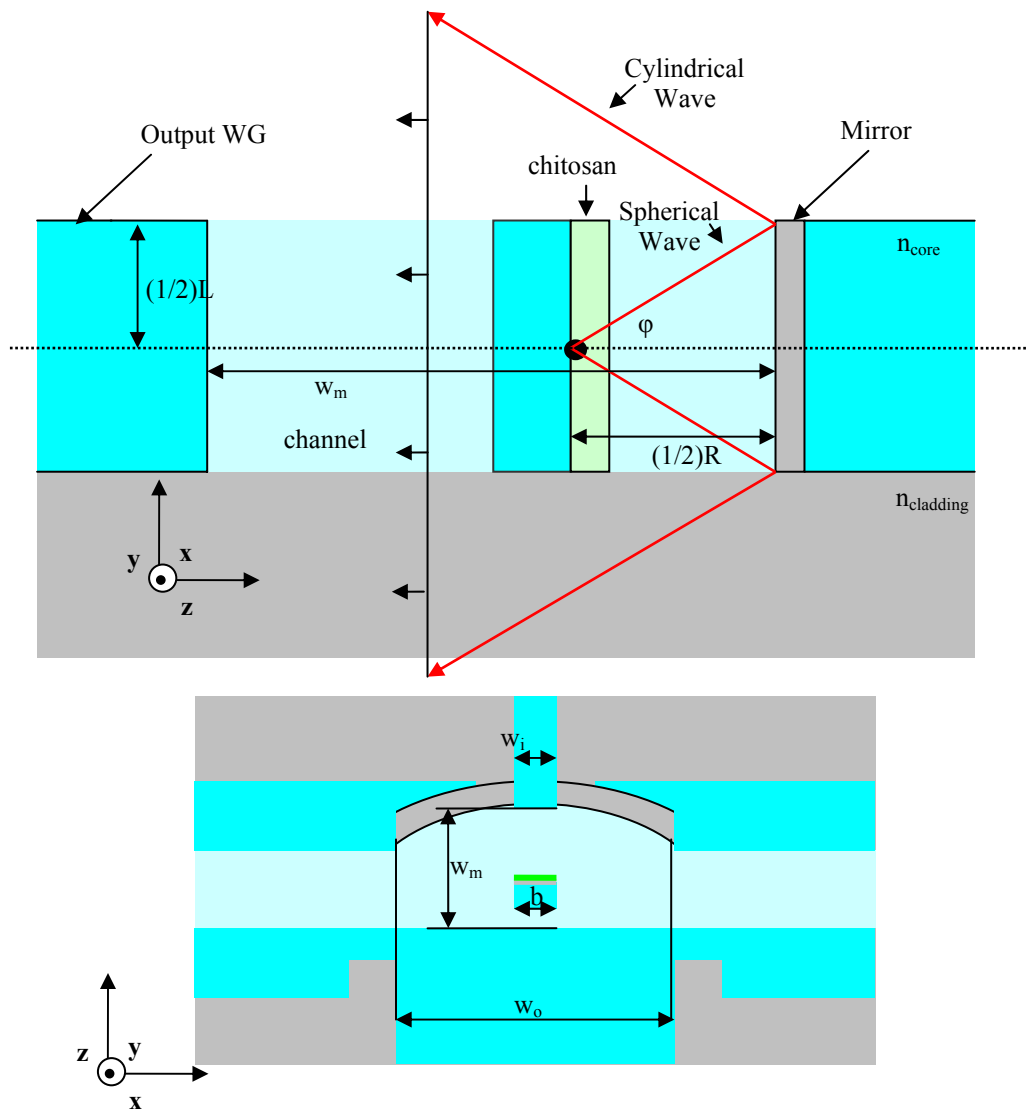| *Variable*	*Parameter*	*Value*
R	Mirror Radius of Curvature	300 μm
L	Thickness of the polymer	130 +/- 13 μm
w_i	Width of input waveguide	50 μm
$w_o = c_h$	Width of output waveguide	400 μm
w_m	Fluid channel width from mirror to waveguide	400 μm
b	Chitosan pedestal width	50 μm

Figure 2.8: (a) Top: The side view construction to find the cross-section of the C-Cell. (b) Bottom: The top view showing collimation of the beam in the x direction. It is important to note that the focusing of the mirror changes the emission from a spherical wave to a cylindrical wave incident on the waveguide facet.

Determining the cross section is a multi-step process. The mirror first collects and collimates the beam in one axis with one cross section, and then the waveguide captures the astigmatically focused beam with a secondary cross section. The beam radius

exceeds d so the capture cross section is determined by the wavefront's incident area. The area of a spherical wavefront and the cross section subtended by the spherical mirror is given in Equation 2.9. The chord of the reflector is c_h and the radius of curvature is R.

Equation 2.9

$$A_{wave} = 4\pi \left(\frac{R}{2} \right)^2$$

$$A_{mirror} = 2RL \arcsin \left(\frac{c_h}{2R} \right) - w_i L$$

$$\sigma_{mirror} = \frac{A_{mirror}}{A_{wave}}$$

The design parameters used here allow the mirror to collect 16% of the emission. Unfortunately, since the mirror is cylindrical and not spherical, the reflected wave will continue to diverge along the axis of propagation before it is captured by the waveguide. This divergence results in an expansion of the beam in the y direction while the x direction is collimated. The angle of expansion can be taken to be the angle from the source that subtends the reflector. The divergence half angle and coupling cross section is given in Equation 2.10 and depicted graphically in Figure 2.8a. Here, w is the distance between the center of the mirror and the waveguide end facet.

Equation 2.10

$$\phi = \arctan \left(\frac{L}{R} \right)$$

$$\phi = \arctan \frac{\dfrac{L_w}{2}}{\left(\dfrac{R}{2} + w_m \right)}$$

$$\sigma_{wg-capture} = \frac{L}{L_w} = \frac{R}{2R + w_m}$$

The waveguide's capture of the mirror's reflection is 30% for this design. The cross

sections of the mirror and the waveguide must be multiplied for the total.

From off-axis sources, the resultant plane wave in x from the reflector will be angled with

respect to the optical axis. By ray tracing the chief ray, this angle for objects off axis by

dimension b is given in Equation 2.11.

Equation 2.11

$$\beta_{max} = \arctan\left(\frac{2b}{R}\right)$$

The constraints on the pedestal width (2b) are the obstruction to the reflected wave and

the acceptance angle of the waveguide, which should not be exceeded by β_{max}. The

efficiency of the C-Cell can be taken to be the product of the mirror's cross section

fraction of the entire wave, the waveguide capture cross section of the reflected wave,

and the transmission through the dielectric interface minus the reflective losses. Table

2.5 gives the efficiency of the C-Cell for the design parameters.

Table 2.5: Efficiency of the C-Cell.

Aspect	Efficiency
Mirror Cross Section	16%
Waveguide Cross Section	30%
Mirror Surface Transmission	100%
Water – SU-8 Transmission	91%
Chitosan – Water Transmission	96%
Efficiency into Waveguide	=4.19%

The analysis here neglects the surface imperfections of the mirror. Practically, this will

not be the case since the metal layer is not a perfect conductor and surface roughness will

have a diffuse scattering effect. Also, the size of the output waveguide produces

operational difficulties. The waveguides in the I-Cell and Z-Cell are well matched in aspect ratio to optical fiber, but the output waveguide of the C-Cell is not. Collection optics would likely have to be used in this case to bring the light into a fiber or detector.

The L-Edit mask implementation of the C-Cell is given in Figure 2.9. It is important to note the relative dimensions of the waveguide and the chitosan pedestal in the center of the channel. The pedestal and the curved surface of the mirror causes obstructions in the fluid flow.
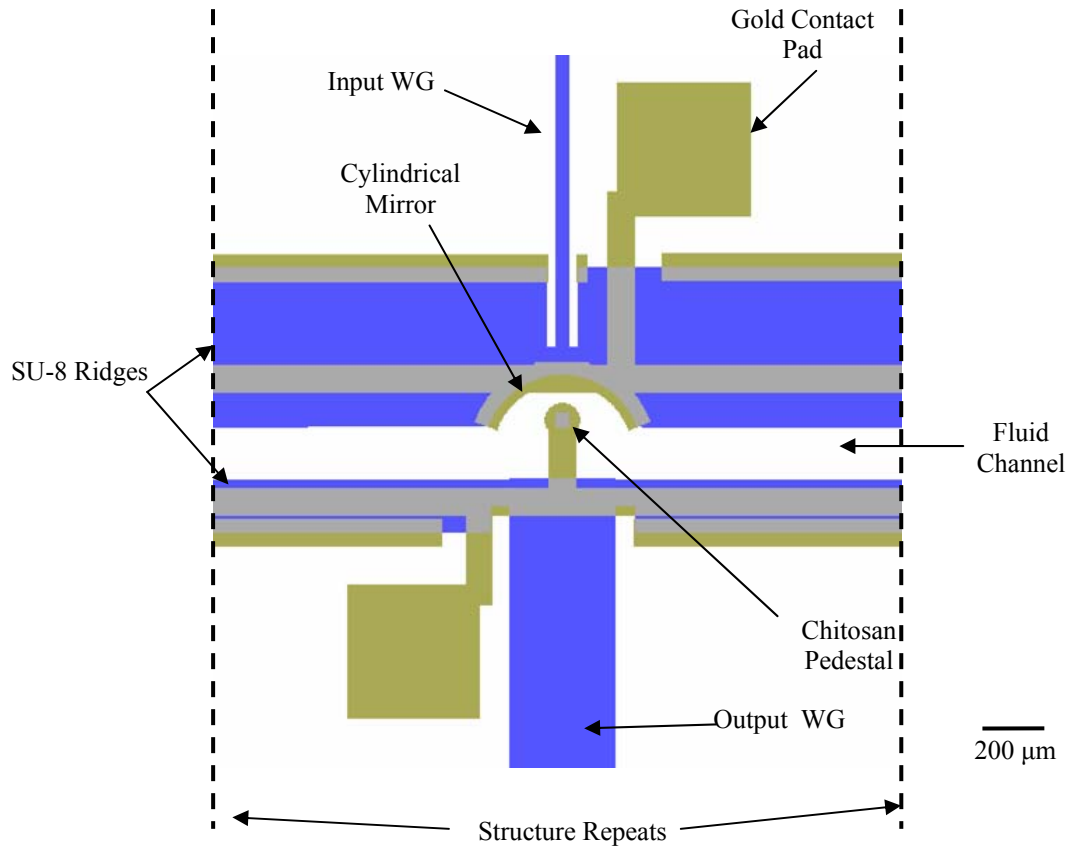

Figure 2.9: L-Edit mask implementation of the C-Cell

2.2.2.3 Z-Cell

The analysis of the Z-Cell follows closely from that of the I-Cell with a few significant exceptions. First, the device operates outside of the NA limit. Also, some additional losses are introduced such as mirror reflectivity. Assuming a spherical wave emanating from the chitosan surface, the point-source efficiency is the cross-sectional area of the waveguide divided by the total area of a spherical wave at the distance of the waveguide's facet from the emission point as given in Equation 2.12 and Figure 2.13.

Equation 2.12

$$\sigma_{eff} = \frac{w_w L}{4\pi r^2}$$

The design scheme is shown in Figure 2.10, and their respective values are given in Table 2.6.

Table 2.6: Z-Cell Design Parameters

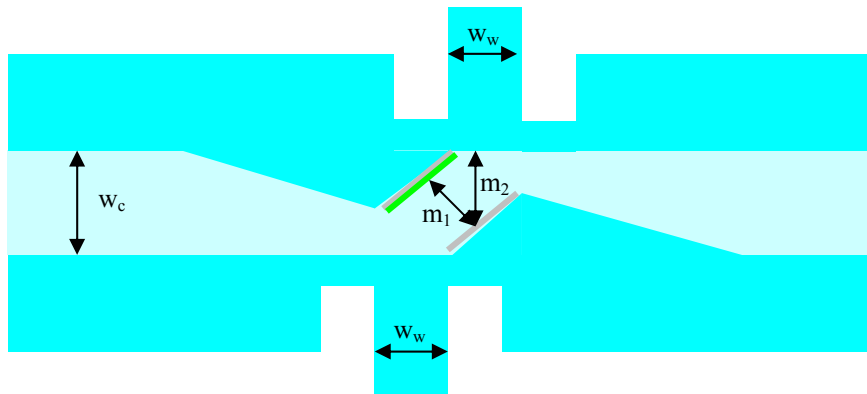| *Variable*	*Parameter*	*Value*
w_w	Waveguide Width	150 μm
L	Thickness of the polymer	130 +/- 13 μm
s	Chitosan and mirror width	212 μm
w_c	Width of fluid channel	300 μm
m_1	surface to mirror separation	210 μm
m_2	Mirror to waveguide separation	230 μm

Figure 2.10: Dimensions for the Z-Cell. The side view is a folded version of the I-Cell.

The L-Edit mask implementation is given in Figure 2.11, and like the C-Cell it is important to note the obstructions introduced by the optical components in the channel. The efficiency calculations are produced in Table 2.7.
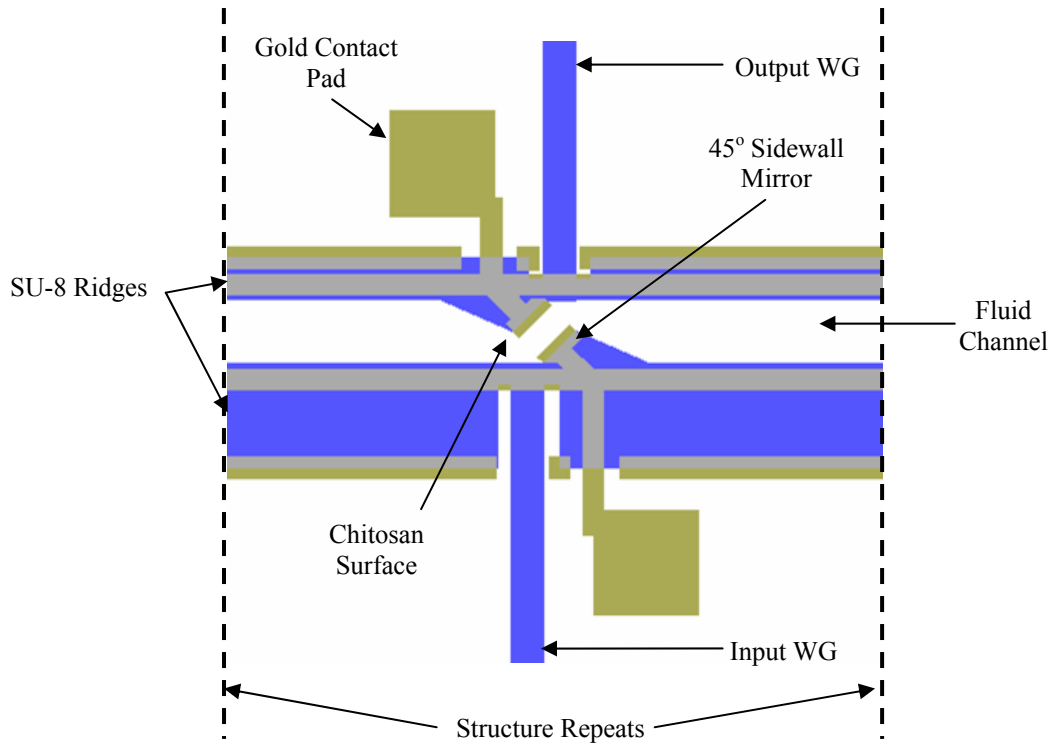
Figure 2.11: L-Edit mask implementation of the Z-Cell

Table 2.7: Efficiency of the Z-Cell

Aspect	*Efficiency*
Cross Section	0.8%
Mirror Surface Transmission	100%
Water – SU-8 Transmission	91%
Chitosan – Water Transmission	96%
Efficiency into Waveguide	**=0.70%**

The efficiency of the Z-Cell unfortunately turns out to be quite low, even when 100%

reflection is assumed which is not reasonable to assume in practice.

2.2.2.4   Some Experimental Alternatives

In the course of solving some operational difficulties, alternative designs emerged. The S-Cell is pictured in Figure 2.12. The idea behind the S-Cell was to eliminate the backreflections that are caused at the end-facet of the waveguide and improve performance without having to use a beamsplitter or directional coupler to separate the forward and backward propagating light. It turns out that in practice this design did not reduce the backscattering, but actually experienced worse effects which were likely the result of cross-coupling between input and output waveguides.

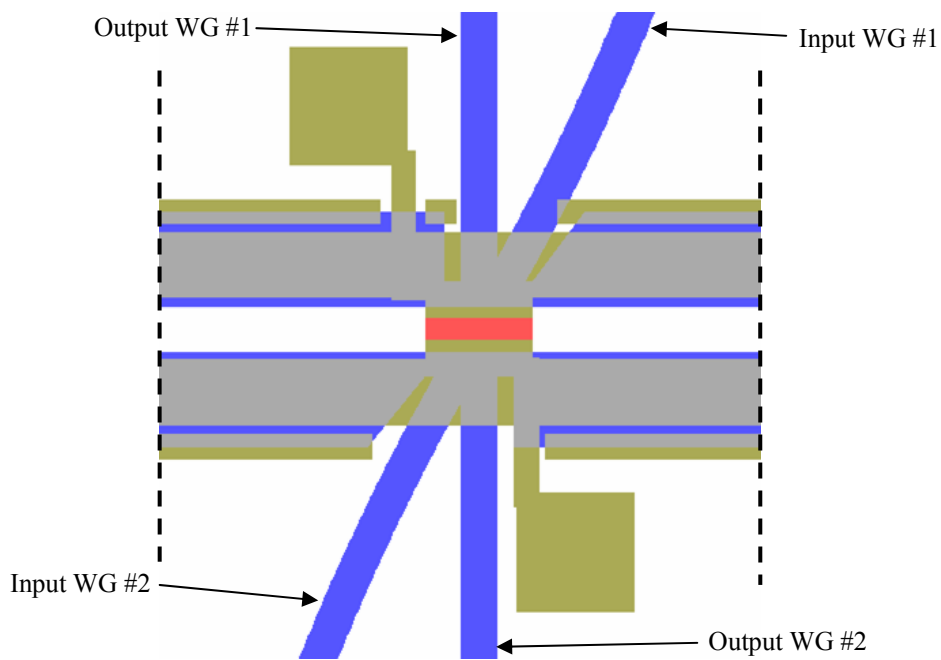**Figure 2.12: L-Edit mask implementation of the curvy S-Cell**

2.2.3 Final Design

The efficiencies of the designs may seem small in absolute terms, however this is not unusual, unexpected, or unmanageable. For example, an LED constructed with a

semiconductor material of index 3.3, the solid angle for emission out of the surface into air is a mere 0.3 sr due to the internal reflections that occur at higher angles. [63] The efficiency for photons escaping from the electron hole recombination points is then around 3%, lower than what is calculated for the I-Cell. Yet, despite these inherent physical inefficiencies, LEDs are a very successful technology. Furthermore, considering these devices as parts of a system, reveals that their efficiency is not the weakest link. Argon ion lasers frequently used for biophotonics have wall plug efficiencies of 0.01%. [56] Low brightness and low capture cross sections for fluorescence will always be an issue due to the fact that the emission is spontaneous.

Because the I-Cell satisfies all of the design goals outlined in Section 2.2 better than the alternatives, it was selected as the design to progress to the fabrication and testing phase. A perspective view of the device is shown in Figure 2.13.
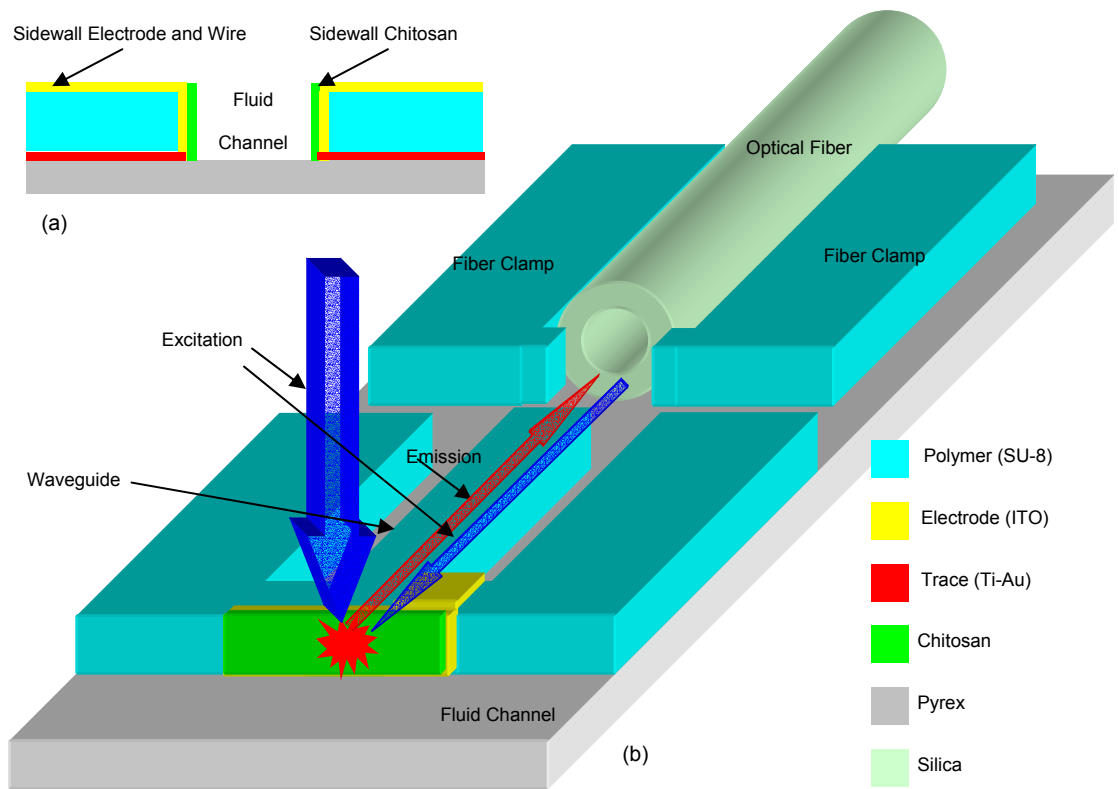
Figure 2.13: (a) Cross-section of the device intersecting the fluidic channel. (b) Perspective view of the integrated optical device. The fluorescent excitation light shown by the blue arrows can be delivered from the top-down or from the optical fiber.

2.3 Optical and Electrical Interface Design

In this photonic device, both an electrical and optical interface had to be designed that would be compatible with the testing equipment and with the biology of the experiments. Through some insight and trial-and-error, a simple and flexible design developed to facilitate interconnection with external instruments.

2.3.1 Fiber Clamp Structure

After several preliminary experiments with free-space optical coupling to the waveguides, it was determined that using an integrated fiber-optic approach was far better as it improved the robustness of the test setup, reduced the collection of stray light, improved the consistency of source and detector coupling to the waveguides, and decreased the amount of time required to test an array of sensors. Following from some similar structures reported in the literature [28], "fiber clamp" structures were developed by Arne Schleunitz as shown in Figure 2.14. [74] The spacing for the clamp was first approximated by the fiber diameter, however some empirical adjustments had to be made due to the dimensional change of the polymer during processing. Mechanical stops were implemented to prevent the silica fiber from damaging the facet of the polymer waveguide while still maintaining an unobstructed aperture for the core.
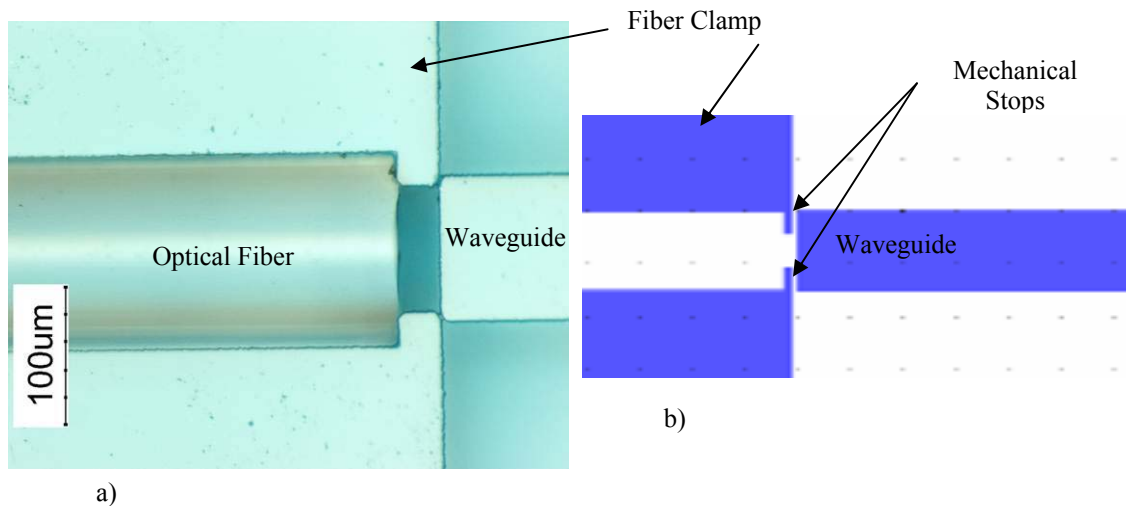

Figure 2.14: Fiber Clamp Structures: (a) Left: Micrograph of a fiber clamp structure, waveguide, and optical fiber. (b) Right: L-Edit drawing of the same structure.

2.3.2 Electrodes

The electrode structure is important to this design because it serves as the interface for chitosan deposition. Previous work with chitosan has involved the use of gold patterned electrodes. Gold is a good material of choice due to its noble metal status in that few chemicals will react with it. For the C-Cell and Z-Cell, which allow chitosan deposition on an opaque surface, gold is the material of choice. For the I-Cell, indium tin oxide (ITO), a transparent semiconductor, is used. Further details of ITO are given in Section 3.3.4. Figure 2.15 displays the contact pad arrangements used in this work. Depending on the situation, large area pads were designed when depositing chitosan on up to 10 sensors simultaneously, or micro-contact pads were used with micropositioning probes for deposition on up to 3 sensors on a chip. The actual deposition method will be described in Chapter 4.
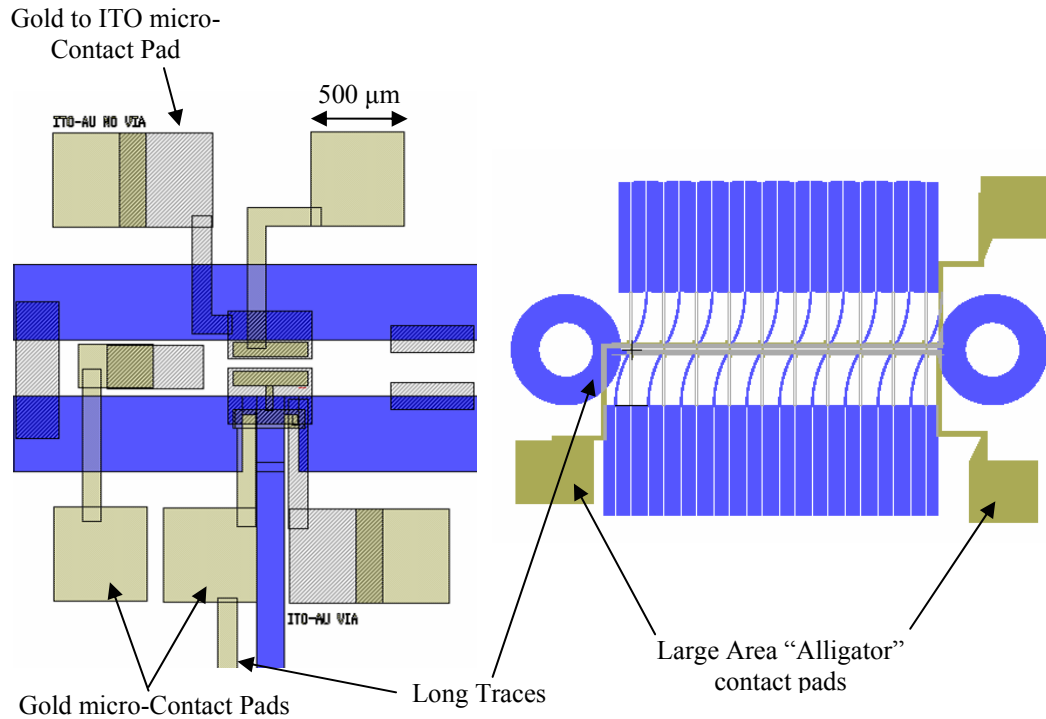
Figure 2.15: Two contact pad arrangements

Early on, it was found that thin ITO traces on the Pyrex substrate were not able to carry large amounts of current. In effect, ITO traces of about 300 μm in width were found to act as fuses. To prevent this, a gold-ITO combination was used. Long traces were implemented in gold, but the transparent electrodes and local traces were implemented with ITO. ITO was found to make good electrical contact with gold. Although the Ohmic or Shottky properties of the contact were not characterized, no operational difficulties were observed. The design in Figure 2.15 employed a "design-for-test" methodology, as more contact pads were designed than necessary to check the continuity and contact resistance between gold and ITO.

2.4 Fluidic Design

The fluidic design in this sensor is relatively straightforward. Channels with square cross sectional profiles were created using the same layer of polymer used in defining the waveguides. Thus, the depth of the channel was constrained to the height of the waveguide. As mentioned previously, the height of the waveguide was determined by the outer diameter of optical fiber, so this dependency is transferred to the channel depth. The channel width was determined by the fabrication restrictions of the device processing. Initially, a 100 μm width was designed. Due to difficulties in the sidewall recipe, the channel width was expanded to 200 μm. Thus, the fluid channel properties did not drive the design considerations.   Basic fluid structures were designed to aid in the testing, such as the reservoir structure in Figure 2.16. This was found to be a useful way of sending fluid through a temporarily sealed channel. When a glass slide was placed overtop the channel and a drop of solution was placed in the reservoir, capillary action moved the fluid through the channel.
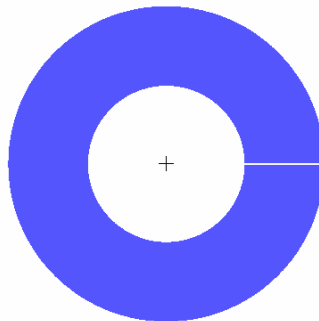

Figure 2.16: Fluid Reservoir Structure

During the course of this study, the channels were not sealed because the focus of the work was on the fabrication process and optical testing. Sealing the channel would be the next step in testing a full microfluidic system.

2.5 Biorecognition Element

By definition, a biosensor is able to detect the bio-properties of its environment through the action of some biorecognition element. In this case, the biorecognition element is single-stranded DNA (ssDNA) that is described in Section 1.4 and previously in literature. [42] Essentially, all biosensors must be specific to a particular target. Through the strong and highly specific affinity of matching ssDNA strands, the biorecognition element selected for this work fulfills this purpose very well. The location of the element, on the sidewall of the device, increases its optical interaction.

The fluorescent detection element is an important part of the system to be considered at the design stage. The key properties of a fluorescent element are its absorption maximum and bandwidth, emission maximum and bandwidth, and quantum efficiency. The quantum efficiency is highly dependent upon the environment, and changes with different coupling. Although not known *a priori,* the luminescent parameters influence the total light output. Sufficient fluorophores must interact with the excitation light to produce appreciable emission. The Signal to Noise Ratio (SNR) ultimately determines the sensitivity of the device. As a starting point, it is good to begin with the maximum reasonable area.

3 Fabrication

Although the fabrication of this device is based on techniques that were originally developed for VLSI microelectronics, this process involves some unorthodox fabrication methods including the pattering of ITO on thick sidewalls, integration with biological components, and the use of polymers which have temperature and other limitations. Materials compatibility has been a critical issue throughout the design, development, and fabrication process. This section details the fabrication process flow, including each process step, the final results, and the methods used to obtain those results.

3.1 Materials

The selection of materials is critical in MEMS since each material must be compatible with one another not just in the device, but during fabrication as well. The mechanical, electrical, and optical characteristics must all be considered in varying degrees. For BioMEMS, the additional aspect of bio-molecular functionality must also be considered.

3.1.1 Substrate

The substrate serves as the basis for all of the surface micromachining that will define the functional structures. It must exhibit the following properties:

1. Low Optical Refractive Index – Lower index materials increase the numerical aperture and collection efficiency of the waveguides.

2. Good Adhesion to Polymer Materials – Robust ability to be used with a variety of polymer materials.

3. Rigid – Flexible substrates can be difficult to process.

4. Tolerance of High Temperatures and Ultraviolet Light – The substrate must withstand all of the processing conditions of the device without degradation.

Several possible substrates were considered, including Pyrex (Borosilicate Glass), Kapton, and silicon with a cladding of BCB. In terms of refractive index, Pyrex is about 1.47 which is less than many polymers that could be used for waveguides. Kapton, on the other hand, has a high refractive index that makes it unsuitable as a cladding material. Although Silicon has a high refractive index of 3.5, cladding with BCB which has a lower refractive index can make this a suitable option. In terms of adhesion, this is not often known before hand and depends on processing. All of the options considered could be made rigid at some acceptable thickness, and all can tolerate high temperatures for processing and ultraviolet light. Ultimately, Pyrex was selected because it had the lowest refractive index of all of the options and is transparent at visible wavelengths making it compatible with transmission microscopes.

3.1.2 Waveguide / Fluid Channel

A single layer of polymer material was chosen to define the fluid channel, waveguides, and fiber clamp structures. A polymer material is easier to define with inexpensive equipment than patterning silica, silicon nitride, or other materials typically used as integrated waveguides. A wide variety of polymers exist for defining the waveguide and fluid channels. Only photopatternable polymers were considered due to the ease of processing and the fact that these polymers exhibit lower sidewall roughness versus dry-etch process materials. Roughness increases the transmission loss in the waveguide. The desirable aspects for this material include:

1. High Index – High index increases the numerical aperture and light gathering efficiency of the waveguides

2. Low Loss – Minimal absorption at visible wavelengths is required for efficient operation.

3. High Thickness – Polymer must be available in high viscosity formulations for formation of layers of about 130 μm for the purposes of fiber optic integration and active sensor area (See Chapter 2).

4. Good Sidewall Characteristics – Formation of vertical sidewalls necessary for sidewall mirrors and vertical sidewall patterning.

5. Chemical Inertness – Non-reactivity with biological agents and processing chemicals.

SU-8, BCB, PMMA, Polyamide, PDMS, and OptiNDEX [64] polymers were considered for this application. PDMS was ruled out due to its low refractive index (1.43) and PMMA was ruled out due to its hazardous solvent (Chlorobenzene).   The refractive indices of some of the candidates are shown in Figure 3.1.
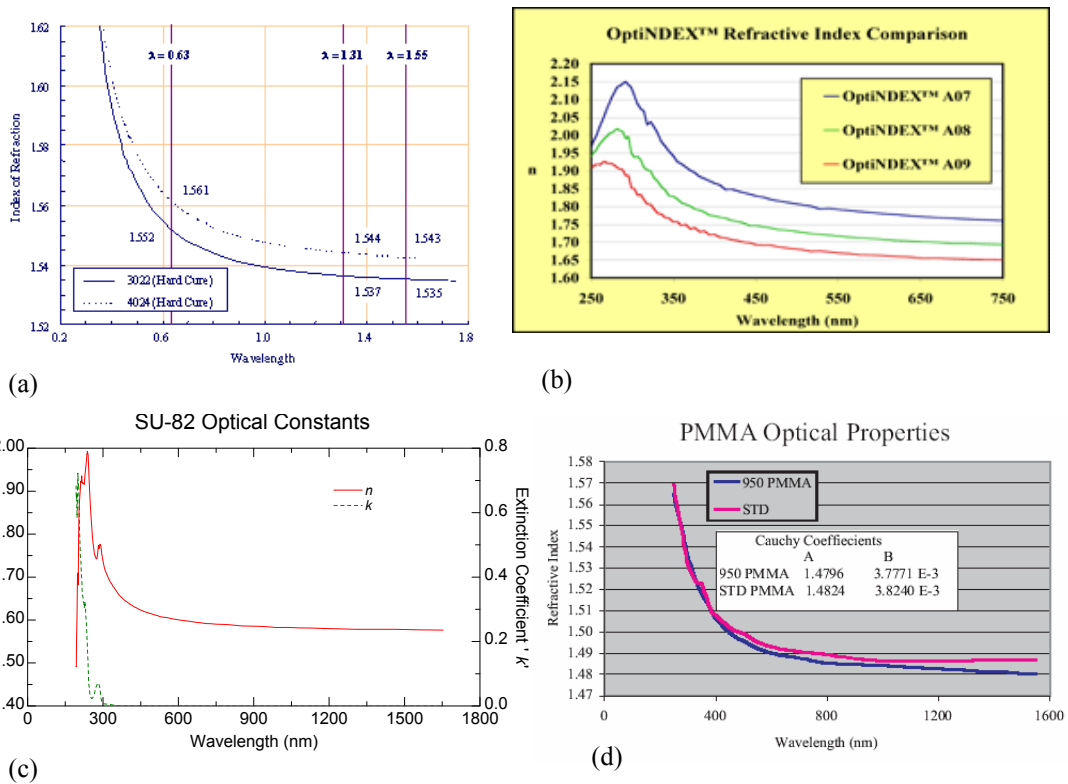
(a)

(b)

(c)

(d)

Figure 3.1: Refractive indexes versus wavelength for (a) BCB [65], (b) OptiNDEX [64], (c) SU-8 [66], (d) PMMA [67]

The refractive index profiles follow a Cauchy profile, which is typical of polymer materials. A high refractive index is a desirable trait. [60] SU-8 and OptiNDEX have the highest index in the red region of the spectrum of the contenders. The viscosity and spin properties must be able to meet the design goals of 150 μm thick layers. SU-8 is capable of being spun in thicknesses of up to 500 μm, although the others are not. For single coats, BCB is only capable of about 26 μm. OptiNDEX in particular is only available in low viscosity formulations for nominal thicknesses of a few microns. The sidewalls of the polymer should be smooth and vertical. Polyamide materials tend to have sharply re-entrant profiles, making them unsuitable for sidewall mirrors and electrodes. Absorption is also important because this determines the light throughput of the waveguides.

Generally, polymers are more absorptive at shorter wavelengths. The actual absorption depends on processing variables, which will be discussed in a subsequent section. For chemical tolerance, few polymers have the same resistance as SU-8. In fact, it is difficult to intentionally remove SU-8 material even when desired. These reasons make SU-8 the best option for this application.
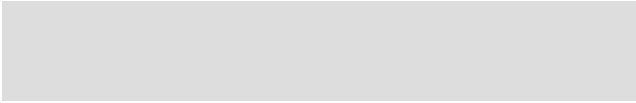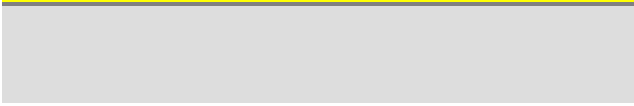
3.1.3 Electrodes

Two electrode materials were necessary, one for traces and the other for sidewall electrodes.   For sidewall electrodes, indium tin oxide (ITO) was used owing to its transparent and conductive properties. Later experiments proved that it does not react with the chitosan and DNA chemistry. For the conductive traces, gold was used for its high conductivity and, like ITO, chemical inertness.
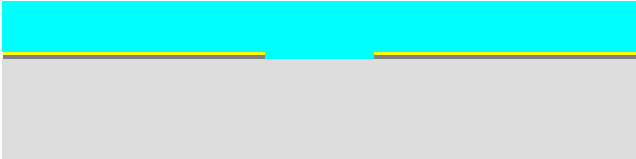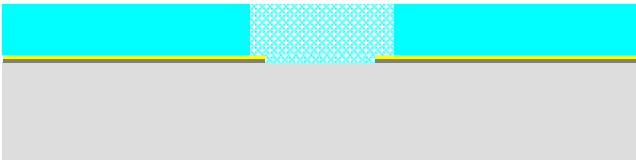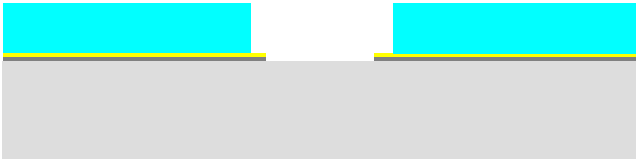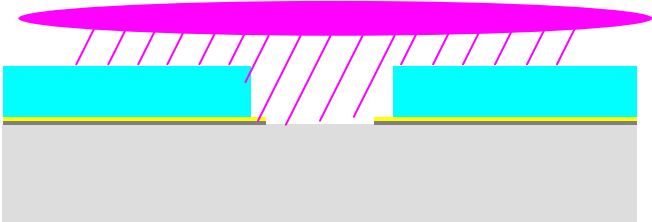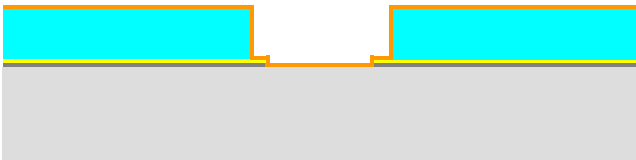
3.2 Fabrication Process Flow
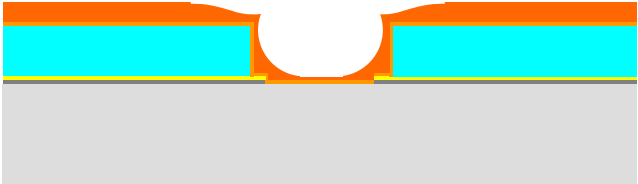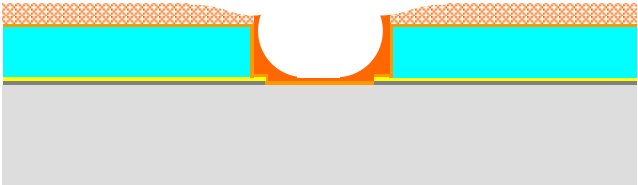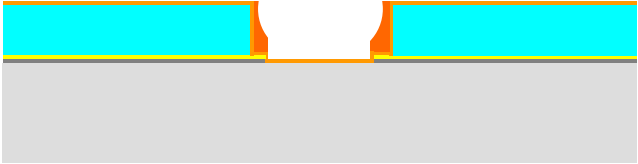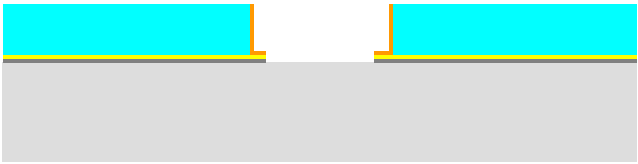
The fabrication process flow for the I-Cell device is given in Table 3.1. The design of the I-Cell and perspective views are detailed in Chapter 2. The processing for the C-Cell and Z-Cell is very similar, with gold substituted for ITO.

Table 3.1: Fabrication Process Flow
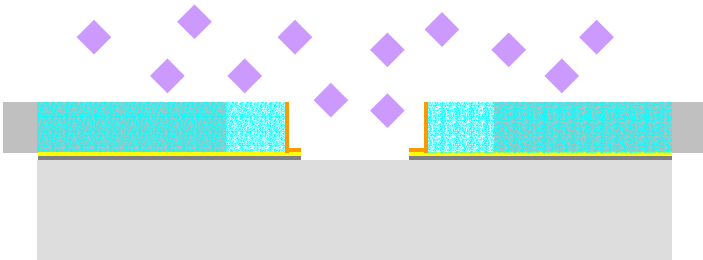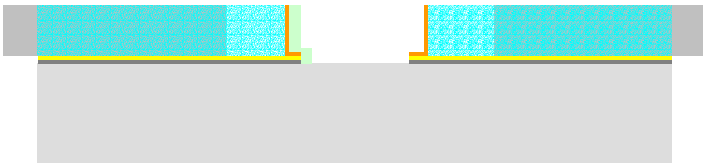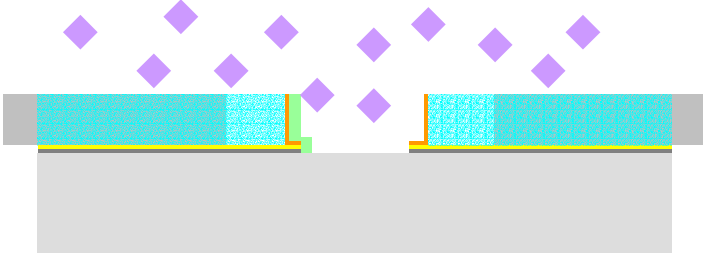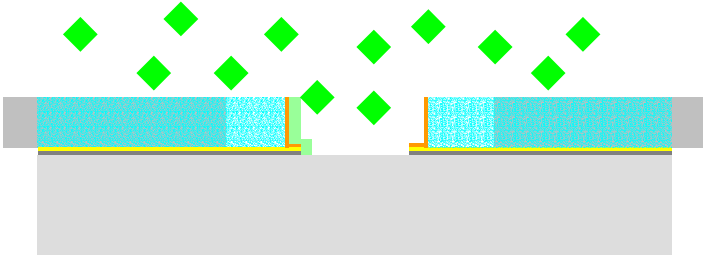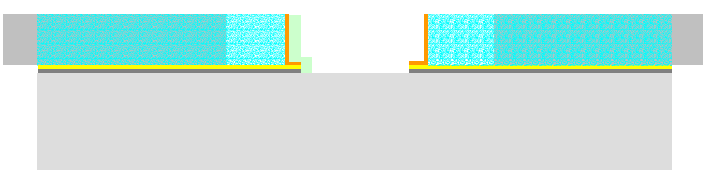
Step	*Wafer View*	*Details*
1		Start with Pyrex wafer, 500 μm thickness. Clean with Acetone-Methanol-IPA-DI sequence if not new out of box.

Step	Wafer View	Details
2		Electron beam evaporate 200Å Titanium, 2000 Å Gold. See Section 3.3.1
3		Spin Shipley 1813 with standard recipe for a nominal thickness of 1.5 μm. See Section 3.3.2.
4		Pattern with a contact aligner and the "Gold Trace #1" mask.
5		Etch Gold with Transene TFA Gold Etchant (Iodine Acid Complex) for 100 s at 23^oC. Etch Titanium in 50:1 BOE at 23^oC for 5 minutes.
6		Strip photoresist with Acetone-Methanol-IPA-DI rinse. Descum with 50W O_2 Plasma for 30s.

Step	Wafer View	Details
7		Spin AP300 according to modified recipe which deposits a very thin layer of TiO_2; Spin SU-8 with standard SU-8 recipe. Pre- bake at 95^oC for 100 minutes, 300°/hr ramp. See Section 3.3.3.
8		Expose SU-8 at 2250 mJ cm^{-2} (@ 405 nm) with "SU-8 Mask #2" Post bake at 95^oC for 100 minutes at 300° C hr^{-1} ramp.
9		Develop SU-8 in PGMEA for 25 minutes at 23^oC.
10		Ar$^+$ plasma clean wafer, 20 W, 5 minutes. Etch TiO_2 with BOE until surface is hydrophilic.
11		Sputter ITO, 100 W, 5 mTorr, 60 minutes, 110 mm substrate distance. See Section 3.3.4.

Step	Wafer View	Details
12		Spin AZ9245, ramp to 110°C, 500°C hr^{-1}, natural cool down. See Section 3.3.5.
13		Expose 4250 mJ cm^{-2} (measured at 405 nm) with "Sidewall Mask #3".
14		Develop in AZ 400K inorganic developer, 1 minute and check, up to 3 minutes if necessary
15		Etch ITO in 1:1 HCl : DI H$_2$O for 30 seconds.
16		Strip AZ9245 in Acetone, Methanol, IPA, DI H$_2$O

Step	Wafer View	Details
17		Dice into chips with wafer dicing equipment (Disco DAD 123)
18		Sanitize in 1N NaOH – 30 minutes. See Section 3.3.6.
19		Clean in Alconox critical cleaning soap
20		Attach and align fiber optics. See Section 3.3.7.
21		Clean in Alconox critical cleaning soap

Step	Wafer View	Details
22		Sanitize in 1N NaOH – 5 minutes. *Note:* This step can erode some of the UV epoxy. Care must be taken to ensure that the fibers do not detach.
23		Deposit Chitosan using probe tips – See Section 3.3.9.
24		Neutralize chitosan in 1N NaOH for 5 minutes, rinse in DI. See note in step 22.
25		Store in SSC Buffer Solution
26		DNA Functionalization. See Section 3.3.10.
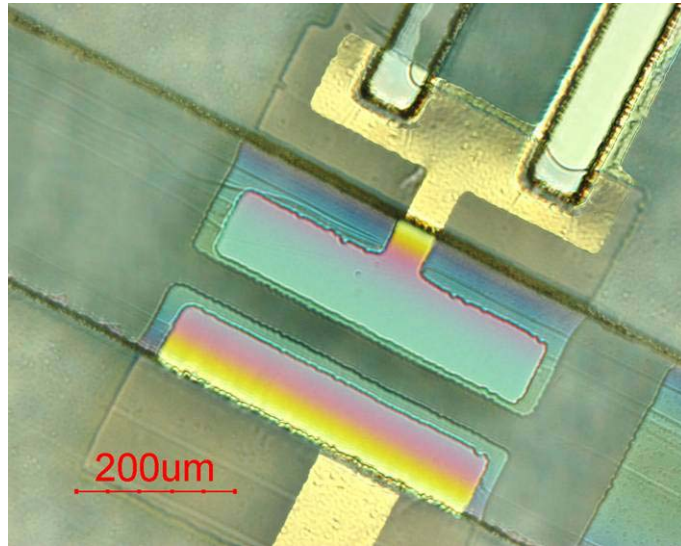
Figure 3.2: Optical micrograph of a fully-fabricated I-Cell device (Chip 11)

3.3 Process Development

3.3.1 Electron Beam Evaporation

The traces on the Pyrex substrate are formed in Gold with a Titanium adhesion layer. The deposition and patterning is a straightforward process. Titanium is evaporated on a clean Pyrex wafer, followed by Gold. The evaporator used for these devices is a CHA Mark 40 Electron Beam Evaporator with an Inficon quartz deposition controller. The wafers are put in a "chandelier" type planetary orbital fixture for deposition uniformity. The 45° tilt of the wafers as they rotate provides for good sidewall deposition which is important to the C-Cell and Z-Cell. The wafers on the fixture have an assumed 50% tooling factor for deposition versus those mounted directly on top of the crucible. [68]

Once the wafers are in the chamber, a cryopump maintains a base vacuum pressure of 2×10^{-6} torr. The deposition parameters used are given in Table 3.2.

Table 3.2: Electron Beam Deposition Parameters

Film	Base Pressure (torr)	Beam %	Rate (Å/sec)	Thickness (Å)
Ti	2×10^{-6}	72	4	200
Au	2×10^{-6}	76	7	2000

3.3.2 Gold Trace Patterning with Shipley 1813

The gold patterning procedure is typical. Shipley 1813 is a positive photoresist that can be spun to a nominal thickness of 1.5 μm. All of the gold trace features are greater than 10 μm in minimum dimension achievable with transparency masks (See Section 3.3.3.3), so processing on contact lithography equipment is easy. Table 3.3 gives the standard recipe for Shipley 1813 processing.

Table 3.3: Shipley 1813 recipe

Step	Purpose	Procedure
Spin Coat	Coat Resist	3000 RPM, 30s
Pre-Bake	Crosslink Resist	100°C, 60s
Exposure	Define Pattern	200 mJ cm^{-2} @ 405 nm
Develop	Remove Exposure	Microposit 352, 2 minutes @ 23°C
Strip	Remove all PR	Acetone-Methanol-IPA or Aleg 310

After the patterning of photoresist, the metal is etched in the recipe given in Table 3.4.

Table 3.4: Trace etch recipe

Step	Procedure
Etch Au	Etch in Transene TFA Gold Etch, 100s at 23°C
Rinse	Rinse in DI
Etch Ti	Etch in 50:1 BOE, 5 minutes, 23°C
Rinse	Rinse in DI

3.3.3 SU-8

SU-8 is a negative-tone, photodefinable, chemically-amplified epoxy resin. IBM developed the photoresist formulation from the epoxy created by Shell Chemical. The name SU-8 is derived from the 8 epoxy groups present in the monomer structure. The epoxy groups cross-link to one another to form a polymer. Thus, the crosslink density is influenced by the number of functional crosslinking groups. Eight groups makes for a very dense polymer for SU-8, and the number of these groups influences the resolution, aspect ratio, profile, optical index, and absorption. SU-8 as sold by Microchem Corp consists of 4 components: the epoxy resin, the resin solvent (Gamma Butyrolactone, GBL), the photoinitiator (Triarysulfonium / Hexafluoroantimonate Salt), and the photoinitiator solvent (Propylene Carbonate). After spinning on the substrate, the layer is pre-baked to evaporate the solvents. Upon i-line exposure, the photoinitiator absorbs photons and produces a strong catalytic acid, $HSbF_6$. The post-baking step provides the activation energy for the catalytic acid to cross-link the epoxy groups. As a catalyst, $HSbF_6$ is not consumed in the process and will continue to cross-link while the film remains at an elevated temperature. It is possible, by diffusion of the catalyst, to cross link non-exposed areas which can be problematic for high resolution structures. The

development agent used in the commercial SU-8 is PGMEA (Propylene Glycol Monomethyl Ether Acetate). The low-molecular weight polymer in the unexposed areas is highly soluble in PGMEA, while the high-molecular weight matrix in the exposed areas is not.

3.3.3.1 Developed Recipe

SU-8 is capable of high aspect ratios [69] in thick films, and has good sidewall profiles. Initially, the SU-8 fabrication process was developed at the MEMS Sensors and Actuators Lab (MSAL) for the purpose of microfluidic channel definition, gas separation nozzles, and molds for embossing of other polymers such as PDMS. [70]   Other groups have used SU-8 to define optical structures integrated with microfluidic components. [71, 72]   Table 3.5 is the recipe developed during the course of this thesis. One of the chief additions was the AP300 adhesion promotion step. The dosage was tuned for improved optical performance. The following sections describe some of the process development aspects and challenges.

Table 3.5: SU-8 and AP300 recipe

Step	Purpose	Parameters
Spin AP300	TiO$_2$ monolayer adhesion promoter	5000 RPM, 60s
Bake AP300	Prevents Residues	150 ^{o}C, 15m
Spin SU-8	Spins for 130 μm layer	240 RPM 3s, 500 RPM 7s, 1200 RPM 20s
Pre-Bake SU-8	Evaporates GBL solvent	95° C 100m, 300 ^{o}C/hr ramp
Expose	Activates photoinitiatior	2250 mJ cm^{-2} @ 405 nm
Post-Bake	Cross-links resist	95 ^{o}C 30m, 300 ^{o}C/hr ramp
Develop	Dissolves low weight chains	PGMEA, 25m, 23°C
Rinse	Removes residues	Isopropyl Alcohol
Etch TiO$_2$	Removes insulating adhesion layer in unwanted areas	50:1 BOE, 10 minutes, 23°C

3.3.3.2 Stress Cracking

Unfortunately, SU-8 is typically a highly stressed film after deposition and is prone to cracking. Figure 3.3 demonstrates some of the difficulties encountered while working with SU-8. This stems from the fact that the CTE of SU-8 is 55 ppm/K versus 3.3 ppm/K for Pyrex glass and 3 ppm/K for Silicon. [73] All thermal change causes stress in the film, and abrupt changes can lead to cracking. Care was taken in processing to avoid rapid temperature changes such as the 300 ^{o}C/hr ramp for the pre- and post-bake steps. One strategy for avoiding cracking could be making the film more elastically compliant so it has lower stress when strained. The second is to increase the yield strength of the material so it does not break at the thermal stress levels. The latter direction was taken. To increase the strength of the layer, the exposure dosage was increased. It was found by

a successive "progressive exposure" process that at some dose the cracking disappeared. Finding this point involved spinning a uniform layer of SU-8 on a wafer and moving an opaque object over the exposing wafer at regular intervals to create regions of increasing exposure dose. The optimal does is the lowest dose where cracking is not present because higher doses result in less transparent films.
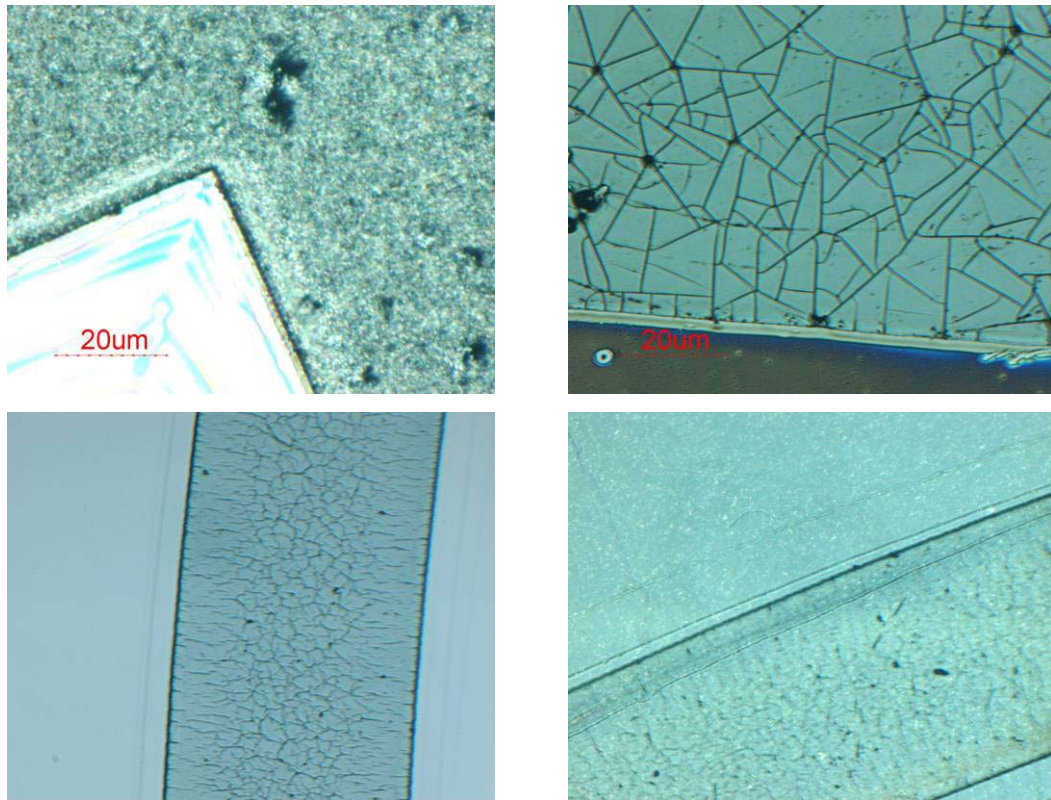
Figure 3.3: Early work with existing SU-8 recipes produced structures that were pitted and cracked.

Ultimately, the results depicted in Figure 3.4 revealed that the proper dose for a crack-free film was 2250 mJ cm^{-2} measured at 405 nm.
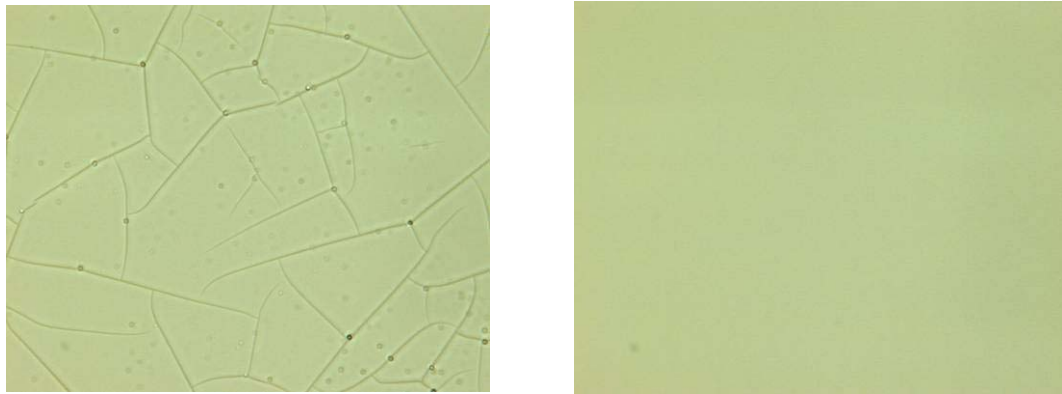
Figure 3.4: (a) A cracked SU-8 Layer. (b) A clear SU-8 layer on the same wafer with dose adjustment.

3.3.3.3 Sidewall Profiles of SU-8

To make in-plane optical components, near vertical sidewalls are necessary. Negative resists commonly demonstrate a re-entrant (inwardly-sloping) profile since the light which promotes crosslinking is more intense at the surface before it has been absorbed with penetration into the resist. With thick negative resist, T-Topping effects are usually apparent in structures with a re-entrant profile that is especially pronounced at the very top edge of the resist. It turns out that SU-8 is highly absorptive at short wavelengths, and sometime low-pass optical filters are employed in the exposure system to attenuate the shorter wavelengths that can promote t-topping. Having highly re-entrant profiles can reflect beams into the substrate which would result in signal attenuation, especially the C-Cell and Z-Cell since the sidewall mirrors must be vertical for best operation. A re-entrant profile also makes the sidewall resist patterning more difficult, if not impossible. An examination of the sidewall profiles with a SEM revealed that the recipe developed

for the purposes of this thesis produces structures with near vertical angles, greater than 87°. This is a benefit of choosing SU-8 over other photoresists that tend to have less favorable sidewall properties. Experimentation demonstrated that the UV dosage did not strongly affect on the sidewall angle, even when varied as much as 4x. Figure 3.5 shows the typical SEM images that determined the sidewall profile characteristics.
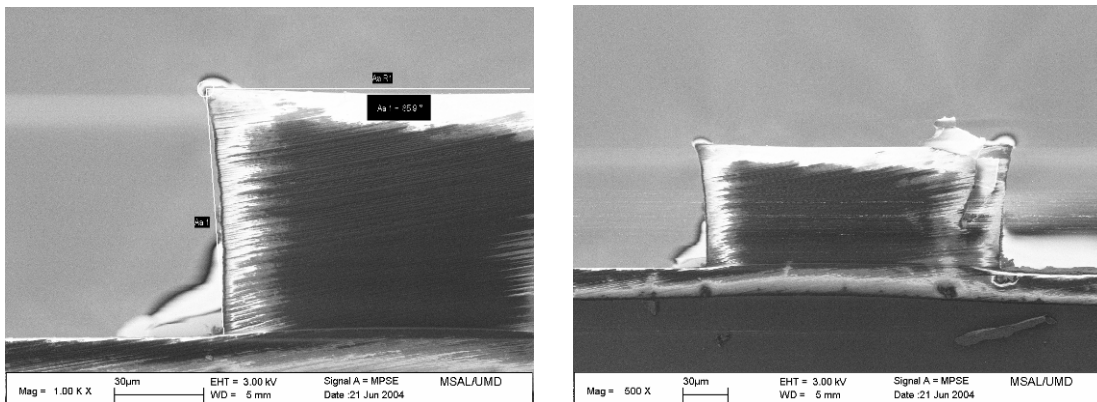
Figure 3.5: Sidewall profiles of an SU-8 waveguide. The sidewall angle is greater than 88°.

Sidewall roughness is an issue that is related to the sidewall profile. The roughness on the top and bottom of the waveguides is very low; however the sidewall roughness can be much greater and is strongly influenced by the lithography equipment and techniques. The greatest acceptable surface roughness for many systems is on the order of a tenth of a wavelength. More demanding applications require roughness of a twentieth of a wavelength. Surface roughness can be the result of the polymer's properties and development process, or as a result of the mask method and lithography equipment. In this case, the transparency mask method of lithography was by far the most dominant source. A transparency mask is created by a high resolution laser printer with greater than 5000 dpi. Generally, transparency mask techniques are suitable for feature sizes

greater than 15 μm, depending on the printer used to create the mask. Although high resolution in printer terms, this is not comparable to the nanometer spot sizes of electron beam mask writing equipment for standard microelectronic chrome masks. The chief advantage to using transparency masks is the quick turn-around time and low cost. A transparency mask based routine can go from design to fabrication in a day at a price of $50, while a traditional chrome mask will cost more than $500 depending on complexity with a turn-around of several weeks. The turn-around time advantages of transparency masks can make a big difference in iterative design processes. This comes at the price of high surface roughness on the edges of the fabricated structures. Figure 3.6a shows SEM micrographs of the edge of SU-8 structures fabricated with e-beam chrome masks and Figure 3.6b demonstrates those made with transparency masks.
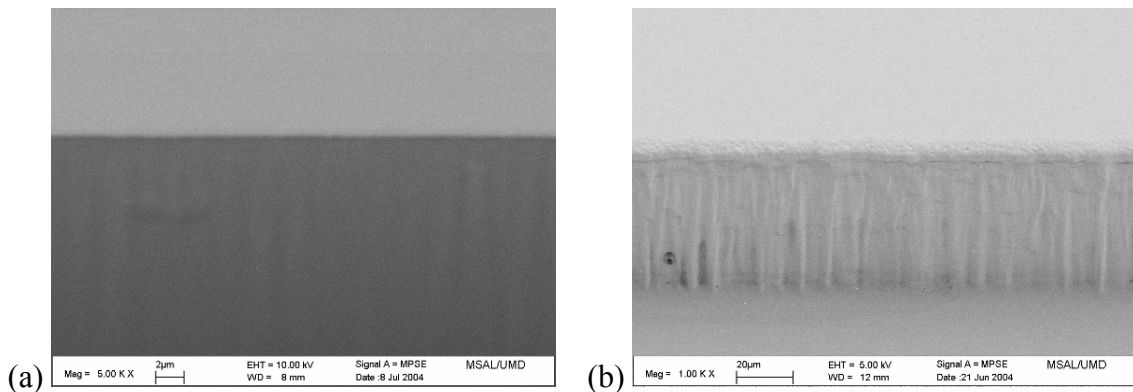
Figure 3.6: (a) SEM images of the sidewall of a SU-8 ridge. (b) The left image is a ridge formed with a chrome mask while the right is formed with a transparency mask from RGM Graphics in Bethesda, MD.

3.3.3.4 Substrate Adhesion

Although SU-8 has considerable advantages in the way of chemical resistance, the adhesion to the substrate can be a problem. The adhesion of SU-8 to silicon substrates has been observed to be very strong, however the adhesion to Pyrex was shown to be very weak. The "tape test" approach was used to make a reproducible and qualitative measure of adhesion. In this test, a piece of scotch tape is stuck to the structures on the wafer, and then removed. If the structures remain attached the adhesion is "good" while if they delaminate the adhesion is said to be "bad". The forces imparted in this test are far greater than any of those that may be encountered in normal handling of the device. Without any surface treatment, the adhesion of SU-8 to Pyrex was so weak that the devices would delaminate during normal handling and even during processing. As stated previously, the thermal coefficient of expansion mismatch between Pyrex and SU-8 causes stress that promotes the delamination. Large thermal stress, which occurs during rapid temperature changes, was observed to be one of the chief sources of delamination. Delamination also occurred during agitation in the development process. Several things were tried to remedy this problem. First, the exposure dose and processing parameters were changed to examine what would improve the adhesion. [74] Although some improvements can be made by adjusting the parameters, the results of these tests were not conclusive as no combination of processing parameters would produce acceptable adhesion. Modifying the process flow slightly to first spin a very thin layer of SU-8 as a blanket coating on the entire wafer was tried. This put thick SU-8 structures on top of that and was shown to be a good way to eliminate delamination.   Unfortunately the cost of this process is waveguide leakage through the blanket layer. Lastly, the use of several

adhesion promoters was tested including HMDS, AP3000, and AP300. Among these

AP300 produced excellent results, however it had some unwanted side effects that will be

discussed in the next section.

3.3.3.5   AP300 as an Adhesion Promoter for SU-8

Silicon Resources, Inc. of Cupertino California produces AP300, an organofunctionalized

titinate in IPA, which is purported to be effective as an adhesion promoter for Pyrex and

SU-8. The purpose of AP300 is to deposit a monolayer of TiO_2 to increase the adhesion

of cured SU-8 to the substrate. The recipe issued by the company involved spinning the

adhesion promoter on a clean Pyrex wafer at 3000 RPM for 30 seconds, and applying

SU-8 to the treated surface within 1 minute with no pre-baking. Discussions with

application engineers at Silicon Resources confirmed that this was the correct procedure.

[75] Unfortunately, although AP300 was shown to dramatically increase the adhesion, it

left behind a thin film of residues on the entire wafer. These residues can be observed in

a, b, and c of Figure 3.7. Not only is it possible for some leakage of light to propagate in

the thin residue, but also the residues also inhibit electrical contact to the bottom of the

channel.
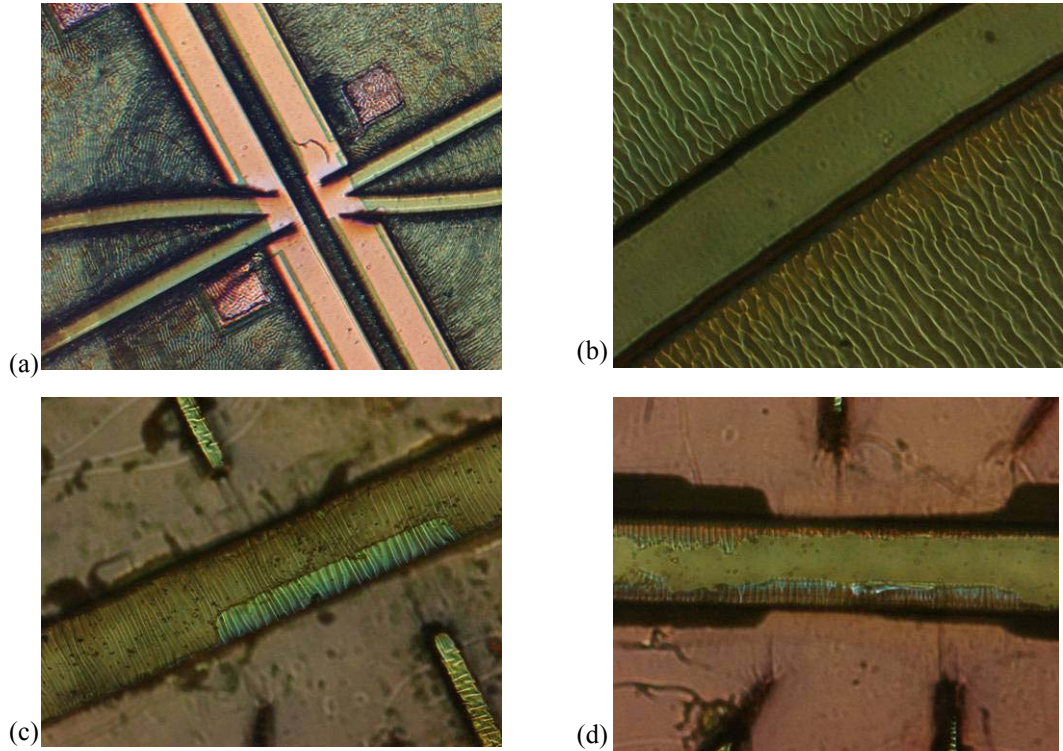
Figure 3.7: Images of devices demonstrating the residues resulting from the use of AP300 according to the manufacture's recipe and instructions. The wavy "coral-like" formations are residual SU-8.

After many trial runs and inquiries with Microchem and Silicon Resources, there was no improvement in the residue formation. Several process modifications were tried initially, including more thorough pre-cleaning of the wafers, longer development times, and development at higher temperatures (50° C). None of these modifications improved the situation. Several possibilities were considered:

1. Wash the wafer in SU-8's native solvent (GBL) following development

2. O_2 plasma clean wafers following development

3. Lift-off procedure of the adhesion promoter

4. Pre-bake the adhesion promoter to evaporate volatile components

The idea behind the GBL rinse was that the residues were not strongly cross-linked and would be susceptible to GBL. Through many trials which involved immersing the wafer in GBL at 70°C for 2 hours and overnight at room temperature, there was no dissolution of the residues whatsoever. A similar method of thinking was behind the O_2 plasma clean routine. In general, plasma etching of SU-8 involves SF_6 and O_2. Most organics are eroded by O_2 alone. Again, it was thought that that the residues would etch far faster in O_2 than the exposed and cross linked SU-8. This was shown not to be true, as the waveguides etched along with the residues. The results of the plasma process are shown in Figure 3.7d. Compared to Figure 3.7c, note that some of the residues have been cleared up in the channel, but the removal is far from complete and the waveguide surfaces are darkened due to etch roughening. The lift-off idea was to only put the adhesion promoter down in patches on the wafer so that the residues will only appear in the treated areas and not everywhere. In this case, not all of the electrical contacts would be blocked. While not a complete solution of the residue problem, this would prevent their presence in all undesirable locations. Along with this attempt, a pre-bake of the AP300 on the wafer prior to SU-8 spin was performed, with the idea that this could evaporate the organic components that were causing the residues while leaving behind the TiO_2 which is the actual adhesion surface. In practice, both the lift-off and the pre-bake attempts were successful. The lift-off procedure was successful in patterning the TiO_2 regions, however it has been shown that the pre-bake of the lift-off resist was actually responsible for clearing up the residues. Figure 3.8 shows the results of the two techniques.
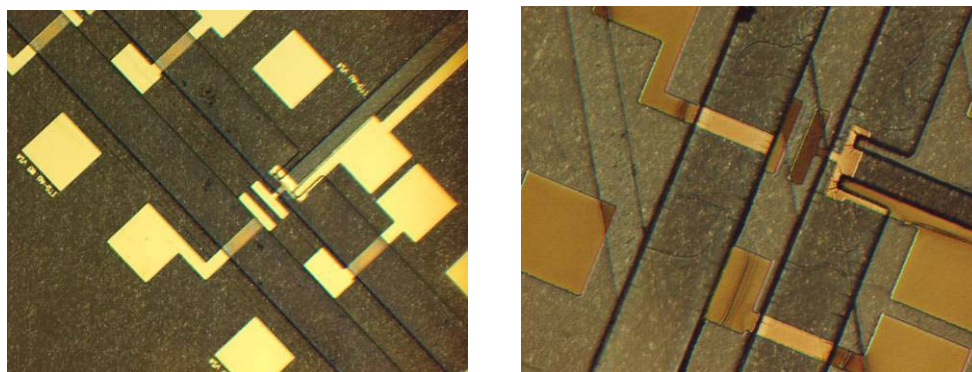
Figure 3.8: (a) Result from modified AP300 recipe showing no residues. (b) Lift-off AP300 recipe. The lines result from the AP300 coating.

From these results, the cause of the residues is conjectured to be the result of some components in the adhesion promoter initiating cross-linking of the epoxy groups in SU-8. SU-8 is a chemically amplified resist, where a photosensitizing agent releases acid free radicals upon exposure. When the activation energy for cross-linking is thermally supplied, the free radicals will crosslink the epoxy chains. It is reasonable to assume that acid components in the adhesion promoter were functioning as the acid free radicals or liberating acid free radicals in unexposed areas. The pre-bake step at 150°C eliminated (by either evaporation or decomposition) these components of AP300 and thus eliminated the residues.

3.3.3.6 Optical Transmission

One of the optical parameters that is strongly influenced by the processing is the optical transmission. Generally, polymers absorb at shorter wavelength regions corresponding to electronic excitations, and at wavelengths in the IR regions corresponding to molecular

excitations. This leaves a window in the long wavelength visible and short wavelength IR where polymers have comparably high transmission. The absorption of SU-8 was analyzed from a sample layer of delaminated film. The thin delaminated film was inserted into a Genesys 2 spectrophotometer and analyzed from 400 nm to 1100 nm. A graph of the relative transmittance as a function of wavelength is given in Figure 3.9. From this, it was found that the optical transmittance of SU-8 decreases with increased exposure. This is an expected result, since more exposure increases the crosslinking which increases the rate of absorption. The results of this test determined the optimal point for the SU-8 recipe developmentp; that the dosage should be increased to the point of acceptable structural properties, but not further to avoid unnecessary optical losses.

Transmittance vs. Dose Region
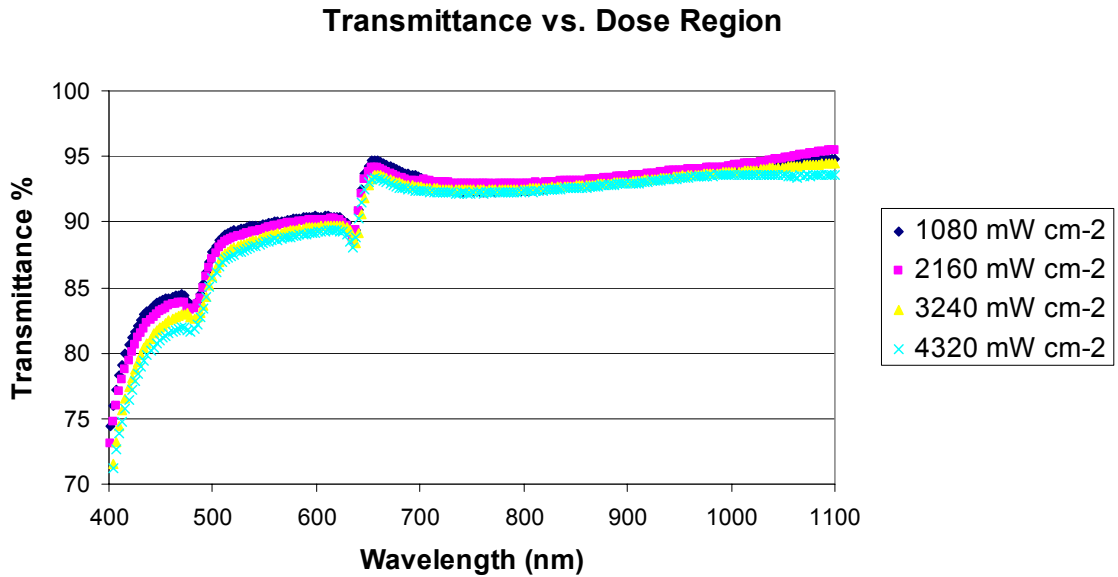
Figure 3.9: Graph of transmittance versus wavelength for SU-8 at various exposure energies.

3.3.3.7 Process Uniformity

One important question in the development of any microfabrication process is its uniformity. Typically uniformity relates to the thickness of the material. For SU-8, and thick polymer films in general, the thickness uniformity from the center to the edge is not very good. Throughout the fabrication process an overall thickness nonuniformity of 10% was observed from the center of the 100 mm wafer to the outer 75 mm radius. Beyond this, the "edge bead" effect occurs and thicknesses can increase by almost 90%. Fortunately, for this application thickness variations were not observed to be a significant problem. Some optical loss can occur in a waveguide that tapers down, however this loss is likely insignificant compared to the other losses in the system.

3.3.4 Indium Tin Oxide Deposition

Indium Tin Oxide (ITO) is a wide-bandgap high transparency semiconductor that is formed by substitutional doping the cubic bixbyte structure of indium oxide (In_2O_3) with Tin (Sn). The tin forms an interstitial bond with oxygen in the lattice. In fact, tin acts like an n-type donor (depending on the valence state) and, along with oxygen vacancies in the lattice, produces an n-type semiconductor. [76] According to Bashar, ITO can be effectively represented as $In_{2-x}Sn_xO_{3-2x}$. For visible transparency, a semiconductor must have a bandgap greater than about 3.75 eV, and such is the case for ITO. The bandgap can vary with deposition conditions, however. ITO thin films have been used extensively in Liquid Crystal Displays (LCDs), Charged Coupled Detector arrays (CCDs), heaters for automotive and aircraft windows, anti-static coatings, and optoelectronics applications in VCSELs and photodiodes, among others. ITO films behave as metals to radiation

exceeding its plasma wavelength of 1 um. The film reflects light at those longer

wavelengths, with reflection related to conduction. [77, 78]

Table 3.6: Reported Values of ITO Properties

Property	*Value*
Bandgap (E_g)	3.5 eV – 4.06 eV [76]
Refractive Index (n)	1.96 [76]
Lattice Parameter (a)	~10.2 Å [76]
Free-Carrier Concentration (N)	5×10^{20} cm^{-3} Typical [81]
Plasma Wavelength (λ_p)	>1000 nm [78] Typical, varies with N

A number of deposition methods are available and reported in the literature, including

evaporation, sputtering, and spray pyrolysis. Many times, in the case of evaporation and

sputtering, oxygen (0% - 3%) is added to the chamber to control the density of oxygen

vacancies which directly influences the conductivity and transparency of the film. [79]

This is not required, however, and some groups achieve good results without reactive

deposition processes. [80]

Photon absorption in semiconductors is the result of electron-hole pair creation for

wavelengths below the bandgap wavelength λ_{bg}, and free-carrier absorption elsewhere.

Thus, while conductivity and transparency can be obtained simultaneously in ITO there is

always a trade-off between the two properties. The sputter rate, substrate temperature,

source composition, and chamber oxygen all influence the free carrier density.

Additionally, oxygen donation from polymer materials can play a role to increase the

transparency and decrease the conductivity. This has been reported in the literature [81]

and observed experimentally in this work.

For this application, RF sputtering was chosen and the University of Maryland's AJA-100 RF Magnetron Sputterer in the Institute for Research in Electronics and Applied Physics (IREAP) was used. A variety of ITO targets are available with different ratios of Indium to Tin. For these experiments, a 95%-5% indium oxide-tin oxide target was used. Intially, DC sputtering was attempted as it has been shown in literature to produce less damage to organic substrates, like SU-8. [82] This was abandoned, however, due to some difficulties in striking the plasma.

Table 3.7: Deposition Parameters for ITO

Parameter	*Value*
Base Pressure	~7 x 10^{-8} torr
Operating Pressure	5 mTorr
Argon Flow Rate	20 sccm
Target Composition	95% In_2O_3, 5% SnO_2
Substrate Distance	110 mm
RF Power	100 W
Observed Sputtering Rate	4 nm / min
Substrate Clean	20 W, 5 minutes

A RF power of 100 W was seen to be suitable for deposition. Higher powers (150 W) caused a slight increase in transparency, with a significant drop in conductivity. Much higher powers were not used due to the damage they could impart on the SU-8 structures already patterned on the wafer. The deposition procedure for ITO followed the standard operating procedures for the equipment. A 5 minute substrate clean step was performed before each run at low power.

The deposited films exhibited good transparency, as evident in Figure 3.10. The transparency in the region of 633 nm, where the device has been selected to operate, is about 56%.
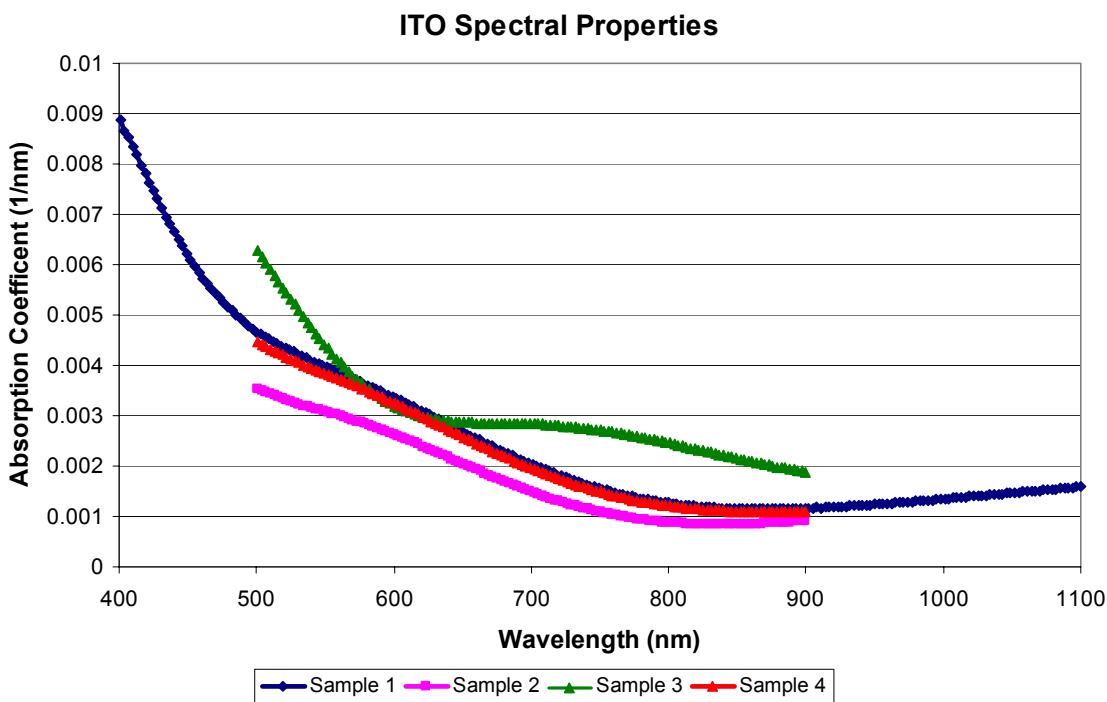
Figure 3.10: Typical Spectrophotometer (Genesys 2) measurements for an ITO film on a glass slide. Samples 1 and 4 were the typical deposition parameters of 100W, 5 mTorr, while sample 2 decreased pressure to 4.5 mTorr and sample 3 increased the power to 125 W.

The conductivity of ITO was measured at various deposition powers and pressures. Higher conductivity ITO benefits the device by reducing the voltage required for deposition of chitosan and decreasing the I^2R resistive losses during deposition. Although these are desirable aspects, they are less important than having high transmission through the system since that directly influences the detection capabilities of

the device. Table 3.8 shows the dependence of conductivity on deposition conditions.

Since the absorption properties of ITO for wavelengths less than the bandgap is affected

primarily by free electron absorption, the absorption coefficient can be related directly to

the film conductivity through the extinction coefficient k which comprises the imaginary

part of the refractive index. This relation is given in Equation 3.1. [59]

Equation 3.1

$$n = n_R - ik$$

$$k = \frac{\alpha\lambda}{4\pi}$$

Subsequently, k can be related to the conductivity of the material and the reflectivity.

Comparison of the sheet resistance as measured by the 4 point probe method and

calculated values from the spectrophotometry measurements were found to be relatively

consistent. Equation 3.2 relates k to the reflectivity R and conductivity σ. [59, 60]

Equation 3.2

$$R = \frac{(n_R - 1)^2 + k^2}{(n_R + 1)^2 + k^2}$$

$$2n_R k = \frac{\sigma}{\varepsilon_0 \omega}$$

Table 3.8: Conductivity versus power and pressure for RF magnetron sputtered ITO films on glass

Conditions	*Sheet Resistance*
100 W, 5 mTorr, 50 minutes	220 Ohms-Square
100 W, 4.5 mTorr, 50 minutes	199 Ohms-Square
125 W, 5 mTorr, 50 minutes	272 Ohms-Square

Etching ITO is a straightforward process. Various recipes for etching ITO include acid

chemistries such as HCl + (HNO$_3$ or FeCl$_3$) [78], and HF + H$_2$O$_2$ + H$_2$O [76]. For this

device, a 1:1 solution of HCl and H_2O was used for several reasons. [76]   The HCl and water chemistry avoids the hazards of working with HF, and the glass substrate is not attacked in that case. Furthermore, the SU-8 is not attacked by HCl, but can be by HNO_3. The etch was done at room temperature, about 23^oC, and had a rate of about 800 nm/min, so the total etch time for a sample was 30 seconds.

3.3.5 Thick Photoresist Sidewall Patterning (TPSP)

The design detailed in Section 2 calls for sidewall patterning on very thick structures. This type of microfabrication is highly unusual, but is necessary in this case to provide adequate surface area for the fluorescent medium. Patterning thick layers with spun-on resist is highly unorthodox, but this thesis presents a reliable and repeatable method for thickness up to 130 um.

3.3.5.1   Positive Resist and the Dill Model

For the thick resist application, positive resist was chosen. Positive resists are generally preferred to negative resists in microelectronic applications because they experience no "swell" in the development process and are generally easier to strip. A positive resist generally consists of three components when in liquid form: the solvent, the resin, and the photosensitive inhibitor. After spinning at a specific angular velocity for a specified time the solvent is evaporated in a pre-bake step that also cross-links the resist. The presence of the photosensitive inhibitor makes the pre-baked layer insoluble in a developer solution. Upon exposure to UV radiation, the inhibitor breaks down and no longer prevents dissolution in the developer. Thus, in a positive resist, the areas exposed to light

are dissolved while those which are masked by an opaque template are protected and do not dissolve in the developer.

The 1975 paper published by F. H. Dill established a standard way of characterizing positive resists. In this model, two first order partial differential equations characterize the resist parameters and are given in Equation 3.3. [83] The I(z, t) function is the intensity of light mW cm^{-2} into the resist (z) at time t. The M(z, t) is the concentration of solubility inhibitor at depth z into the resist at time t. Three parameters given in Table 3.9 can describe the time dynamics of the resist exposure.

Equation 3.3

$$\frac{\partial M(z,t)}{\partial t} = -I(z,t)M(z,t)C$$

$$\frac{\partial I(z,t)}{\partial z} = -I(z,t)\left[AM(z,t) + B\right]$$

$$R = R_0 \exp\left[E_2 M + E_3 M^2\right]$$

Table 3.9: Dill Parameters for AZ 9245 Positive Resist [84]

Parameter	Value for AZ9245		
	365 nm	405 nm	435 nm
A	0.4388 μm^{-1}	0.4245 μm^{-1}	0.0965 μm^{-1}
B	0.0219μm^{-1}	0.0212μm^{-1}	0.0220μm^{-1}
C	0.0222 cm^2 mJ^{-1}	0.0215 cm^2 mJ^{-1}	0.0175 cm^2 mJ^{-1}

The A parameter can be taken to be the absorbance of the photosensitizer as related to the fraction remaining, while the B parameter represents the non time-dependent absorbance of the resist film which is the "bleached" absorbance. The C parameter represents what could be considered as the "cross section" for absorption, which indicates how well the

light breaks down the photosensitizer. At time t=0, when the UV source is initially turned on, $M(z, t) = 1$ for all z and $I(0, t) = I_0$. As time progresses, $M(z, t)$ decreases with absorbed photons, and $I(z, t)$ increases at a fixed z until $M(z, t) = 0$ when it levels off at the bleached value. A solution to these PDEs can be complex and requires numerical methods. It is important, however, to consider qualitative aspects of the equations. The bleaching effect occurs because the photosensitizer is no longer absorptive as the light breaks it down. This means that it is easier to expose thick layers when the bleached absorbance (B) is very low because the UV light can penetrate deeper into the surface. At the B values for AZ9245 the bleached absorbance only blocks about 6% of the UV exposure from reaching the thickest areas of resist.

The concept of resist contrast is important when considering how well the exposed resist dissolves in the developer and how well the unexposed resist survives development. In the ideal case of infinite contrast, the resist becomes completely soluble when the exposure dose exceeds some energy density, and completely insoluble for dose energy densities below some value. In this case the development rate R, is a step function of $M(z, t)$, where some critical dose causes the resist to transition from completely insoluble to completely soluble. In practice this is not true, and the development rate is a sloped function of $M(z, t)$ which is nonzero for every $M(z, t)$. The nonzero development rate across the wafer area means that even unexposed areas are thinned in the developer. This has important implications for this thick photoresist process. In an ordinary microelectronic lithography process, the resist thickness is highly uniform on the surface of the wafer. Thus, if the unexposed areas which are uniform in thickness are eroded at a

rate that is substantially lower than the exposed areas the process with achieve the desired patterning. For this thick photoresist process, however, the thickness of the resist is highly nonuniform. Some areas are very thin while others are very thick. If the etch rate of the unexposed areas is high enough with respect to the etch rate in exposed areas, some of the thin unexposed areas may etch away before some of the thick exposed areas etch away. This is a problem of finite selectivity and, of course, is highly undesirable.

Another complication arises in what can be called mask contrast. In most ordinary microelectronic lithography processes, the mask is made of chrome evaporated on soda lime glass or quartz. In this case, the transmission through the quartz regions can be considered to be 100%, and the transmission through the chrome coated quartz regions can be considered to be 0% for an infinite contrast. For small features, diffraction makes the contrast finite, but this does not apply to the large features in this design. The finite contrast in this design is the result of the use of transparency masks, as described earlier. The transmission through the toner regions of the mask is nonzero, so the contrast is finite. This, in combination with the finite resist contrast, exacerbates the finite selectivity problem by augmenting the etch rate of the unexposed areas.

3.3.5.2 Recipe Development

Because photoresist has some surface tension, one could imagine the feasibility of coating the sidewalls of relatively thick structures if one was willing to sacrifice resolution and tolerate nonuniformities of resist thickness. This is a highly unorthodox procedure and made difficult due to the nonuniformities and the issues discussed in the previous section. With high resolution lithography, raised surface can produce "comets"

in the profile of the resist which are radial streaks that are reminiscent of the tail of a comet or the wake of a boat. The question was twofold: would the resist coat the sidewalls adequately, and, could the correct processing parameters be found such that the finite selectivity problem in the previous section could be overcome.

For the resist, AZ9245 was selected. It is a widely available resist from AZ Electronic Materials, and one of the few available in a high viscosity formulation which is required for this application. The nominal spin thickness for the recipe is 10 μm. This was considered to be the ideal nominal thickness, because viscosity that is too high could make the resist in the channel too thick.

Figure 3.11 shows an optical micrograph and SEM image of the first attempt to spin resist over the thick (130 μm) structures. In this case a "ridge" structure was spun, and patterned with intersecting lines. The first thing to note would be the nearly complete coating of the sidewall by the resist as the result of its surface tension. The base of the ridge still has photoresist, as shown in the close-up of Figure 3.12. The main challenge of this process is the sufficient exposure of the thick regions- which are 130 μm thick, while not overexposing the thin regions. The thickness uniformity issues discussed in Section 3.3.3.1 are very apparent here. Although the coverage is good, the edges of the ridge where the resist is the most thin have been etched away despite not being exposed to UV light. This is not a critical problem, but it does mean that the probability of making good electrical contact to traces that go over the ridges may be severely limited.
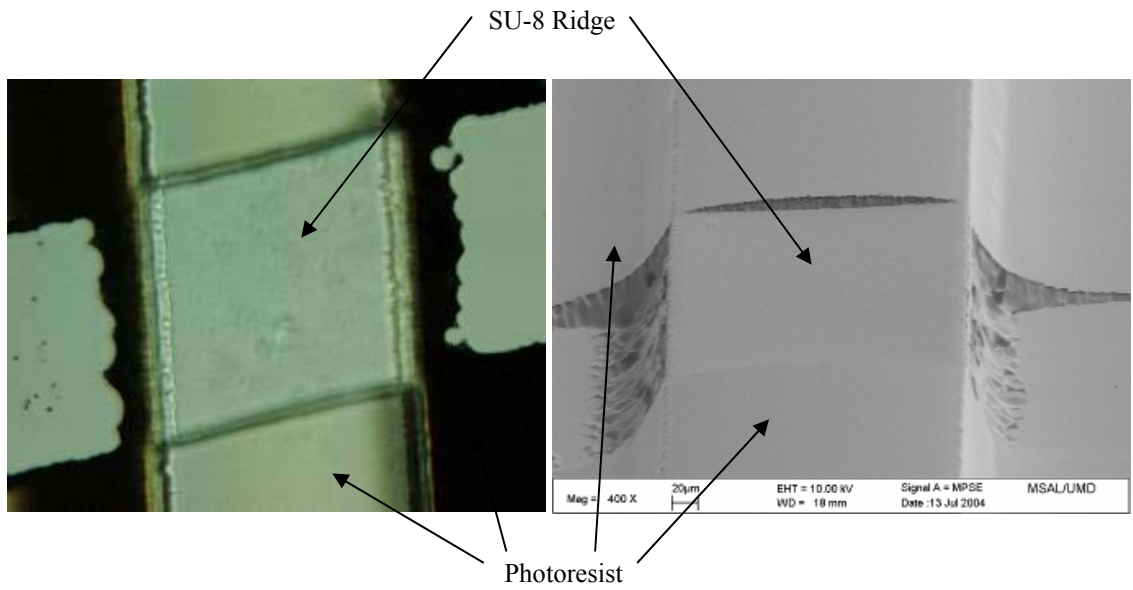
SU-8 Ridge

Photoresist

Figure 3.11: Preliminary results for the thick resist process. The exposure was deemed to be insufficient, however the spin coating coverage on the sidewall is complete.
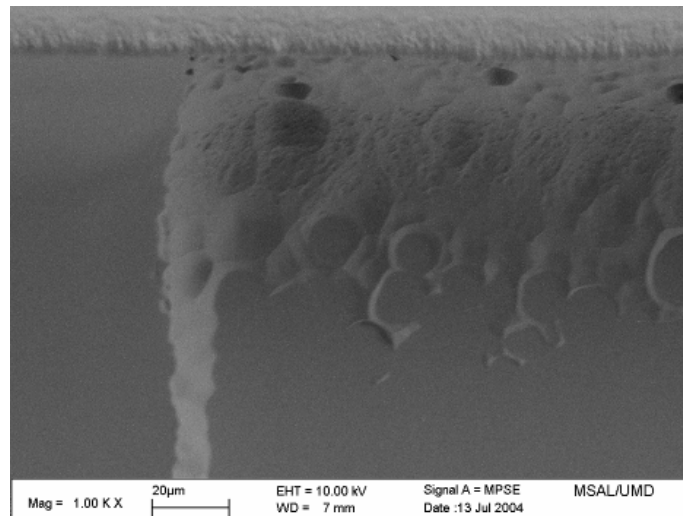

Figure 3.12: "Tranquility base here" – An underdeveloped and underexposed resist in the thick sections is reminiscent of a lunar landscape.

The second round of tests involved spinning the resist on structures that simulated microfluidic channels. This is different from the "ridge" spin attempted previously because the closely spaced channel walls cause thicker layers of resist over larger areas. The pre-bake time was modified to accommodate the thicker resist and a ramp was added. Without the ramp, the thick areas would erode too quickly because of the increased solvent content. The same pattern of intersecting lines was used in this case. Just as with the ridge structures, the sidewall coverage was observed to be complete in most cases, with the frequent exception of the edge. Since the channel structures are like ridges spaced close to one another, the actual profile in the channel appears to be an overlap of the profiles of ridges. SEM micrographs of this situation are shown in Figure 3.13. The reason why the developed pattern in the channel bulges out to become pill-shaped instead of maintaining a perpendicular profile is unknown, but could be the subject of further study. It can be seen that the actual processing parameters were very good, since the removal of photoresist is complete at the bottom of the channel where the resist is of maximum thickness. Although being able to pattern lines over channels was an encouraging result, it is not exactly the same situation which is needed in the fabrication of the actual device. In this situation, the pattern eroded the resist in a continuous line through the channel and left the sidewall uncovered. In the actual design, the sidewall is to stay protected while the channel bottom is selectively etched.
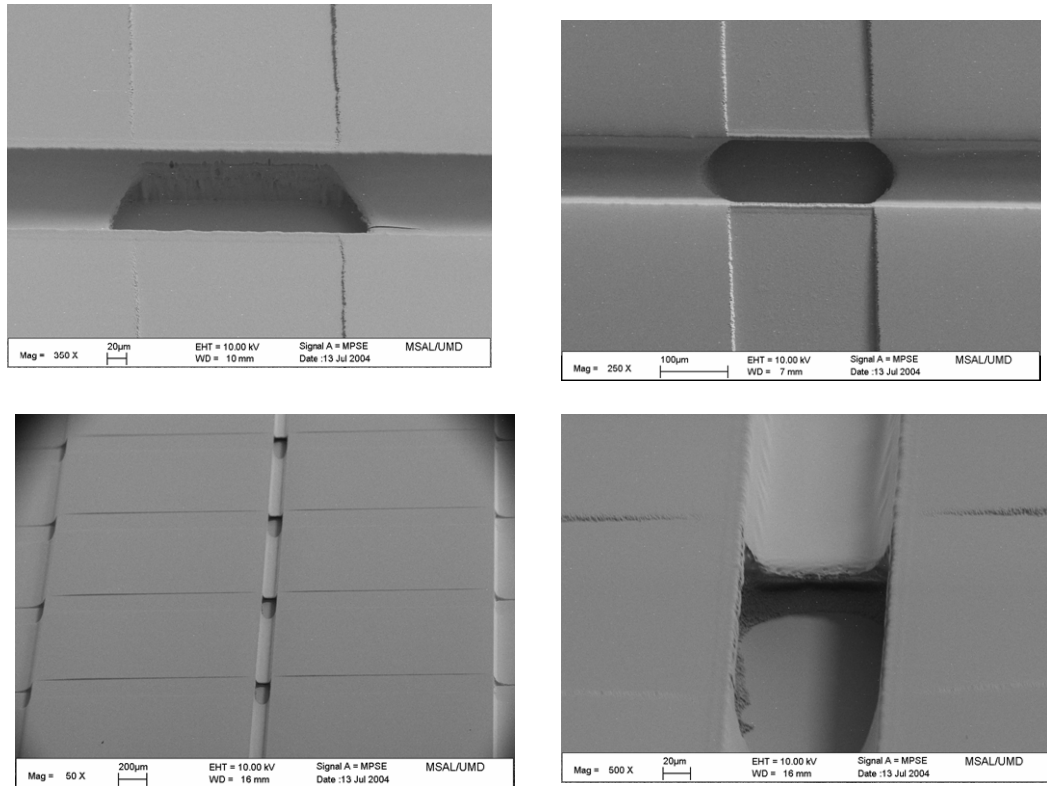
Figure 3.13: Profiles of initial work on the thick sidewall photoresist process.

To bring the technique more toward what is needed in the device, and determine the maximum or minimum channel widths, some test structures were developed. The structures, depicted in Figure 3.14, replicate something like the C-Cell, which is probably the most challenging design to fabricate. The width of the channel varies to test what limiting values are imposed on the channel width. As it turns out, good results are only produced for channel widths exceeding 150 μm. This required modification of the original design which called for channel widths of 100 μm.
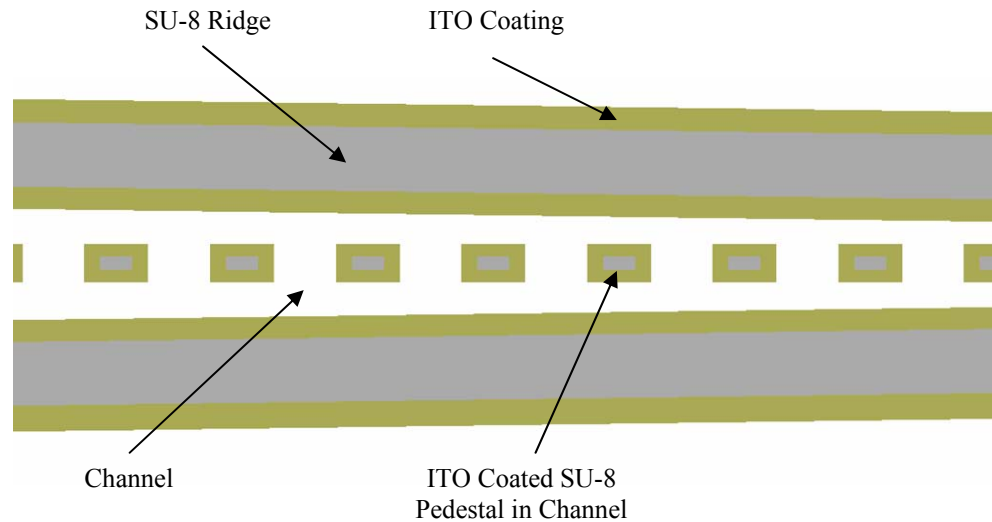
Figure 3.14: Channel spacing test structures. The tapered channel determines the minimum allowable channel width. The smallest allowable channel spacing along the taper indicates the fabrication resolution limit. The pedestal structures simulate the C-Cell.

After the refinement of the previous rounds, the channel width was expanded and the bake and exposure parameters tuned further. Figure 3.16 shows the results of the recipe when fabricating the Z-Cell. The minimum width between ridges was expanded to 200 μm from the original design. It is important to note that good patterning was achieved—simultaneously – on the sidewall of the SU-8, on top of the SU-8, and on the substrate. The bottom of the channel is very clean and free from residues. The profile of the photoresist was measured using a depth-of focus technique with a microscope under high magnification. These results are given in Figure 3.15.

Average Photoresist Profile

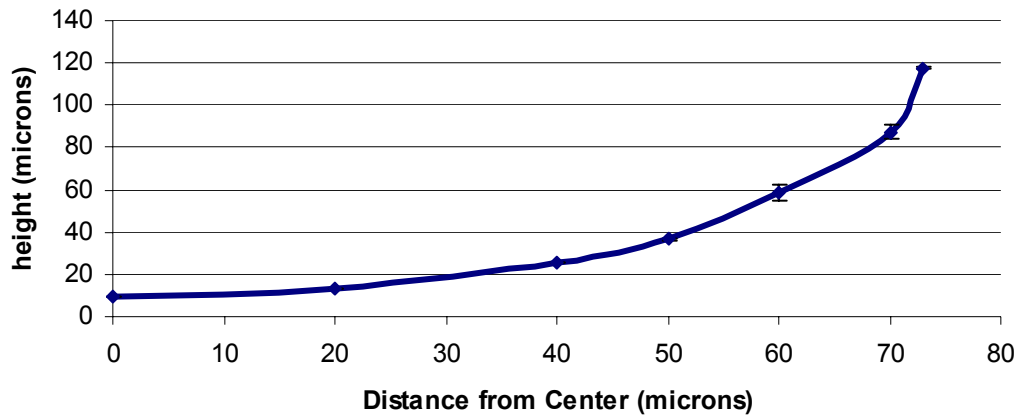**Figure 3.15: The average photoresist profile in a 150 micron width fluid channel. Distance is taken from the center of the channel. The profiles were measured using depth-of-focus techniques.**
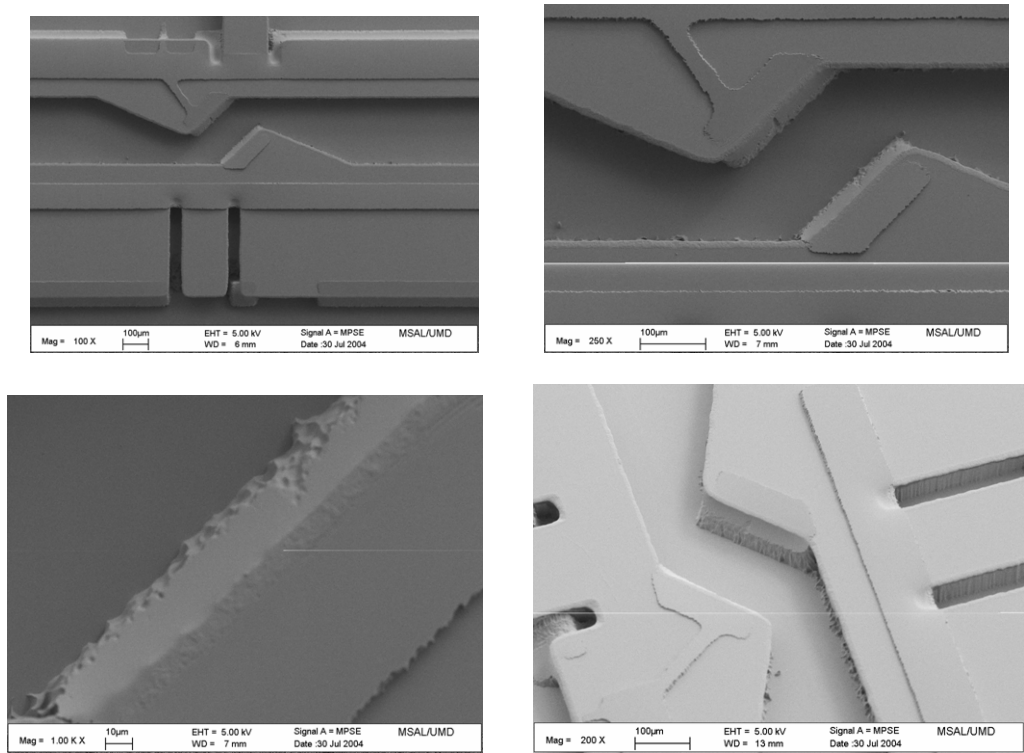
Figure 3.16: Progress in recipe development showing various views of the Z-Cell with photoresist on the sidewall.

The problem of transparency mask contrast was improved by the use of chrome mask transfer. In this procedure, the transparency mask is used to expose a chrome mask blank that has been sensitized with photoresist. The result is a mask that has the same features and resolution as the transparency but has improved contrast. This led to the improvement in edge coverage as depicted in Figure 3.17. Although the edge coverage was improved by the increased contrast, it did not have 100% yield.
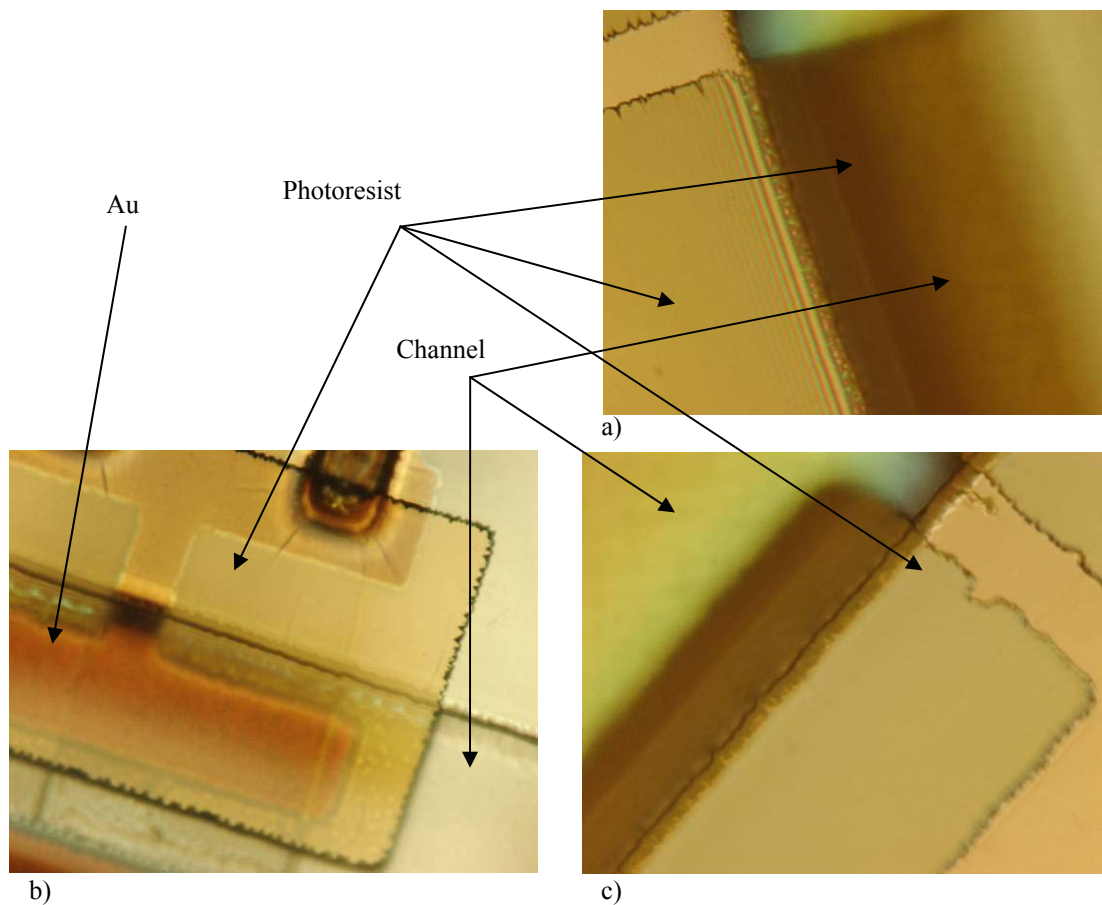
Figure 3.17: Contrast enhancement due to the transparency - chrome mask transfer. (a) Edge formed with transparency mask lithography demonstrates fringes and thinning of resist at the edge. (b, c) Same structure using the chrome transfer lithography process demonstrates complete edge coverage.

Finally, with all the processing details worked out, it was time to test the full procedure by carrying out the etching of ITO on a functional sample. Upon confirmation of a successful lithography procedure, the ITO was wet etched in a solution of HCl and H_2O. An SEM micrograph of the sidewall patterning of ITO is shown in Figure 3.18. Although a thin film of gold was sputtered to prevent charge-up, the ITO coated regions appear lighter due to the difference in secondary electron yield versus the SU-8.
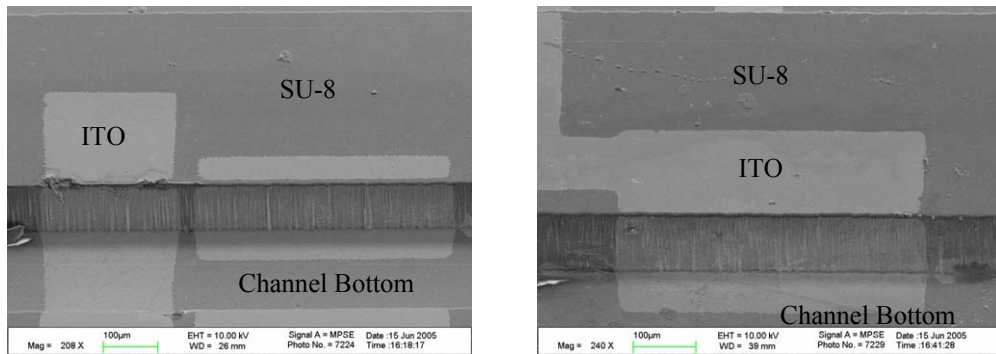
Figure 3.18: SEM Images of sidewall patterned ITO.

Guided by theory and with an iterative empirical process, the thick sidewall recipe was developed. This process could be useful in creating other structures that require in-plane reflective optics or electrostatic actuation.

Table 3.10: Processing parameters for the AZ9245 thick sidewall resist process

Step	*Purpose*	*Parameters*
Spin	Coats Resist	Apply to full area of wafer, 350 RPM 5s, 1000 RPM 40s.
Pre-Bake	Evaporates solvent and cross-links resist	500°C/hr ramp to 110°C, hold for 2 minutes, natural cool down
Exposure	Activates Photosensitive Agent	4250 mJ cm^{-2} at 405 nm
Development	Dissolves Exposed Regions	AZ 400K, diluted 1:3. 1 minute and check, up to 3 minutes may be

		required.
Etch	Depends on application	
Strip	Dissolves all resist	Acetone-Methanol-IPA or Aleg 300

3.3.6 Cleaning and Sterilization

The cleaning and sanitization steps for this device include two components: Alconox critical cleaning detergent, and Sodium Hydroxide sterilization agent. Alconox is a commercially available detergent that breaks up oils and other surface contaminants. Even after this step, sterilization is necessary. For most laboratory and medical equipment, autoclaving is used for sterilization. This process involves steam at high pressures and 121°C. Due to the sensitive nature of SU-8 to temperature, it would not be suitable for this device. Instead, the devices are immersed in a 1N solution of NaOH for 15 minutes. This is a standard practice in biochemical and microbiology labs to remove biological contaminants that can interfere with the operation of the device.

3.3.7 Fiber Optic Coupling

The coupling of optical fibers to the integrated waveguides, while facilitated by the fiber clamp structures, is a delicate operation that takes some practice and patience.   The design of the fiber clamps is given in Chapter 2. The fibers are first prepared by stripping the jacket and cleaning with IPA. The ends are perpendicularly cleaved either by a cleaving tool or by hand with a diamond scribe. Next, the cleaved ends are dipped into the UV adhesive, Norland NOA-28. The fiber is then inserted into the clamp structure on the chip while being observed under a stereomicroscope. Once satisfactory alignment

has been confirmed, the region is flooded with UV light until the epoxy has hardened. Occasionally the use of a glass cover slip can keep the fiber from "floating" out of the clamp. In this case, the cover slip will be permanently attached to the chip following UV curing. Figure 3.19 shows SEM images demonstrating good optical coupling between the fiber and the integrated waveguides.
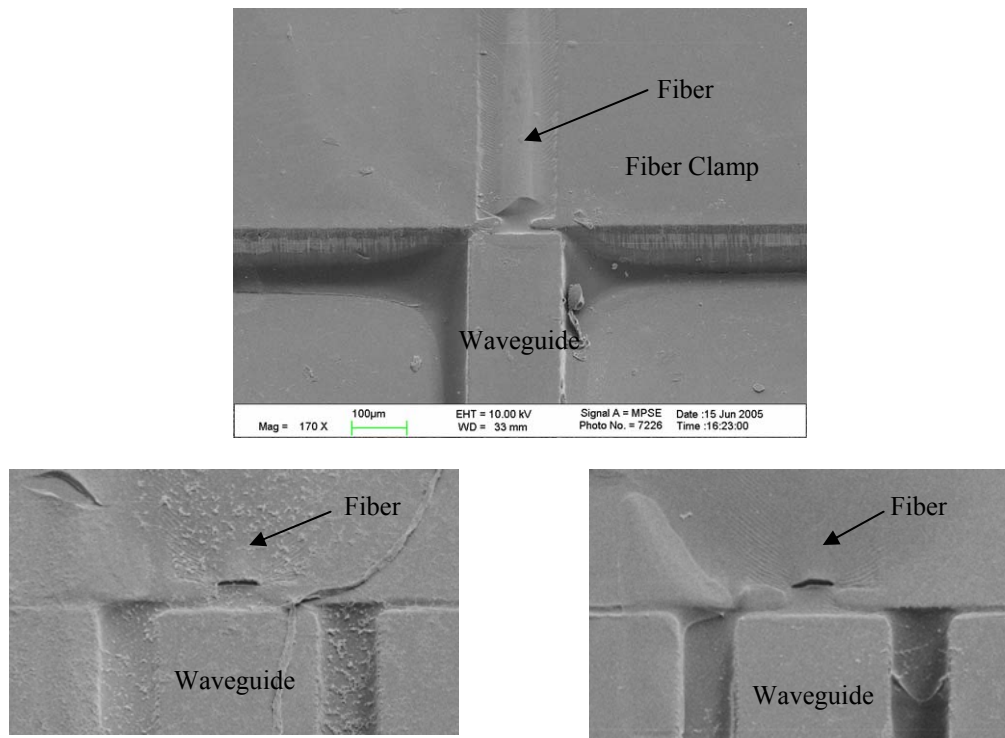

Figure 3.19: Optical fibers coupled to integrated waveguides. The fibers are secured with UV curable epoxy.

3.3.8 Z-Cell and C-Cell Fabrication

Micrographs of the Z-Cell and the C-Cell which were explained in Chapter 2 are given in Figure 3.20. The fabrication for these devices is the same as the I-Cell, with the exception that gold is used as the electrode layer instead of ITO.
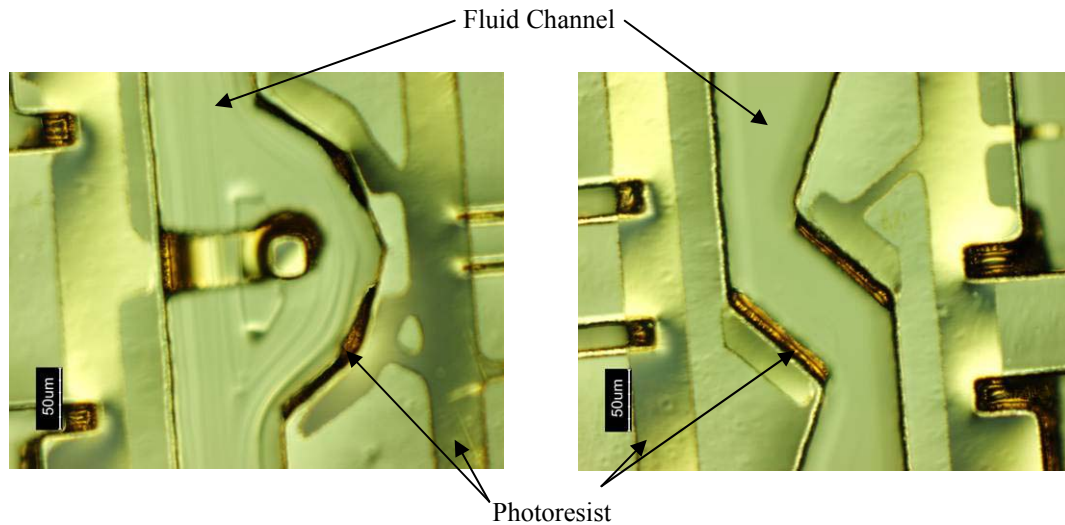
Figure 3.20: (a) C-Cell and (b) Z-Cell. Devices are shown with gold evaporated on entire surface and photoresist defining the areas in which the gold will be masked.

3.3.9 Chitosan Deposition

The deposition procedure for chitosan evolved over the course of this work. Since chitosan has electrodepositable properties, it is possible and often desirable to deposit the material in a sealed channel by the application of voltage on the electrodes while a chitosan solution was injected via pressure driven flow. This has been developed separately by Park et. al. with the intention that those methods can be integrated with the optics and fabrication procedure developed in this work. [85] Initially, a procedure very similar to that of Wu et. al. [40] was used. This involved submersing an entire wafer or chip into a beaker filled with the chitosan solution. Alligator clips provided electrical contact to on-chip electrodes, with an aluminum counter electrode. For later work in which centrifuge-tube style chips were used, a deposition procedure using

micropositioning probes was used as shown in Figure 3.21. This was developed by Stephan Koev for use with his chitosan microcantilever device tests. [86]
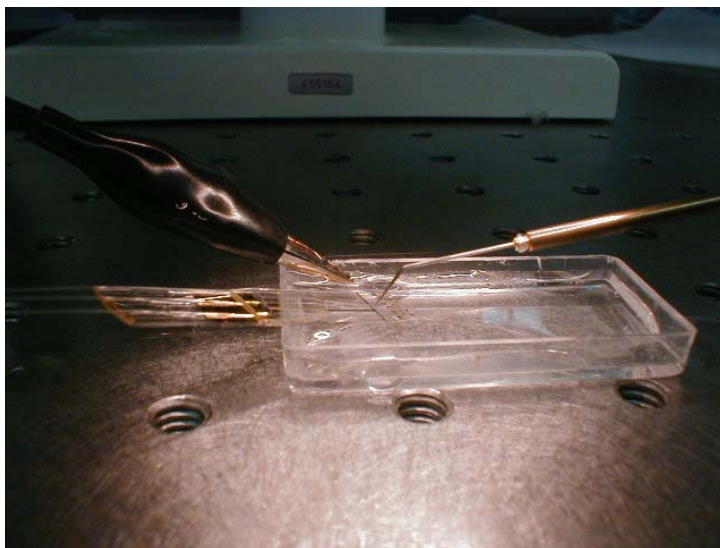
Figure 3.21: The chitosan "microdeposition" setup

Many procedures and recipes used in microfabrication require constant calibration and testing to ensure reproducible results. The deposition of chitosan is no exception. As it turns out, the deposition of chitosan is a very temperamental procedure, and calibration of the routine is difficult and frequent. Chitosan is used by several research groups at the University of Maryland campus and the results can vary from batch to batch as chitosan varies "from crab to crab".   Nonetheless, it was important to develop as best a characterization of chitosan as possible. In the past, chitosan had been deposited on gold electrodes. Li Qun (Cynthia) Wu demonstrated that chitosan could be deposited on an ITO coated glass slide. In this work, it was demonstrated that chitosan could be patterned on photolithography patterned ITO electrodes on Pyrex and polymer sidewall structures.

"Bioprobe" test chips with ITO strips were patterned at spacings of 100 and 200 μm, as shown in Figure 3.22.
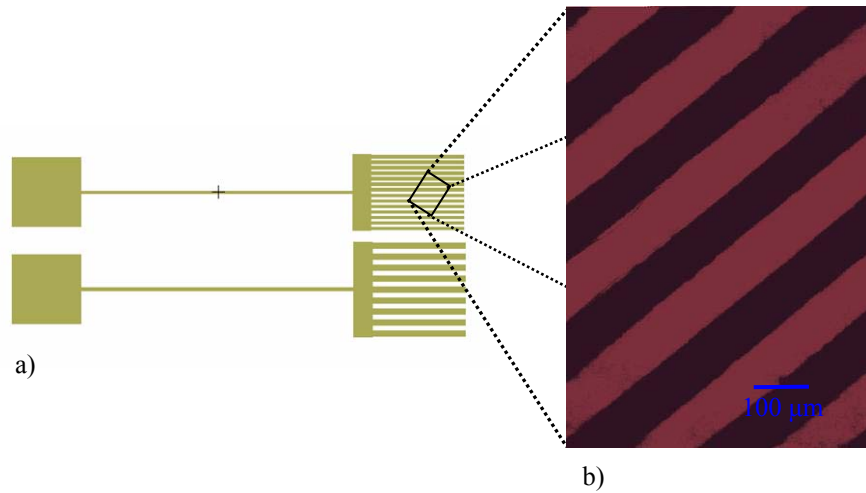
Figure 3.22: (a) Bio-Chip Metallization Structures. The top chip has a 100 μm grating and the bottom a 200 μm grating. (b) Fluorescent micrograph with Alexa Fluor 633 filter. The labeled chitosan was deposited on the ITO electrodes of the Bio-Chip structure. This was the first evidence of Chitosan deposited on patterned ITO electrodes.

The devices shown in Figure 3.22 were submerged in a beaker of chitosan solution and voltage was applied in various magnitudes and durations. One of the chief problems was the thermal fusing of the thin ITO electrode that distributed current to the electrodes at the bottom. This limited the maximum current density obtainable in testing, but provided a sufficient characterization. In the range of current densities that could be used on the bio-chips, rate data was obtained and given in Table 3.11. The deposition response over time is given in Figure 3.23.

Table 3.11: Chitosan Deposition results for bio-chip tests

Current Density →	0.83 A m^{-2}	1.19 A m^{-2}	1.78 A m^{-2}
Linear Rate	0.04 μm / minute	0.12 μm / minute	0.34 μm / minute
Maximum	N / A	2.2 μm	4.0 μm

Chitosan Deposition ITO Bio-Chips
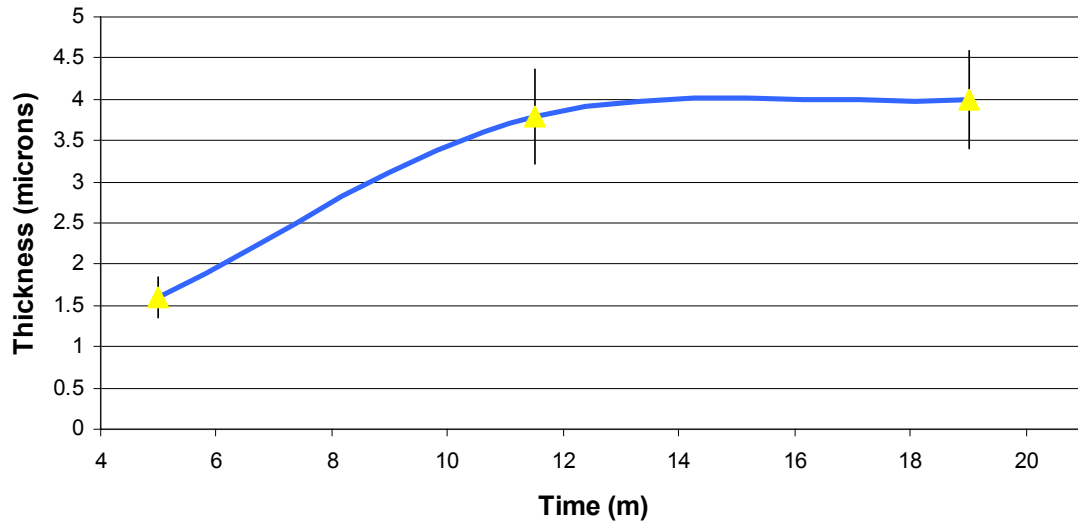
Figure 3.23: Deposition of Chitosan over time for a current density of 1.78 A m^{-2}

Finally, with the baseline characterization in hand from the bio-chip tests, chitosan could be deposited in the sensor structures. Figure 3.24 shows the results of this effort. Note that in the top-down view, the sidewall area is very bright because the effective depth of the chitosan from the viewer's perspective is quite large.

(a)

Fluid Channel

Chitosan on Sidewall

(b)
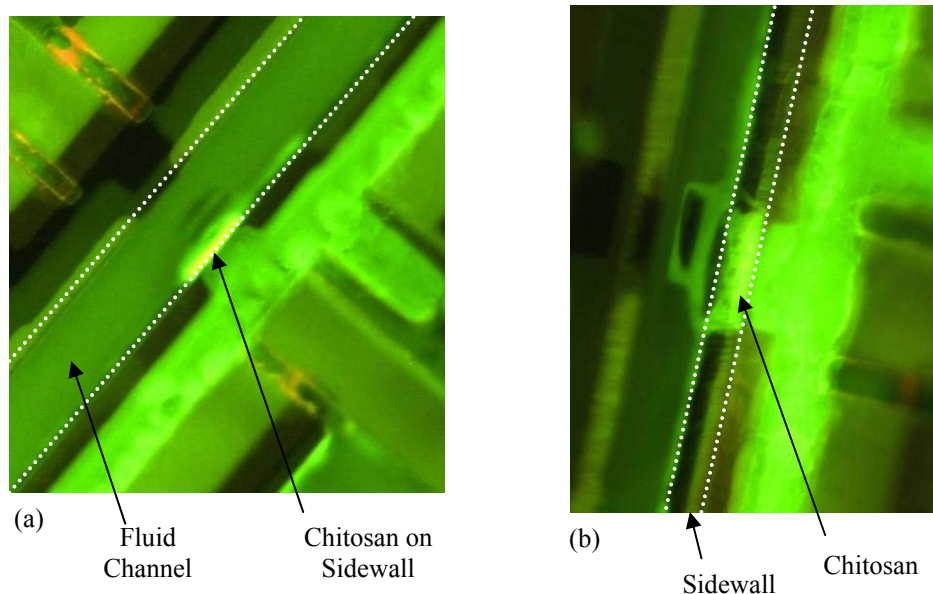
Sidewall

Chitosan

Figure 3.24: Initial results showing Fluorescein labeled Chitosan deposited on the sidewalls of a microfluidic channel. (a) shows a top-down view while in (b) the device is tilted on the fluorescent microscope stage.

SU-8

Chitosan on ITO Sidewall

ITO

| Mag = 196 X | 100µm | EHT = 10.00 kV | Signal A = MPSE | Date :15 Jun 2005 |
| | | WD = 26 mm | Photo No. = 7227 | Time :16:26:28 |
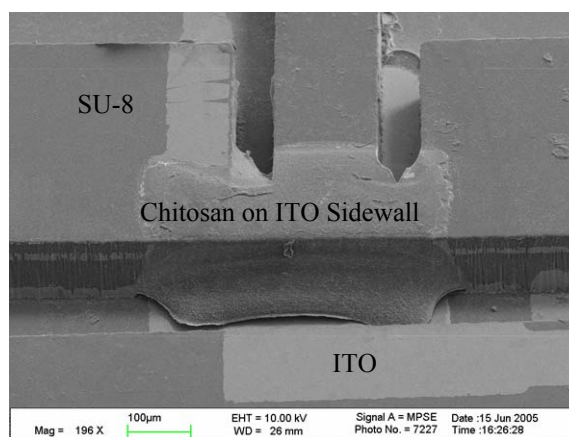
Figure 3.25: Typical SEM Image of chitosan deposited on the sidewall of a microfluidic channel.

3.3.10   DNA Functionalization

The goal of the DNA Functionalization process is to covalently tether the probe DNA to the chitosan surface, as described in Section 1.3.3 and as shown in Figure 3.26. Although this sensor could work in principle with optically active proteins, enzymes, and other biomolecules, DNA hybridization was chosen as a starting point since the chemistry is robust and tolerant to inhospitable environments such as strong pH, higher temperatures, drying and other circumstances that may occur in the normal handling and testing routines.
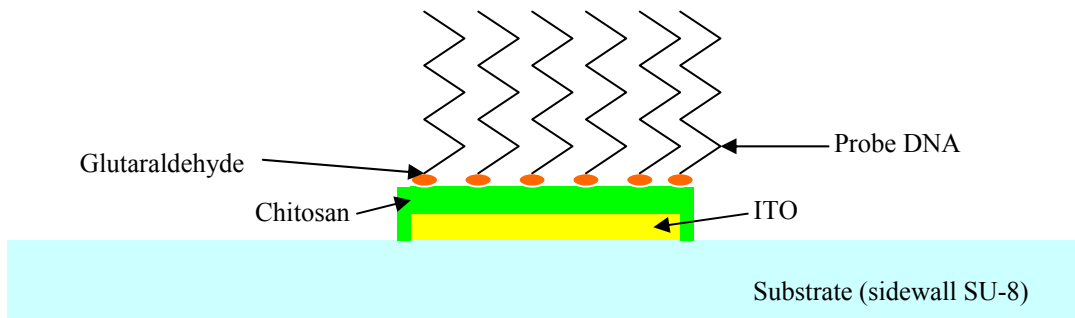
Figure 3.26: DNA Functionalization Scheme

Table 3.12 shows the DNA Hybridization recipe. The initial recipe was provided and developed in conjunction with Hyunmin Yi with UMBI. [41]   The process flow is compatible with the materials on the chips, with the exception of NaOH. Sodium Hydroxide has been found to dissolve the UV curable optical adhesive used to secure the fibers to the chip. This step can be skipped if necessary. If the step is performed with the optical adhesive on the chips, then care should be taken to apply an excess of the epoxy so that significant dissolution can occur without releasing the fibers. Attaching the fibers

after hybridization is not an option due to the UV light used for curing that could damage the chemical components on the chitosan.

In the recipe, two pH buffer solutions are referred to, SSC; Saline Sodium Citrate buffer, and PBS; Phosphate Buffered Saline. The purpose of the buffer is to compensate for pH changes in the solution which result from the processing steps such as the chitosan deposition procedure.

Cleanliness is essential to successful operation of the device. Contamination from the outside environment can prevent operation in two ways. The first is amine-group contamination. Many compounds in the environment such as biological oils from hands and the air can cause nonspecific binding between the amine sites on the probe molecules and contaminated areas of the device. If serious, the contamination could consume all of the reactants of the probe species and prevent tethering to the chitosan. The second form of contamination is nucleases, which are enzymes which break down DNA. If not treated properly these could destroy the probe and target species. Special cleaning agents, such as the commercially available "Eliminase" cleaner can avoid this type of contamination. In light of this, cleaning of the device and glassware prior to use is of critical importance. All autoclaving compatible glassware is sterilized and Alconox critical cleaning soap is used to clean every piece of equipment prior to use. All working surfaces and tools are washed with IPA and water.

Table 3.12: DNA Functionalization Procedure

Step	Procedure	Time / Temp	Purpose
1	Pre-clean: NaOH followed by IPA	5 minutes / 22C	Eradicate Biological Contamination
2	Chitosan (pH: 3.7, 0.5% wt/ vol, 375 kDa weight) deposition with probe-tip contact – 50 micro Amps	8 minutes / 22C	Deposit chitosan
3	DI Rinse	5 minutes / 22C	Flush excess chitosan solution
4	Immerse in 1M NaOH	1 minute / 22C	Neutralize chitosan (Optional- NaOH attacks NOA optical adhesive)
5	DI Rinse	1 minutes / 22C	Rinse
6	Immerse in Buffer (PBS)	5 minutes / 22C	Buffering
7	Immerse in 0.1% Glutaraldehyde solution on rocking platform	30 minutes / 22C	Cross-links deposited chitosan and activates amine sites
8	DI Rinse	5 minutes / 22C	Rinse
9	Immerse in Buffer (PBS)	10 minutes / 22C	Buffering
10	Immerse in amine-terminated ssDNA probe species solution	12 hours / 4C	Tether probe ssDNA species to chitosan
11	DI Rinse	1 minutes / 22C	Rinsing
12	Immerse in Buffer (SSC)	5 minutes / 22C	Buffering
13	Dip in Sodium Borohydride solution	1 minute / 22C	Stabilize the secondary amine groups
14	DI Rinse	5 minutes / 22C	Rinsing
15	Immerse in Buffer (SSC)	1 minute / 22C	Buffering

To test the functionalization procedure and confirm that the chitosan surface had probe DNA attached, the labeled probe ssDNA as given in Figure 1.11c was used. This caused the functionalized surface to fluoresce with Alexa Fluor 633. Confirmation of this procedure is shown in Figure 3.27.
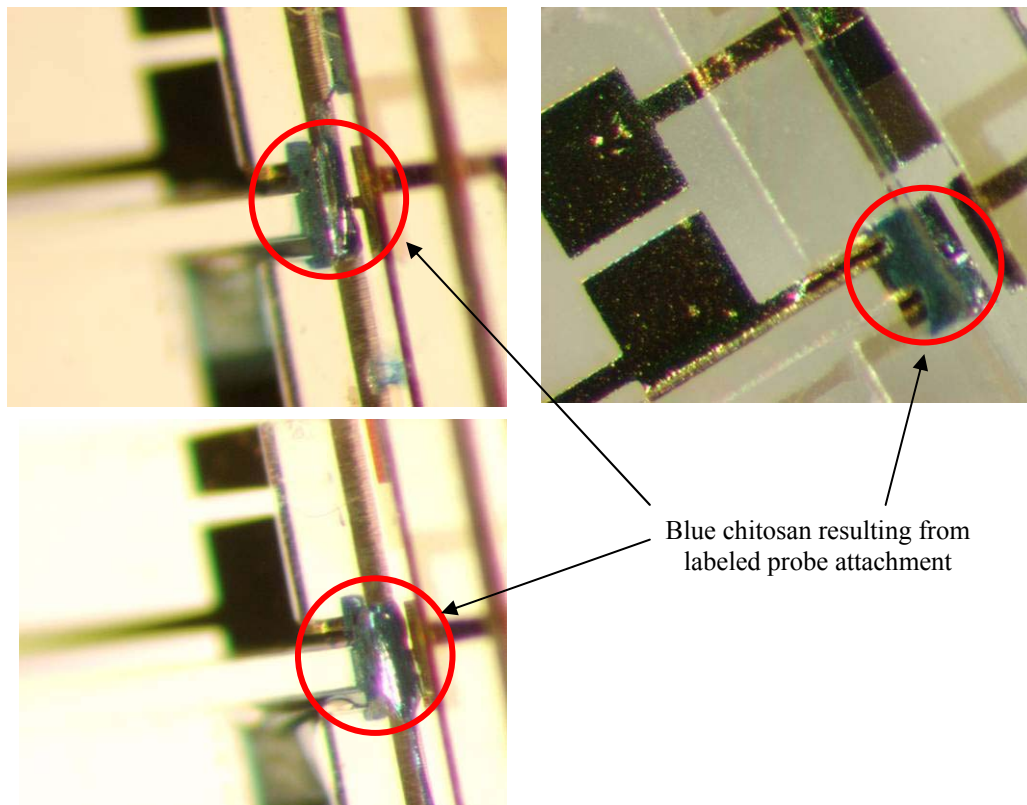
Blue chitosan resulting from labeled probe attachment

Figure 3.27: Blue chitosan in these micrographs indicates confirmation of probe ssDNA tethering

4 Experimental Method and Testing

4.1 Testing Integrated Waveguides

Low-loss waveguiding is one of the most important requirements of the device. The first tests involved determining the loss coefficients for the polymer structures. Generally, polymer waveguides are less absorbing in the red and near IR wavelengths than at shorter wavelengths in the UV to yellow and also the mid-wave IR. Selecting the right wavelength for lowest attenuation is very important. The light source for testing was a 633 nm helium neon gas laser, and this matches well with some existing fluorophores (In contrast, a closely matched 635 nm laser diode was used for operation later). A depiction of the test setup used to measure the loss is shown in Figure 4.2. Free space coupling was used, and the collection of stray light was minimized by a baffle around the waveguide and a curve at the end.   Testing was performed in a frame covered with blackout cloth to eliminate ambient light.   The output was collected by a 400 μm core fiber that was aligned to the angled output facet, while the other end of the fiber was connected to an Ocean Optics spectrometer. The cut-back method [87] was used to determine the loss per unit length by measuring the loss at different lengths. The slope of the line which relates throughput to length is the loss per unit length.   Thus, precise measurement of the absolute light output is not neccesary. For each test, the setup was aligned so that maximum throughput occurred for each test.   The data is in Figure 4.1 and fit to an exponentially decaying function which is representative of optical transmission versus distance. The attenuation at 633 nm was found to be 1.75 dB/cm. In other tests using a chrome mask instead of a transparency, the loss decreased to about 1.35 dB/cm. [74]
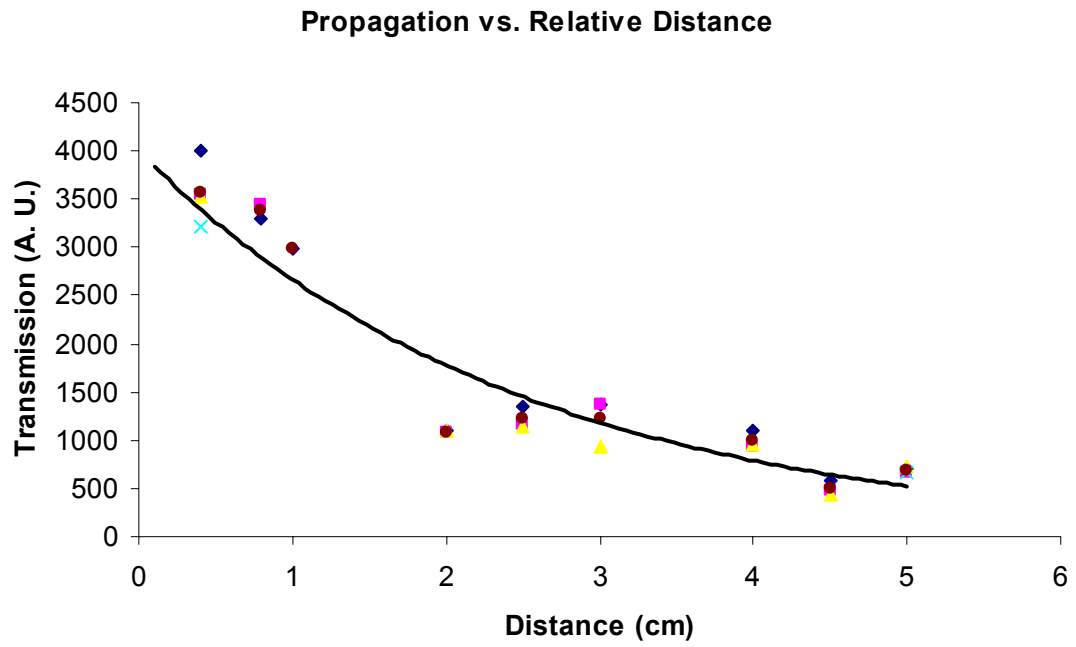
Propagation vs. Relative Distance

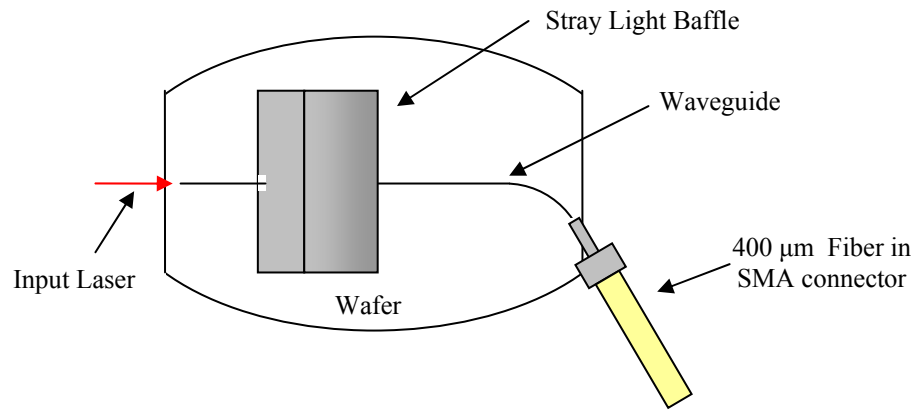**Figure 4.1: Power versus propagation in a SU-8 waveguide**

Figure 4.2: Test setup for propagation loss measurements.

4.2 Feasibility Studies with Alexa Fluor 633 Conjugated Chitosan

To date, the volumetric (or surface) density of binding sites of fluorescent molecules onto chitosan is not well understood. Furthermore, the properties (such as quantum yield) of fluorescent materials are not well characterized under a wide range of environmental conditions. Thus it was not clear from the outset that enough fluorescence could be excited and captured to make a measurement. Therefore, one of the first steps was to demonstrate that a signal could be obtained from a fluorescent chitosan material under best-case circumstances and without the added complication of DNA materials. To do this, Alexa Fluor 633 (AF633) dye was conjugated directly to chitosan resulting in an intrinsically fluorescent chitosan material as described in Section 1.3.3. The chitosan-AF633 conjugate has the best possible output signal because it represents the maximum fluorescence obtainable with chitosan due to the high concentration of fluorophores. This high concentration results from the fact that the fluorophore is conjugated directly to chitosan and by that a high rate of binding of the fluorophores to chitosan amine groups is realizable. Indirect binding with DNA and other coupling schemes yield lower total fluorescence. The chitosan was deposited in the device as described previously. Several configurations were examined to determine the optimal fluorescent signal. Ultimately it was found that the "top-down" configuration to be depicted in Figure 4.10a and Figure 4.10b had the highest signal to noise ratio. Figure 4.3 shows the results from these tests and the clear evidence of signal collection from the chitosan-AF633 conjugate. Note that the sharp spike in the figure represents the laser input which was suspended above the sensor. The prominent peak to the right is the fluorescence from Alexa Fluor 633.
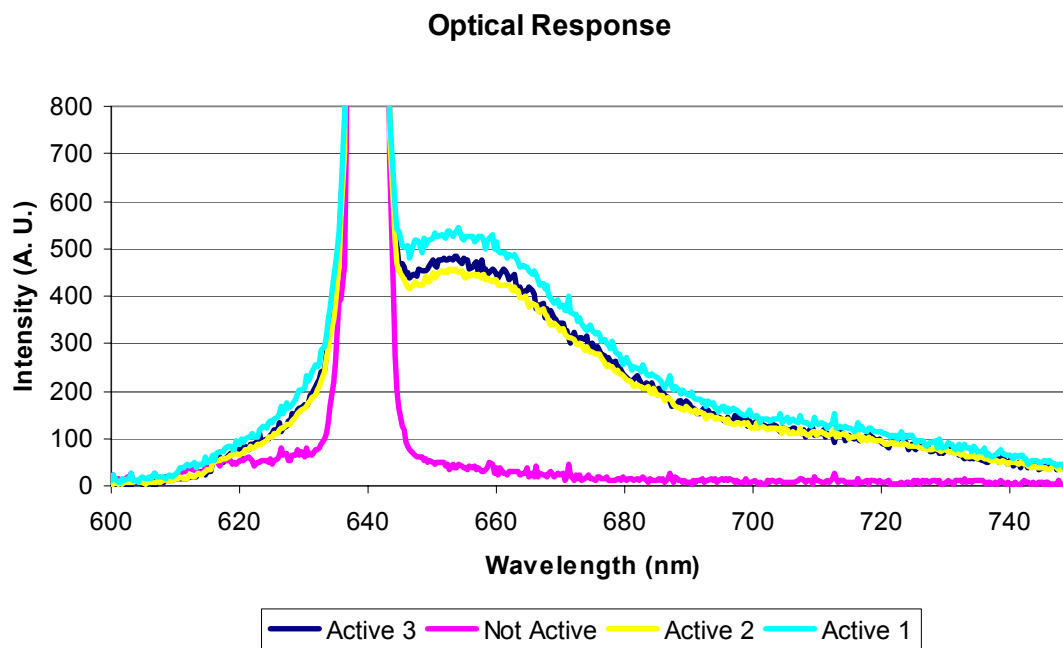
Optical Response

Figure 4.3: The optical response of chitosan-AF633 conjugate deposited in the sensor.

4.3 DNA Hybridization Biosensor

Following the fabrication process and ssDNA probe activation (See Section 3.3.10), the device is ready for testing and should not exhibit fluorescence. The measurement aims to examine the optical intensity beyond 650 nm which is the result of fluorescently labeled ssDNA targets that will be attached by DNA hybridization. Note that the specificity of the binding has not been firmly established here.

4.3.1 DNA Probes and Targets

DNA Probes and Targets were synthesized by Gene Probe Technologies in Rockville, MD. Section 1.3.1 details the function of each type of probe, and the actual sequences are given in Table 4.1.

Table 4.1: DNA Probe Synthesis Data

Type	*ssDNA sequence*
Labeled Probe	5' – (Amino C6 Linker) – C-T-T-T-C-g-C-g-T-T-g-T-T-T-g-C-A-g-A-A – 3' (Alexa Fluor 633)
Probe	5' – (Amino C6 Linker) – C-T-T-T-C-g-C-g-T-T-g-T-T-T-g-C-A-g-A-A – 3'
Matching Target	5' (Alexa Fluor 633) – T-T-C-T-g-C-A-A-A-C-A-A-C-g-C-g-A-A-A-g – 3' (Alexa Fluor 633)
Mismatching Target	5' (Alexa Fluor 633) – C-A-T-C-A-T-C-A-T-C-A-T-C-A-T-C-A-T – 3' (Alexa Fluor 633) **Histadine Sequence**

4.3.2 Hybridization Procedure

Following the DNA probe tethering detailed in Section 3.3.10, the device is ready for hybridization. One of the key considerations in a hybridization experiment introduced in Section 1.4 is the buffering solution used. The buffer can raise and lower the kinetic energy requirement that the target DNA needs to "hop around" and find the best match. Sigma-Aldrich produces a "PerfectHyb" hybridization buffer explicitly intended for this purpose. It contains a proprietary mixture including soap (SDS) and formaldehyde. Sigma-Aldritch claims an enhancement factor in hybridization of 2-5, with no enhancement of nonspecific binding. [88]

Table 4.2: DNA Hybridization Procedure [41]

Step	Procedure	Time / Temp	Purpose
1	Record baseline spectral measurement	22 C	Establish baseline spectra to compare
2	Rinse in DI water	5 min / 22 C	Rinsing
3	Rinse in SSC	5 min / 22 C	Rinsing
4	Immerse in PerfectHyb buffer with target DNA	30 min / 22 C (or 35 C)	Hybridization of Target DNA to Probe DNA
5	Record optical spectrum measurement	22 C	Compare activated spectra to baseline
Optional	Immerse in higher concentration target DNA	30 min	Bind more target DNA at a higher concentration
Optional	Denature with 4M urea solution	30 min / 35 C	Remove target DNA, recycle device

The results of this procedure when hybridized with a matching ssDNA Target sequence are seen with a fluorescence microscope are in Figure 4.4 and Figure 4.5. The color discrepancy between the two is the result of different color camera systems.
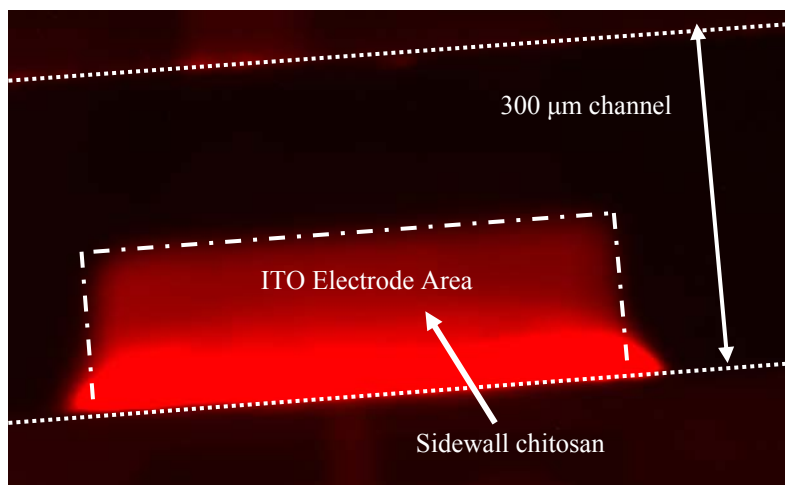

Figure 4.4: Fluorescent micrograph showing target DNA activated chitosan. The sidewall coverage is highly evident.
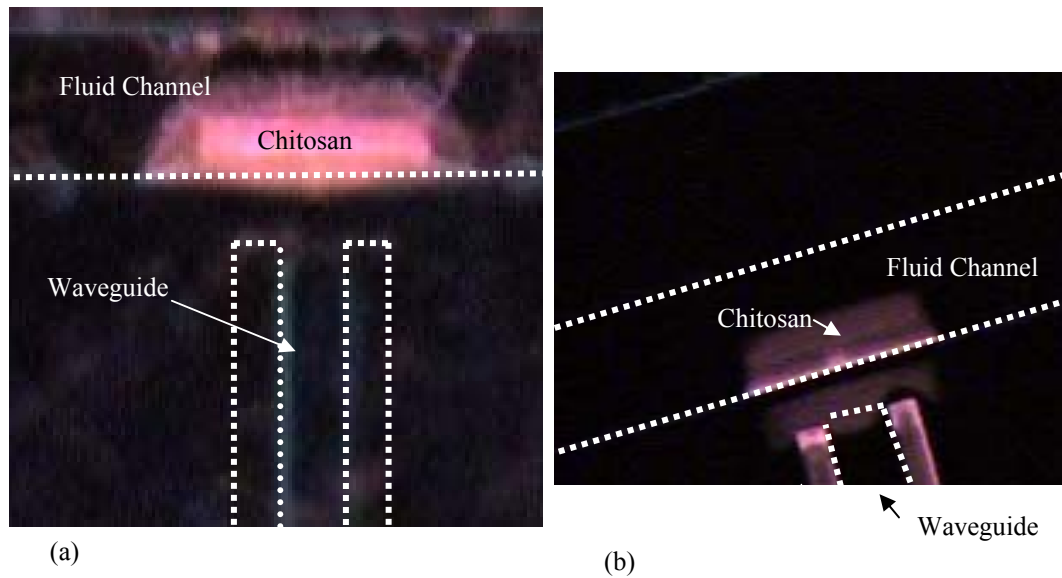
Figure 4.5: Fluorescent micrographs of target DNA activation. (a) Hydrogel deposition; (b) Thin film deposition where the reflection from the underlying gold is visible.

4.4 Optical Test Systems

Several optical test systems were developed to interface with the microfabricated device. The systems could be grouped according to the mode of operation: either transmission mode; where the forward scattering fluorescence and excitation light is sent from an input waveguide to an output waveguide or reflection mode; where a single waveguide is used to send the excitation light and extract the backscattered fluorescence. Additionally, the systems can be grouped as in-plane or out-of-plane. In-plane test systems have the light remain in a plane parallel to that of the substrate, while out-of-plane systems have light directed in planes defined by vectors with components normal to that of the substrate. Generally, in-plane systems are preferred because they have the most straightforward integration path to self-contained lab-on-a-chip systems.

Table 4.3: Test Equipment

Item	Description	Configurations Used
Laser Diode	PD-LD 1.2 mW, 9 μm core fiber pigtailed, $\lambda_c = 635$ nm	Normal, Reflection
Spectrometer	Ocean Optics USB 2000	All
Photodetector	Newport 818 SL Picowatt detector	All
Optical Fiber	Corning Infinicor 300 62.5 μm core	All
Gas Laser	He-Ne Gas Laser, 5 mW, $\lambda_c = 633$ nm	Propagation Loss Measurement

4.4.1 Power Budget

The power budget gives a component by component breakdown of the losses in the system. It represents the conversion ratio between photons from the laser diode to photons in the detector. This helps predict the sensitivity of the instrument and also suggests possible areas for optimization. Figure 4.6 illustrates the system loss element and Table 4.4, Table 4.5, and Table 4.6 give the budgets for each configuration in terms of the forward direction which is the excitation light going into the chip, and the backward direction which is the emission light away from the chip into the detector, the budget for the return direction, and the round-trip budget. With the exception of the bandpass filter, the losses can be assumed to be independent of wavelength for the narrow range considered here.
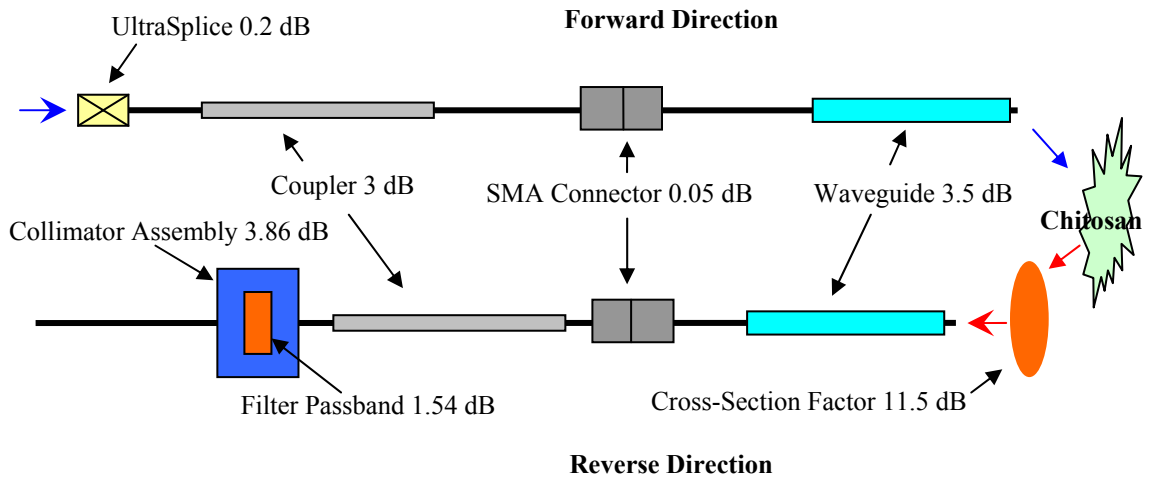
Figure 4.6: Diagram of system loss elements. Not every configuration includes all loss elements.

Table 4.4: System power budget from measurements for reflection mode. The calculations only account for the spectral passband of the emission filter.

Component	Loss
UltraSplice Loss	0.2 dB
Directional Coupler	3 dB
SMA Sleeve Connector	0.05 dB
Waveguide Loss	3.5 dB
Total Forward Loss:	6.75 dB
Cross Section Factor	11.5 dB
Waveguide Loss	3.5 dB
SMA Sleeve Connector	0.05 dB
Directional Coupler	3 dB
Filter Collimator Loss	3.86 dB
Filter Passband Loss	1.54 dB
Total Backward Loss:	23.45 dB
QE Estimate:	3 dB
Round-Trip Loss:	33.2 dB

Table 4.5: Transmission mode power budget. The calculations only account for the spectral passband of the emission filter.

Component	Loss
UltraSplice Loss	0.2 dB
SMA Sleeve Connector	0.05 dB
Waveguide Loss	3.5 dB
Total Forward Loss:	3.75 dB
Cross Section Factor	11.5 dB
Waveguide Loss	3.5 dB
SMA Sleeve Connector	0.05 dB
Filter Collimator Loss	3.86 dB
Filter Passband Loss	1.54 dB
Total Backward Loss:	20.45 dB
QE Estimate:	3 dB
Round-Trip Loss:	27.2 dB

Table 4.6: Normal mode power budget. The calculations only account for the spectral passband of the emission filter.

Component	Loss
Total Forward Loss:	0 dB
Cross Section Factor	11.5 dB
Waveguide Loss	3.5 dB
SMA Sleeve Connector	0.05 dB
Filter Collimator Loss	3.86 dB
Filter Passband Loss	1.54 dB
Total Backward Loss:	20.45 dB
QE Estimate:	3 dB
Round-Trip Loss:	23.45 dB

A round-trip loss of 33.2 dB in the reflection mode configuration means that of the 1.2 mW from the laser, 574 nW of emission makes it to the detector, assuming that all the photons that make it into the chitosan are fluorescently converted with assumed quantum efficiency of 50%. In practice, not all of the impinging photons will be converted. The

137

absorption and conversion of excitation photons to emission photons depends on the fluorophore absorption. For conditions where all excitation light is not absorbed, the effective conversion efficiency will be less. For detector selection and estimation it can be assumed that about 1 - 10% of the emission light from the chitosan layer gets to the detector or spectrometer.

4.4.2 Transmission Mode

The first test setup used transmission mode measurements to obtain a fluorescent signal response. Transmission mode is also useful in absorbance measurements, where the concentration of an analyte is measured by the attenuation of an input signal.
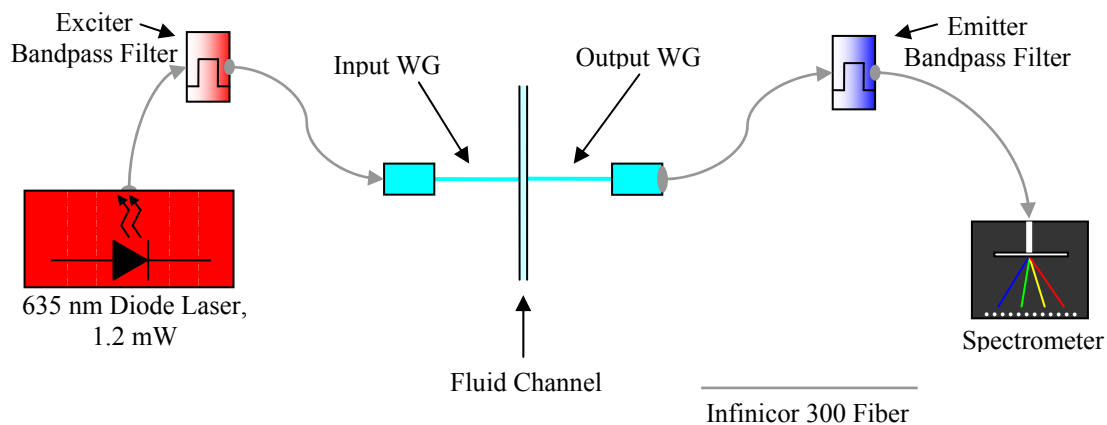

Figure 4.7: Transmission Mode System Setup

The exciter and emitter bandpass filters were obtained from Chroma Technology Corporation (Rockingham, VT). The filters correspond well with Alexa Fluor 633 as shown in Figure 4.8.
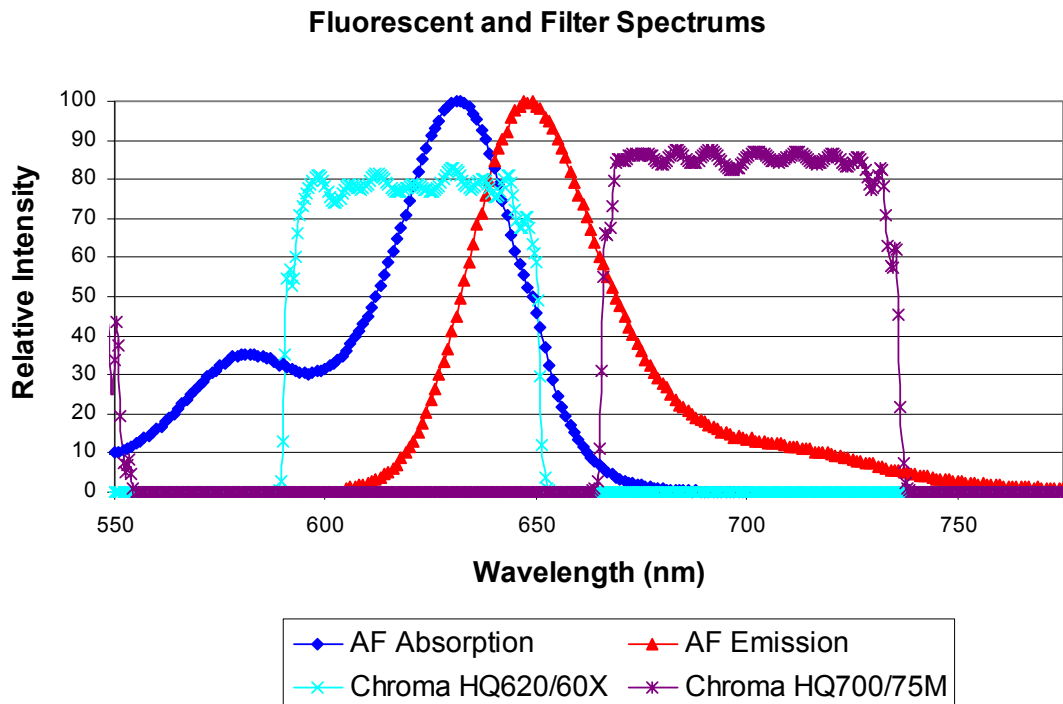
Fluorescent and Filter Spectrums

Figure 4.8: Alexa Fluor 633 spectrum as obtained from Molecular Probes and Chroma filter set 41008 spectral characteristics. Blue and Light blue represent the absorption and absorption filter spectra, respectively as red and maroon represent the emission spectrum and the emission filter spectrum.

Transmission mode is challenging to implement and measure because the fluorescent emission intensity is extremely small when compared to the excitation intensity, both of which are passed directly through to the detector in this case. The great disparity is the result of the thin chitosan layer not completely absorbing all of the emission, the quantum yield of the fluorophore, and the directed nature of the excitation versus the undirected nature of the emission (high versus low brightness). This is a problem despite the fact that the output light goes through a filter. Even the best filters can only be expected to give about 40 to 50 dB of out-of-band attenuation which is not sufficient, given the overwhelming predominance of the excitation signal. Thus, it is nearly impossible to

extract the fluorescence signal using interference filter techniques.   As a further complication, under some conditions the "laser tail" can become a problem. Although laser emission is predominately monochromatic, some of the light is emitted at wavelengths in the vicinity of the central frequency. This is typically minute in intensity, so is the fluorescence. This can be an issue when the fluorescent intensity is very low or the laser source is operated at below threshold where the cavity feedback is not very strong. Although the loss for the reflection mode system is greater than that of the transmission mode, these complications make reflection mode more favorable. Figure 4.9 illustrates this problem. Although the bandpass filter strongly attenuates the excitation light and leaves the emission light undiminished, it still is not enough to allow the emission to dominate the total output.
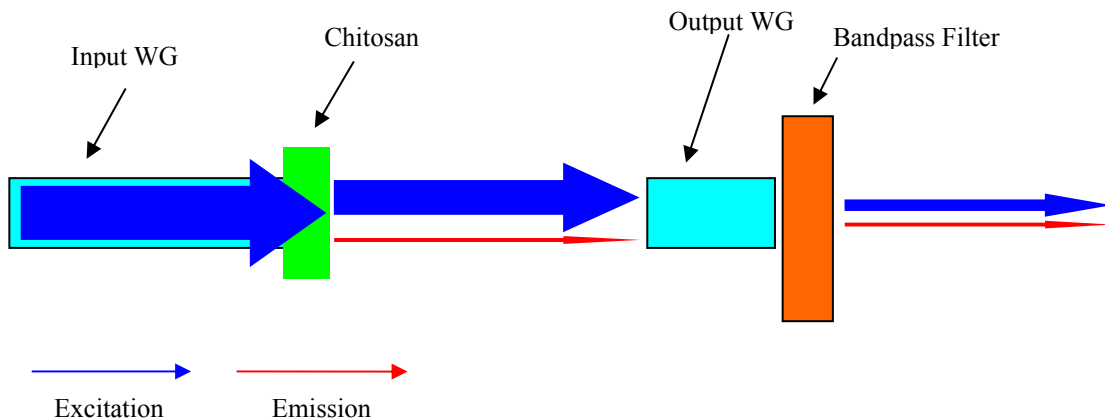

Figure 4.9: Not-to-scale figure demonstrating the difficulty of using transmission mode.

Detecting absorbance can be difficult as well. As explained in the introduction, the absorbance depends upon the optical interaction length.   The sidewall deposition

technique yields an interaction length equal to the thickness of the chitosan which is only several microns, so the absorbance is not very strong.

4.4.3 Normal Illumination

To eliminate the signal to noise problems in transmission mode measurements, a "normal illumination" technique was tried that did not require any changes to the device structure. Instead of using a two waveguide system with input and output waveguides, this technique shines light down onto the chip from an out-of plane source while one on-chip waveguide is used to collect the emission. This effectively puts the excitation and emission collection directions at right angles to one another and dramatically reduces the amount of excitation light that is collected by the output waveguide. The disadvantage of this technique is that it is out-of-plane and poses difficulties for monolithic integration.

There were two sources used for these tests as illustrated in Figure 4.10 and Figure 4.11. The first was a diode laser which was pigtailed to optical fiber, where the fiber was suspended and aligned over the device under test. The second was a fluorescent microscope with an appropriate filter set.
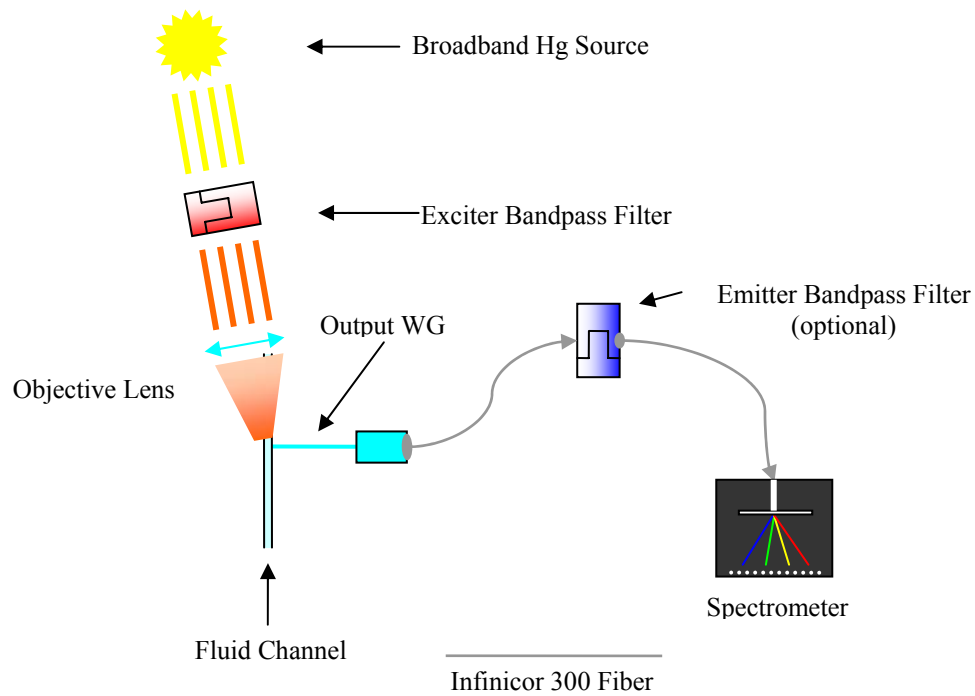
Figure 4.10: Normal Illumination Test Setup

Using a microscope as the light source provides the additional advantage that the sensor can be inspected with the microscope's camera during testing to provide for reproducible intensity (prescribed by focus) and alignment. In a clinical or research environment where a device such as this could be used, a microscope can be used in conjunction with the optical waveguides for additional information about the sample.
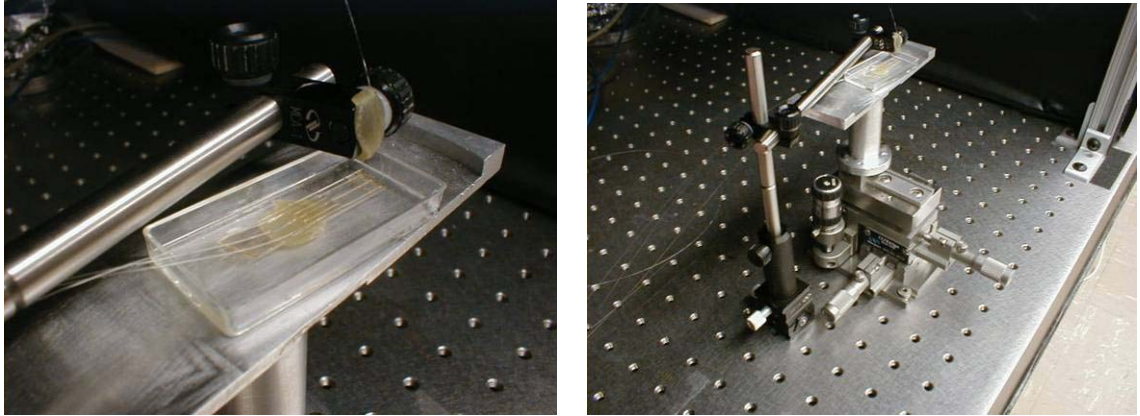
Figure 4.11: Optical Fiber Illumination Method

The signals obtained using the above setup were considerably better than those using transmission mode techniques. Figure 4.12 and Figure 4.13 show the spectral content of the output waveguide of an activated device. In both cases the scattered excitation light is visible as a very sharp peak. The fluorescent emission is the broad peak to the right. Even in normal illumination mode, where the emission and excitation capture are offset, the scattering of the excitation light is still much greater than the fluorescence, although the intensity in the "tail" is not.

Normal Illumination with Microscope

Figure 4.12: Normal Illumination with Microscope

AF 633 labeled Chitosan

Figure 4.13: Spectrum with laser excitation

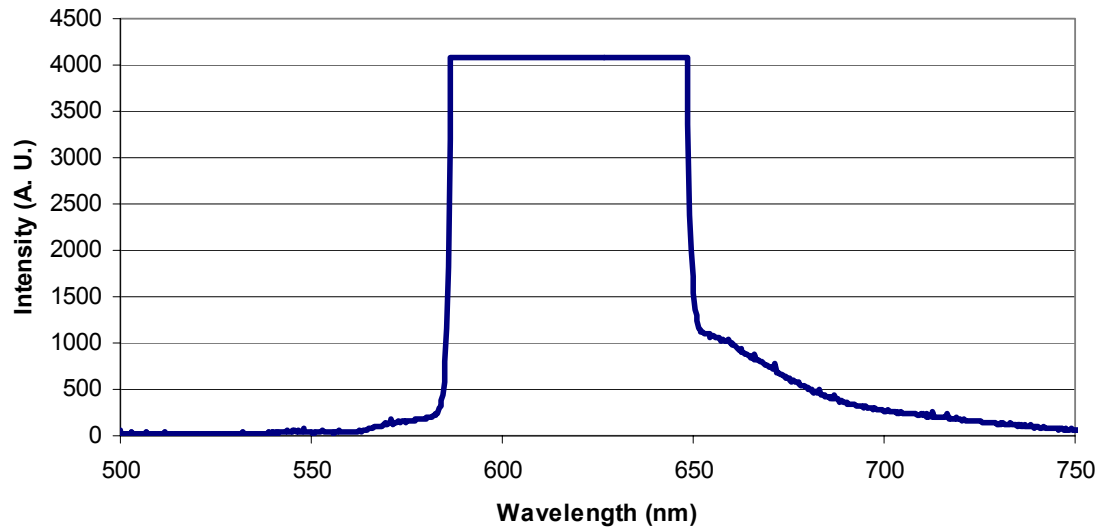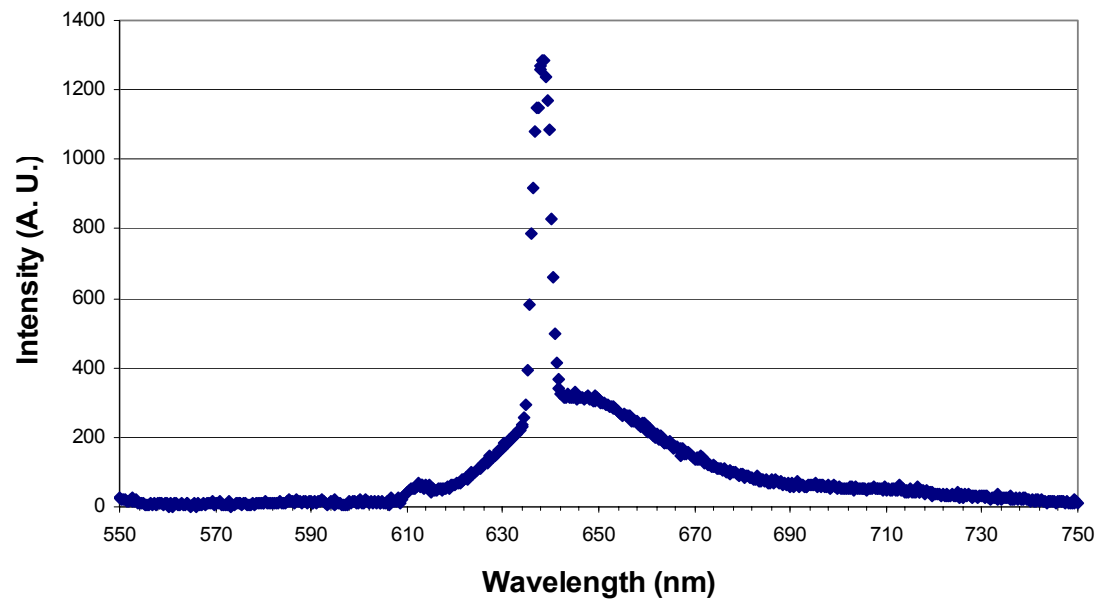After the normal illumination measurement mode had been proven to be robust and repeatable, measurements of the fluorescent emission were taken after ssDNA probe activated chips were exposed to successively increasing concentrations of ssDNA targets. The response of the device, in arbitrary units, was calculated by integrating the arbitrary unit intensity from the spectrometer from 652 nm to the long wavelength limit of the spectrometer which is 1025 nm. These results were averaged and plotted in Figure 4.14. The overall shape of the curve is consistent with the expectation that the ssDNA probe sites on the chitosan become saturated with increasing target ssDNA concentration.

Response at various concentrations
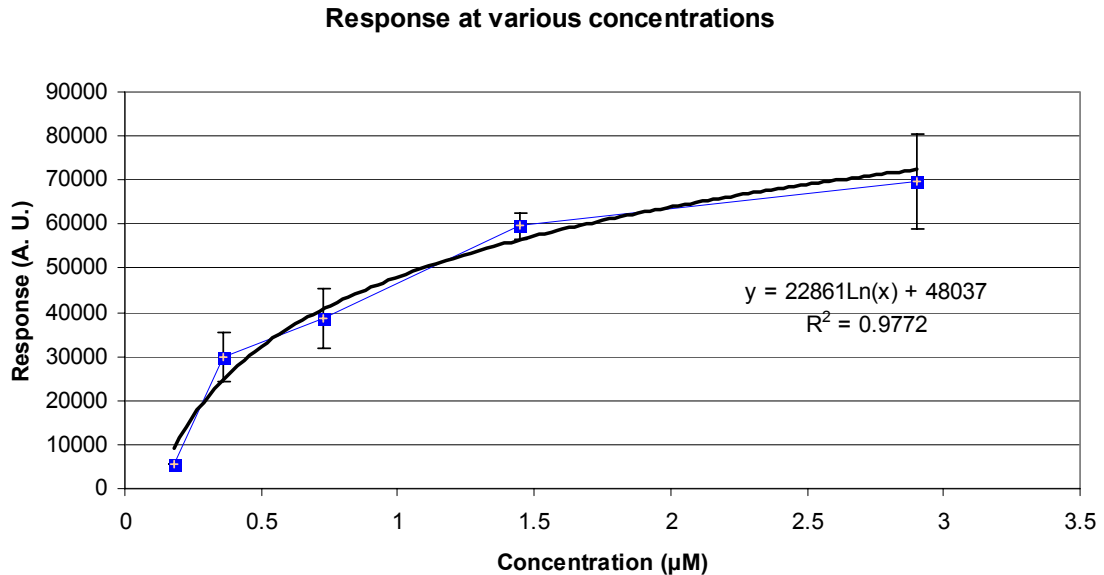
Figure 4.14: Optical response versus concentration for 7 devices.

4.4.4 Reflection Mode

In reflection mode, the overwhelming intensity of the excitation light is avoided by collecting only backscattered light. Although it is disadvantageous in all modes of operation that the emission light is spontaneous and undirected and thus can not easily be collected in its entirety by a waveguide, this fact becomes helpful in reflection mode

because half of the emission counter-propagates to the excitation light. When the collection waveguide only collects backscatter, most of the excitation light is automatically eliminated because it remains in a forward direction. Unfortunately, there is always some backscattered excitation that results from Fresnel reflections, roughness, and other effects. Although far less intense than the original excitation light, this is still considerable compared to the backscattered fluorescence. This is a common technique that was illustrated in Figure 1.4. To interface with a single input/output waveguide, a directionally sensitive splitting component is required. There are several ways to do this. One could use a partially reflective mirror, evanescent coupler, or circulator. Evanescent couplers have been fabricated in MEMS previously and can be done entirely with planar waveguides. [89] Using a coupling technique established in MEMS for the initial tests in this thesis should pave the way to further integration in the future. Directional couplers have existed for some time and can be constructed from tapered and precisely aligned optical fiber. The light is exchanged by coupled evanescent fields, a description of which can be found in Reference [57]. Figure 4.15a shows the configuration of the system while Figure 4.15b shows the splitting properties of the evanescent coupler. Couplers are available in a variety of different ratios. Since one can make a fiber pigtailed laser quite powerful, powers of 1 to 4 mW are available in multi-mode fiber, one can select a laser with surplus power, inject only a tenth into the device, but collect 90% of the backscattered emission. Since emission light is far more precious than the excitation, most of the excitation can be discarded in favor of collecting the maximum amount of emission.
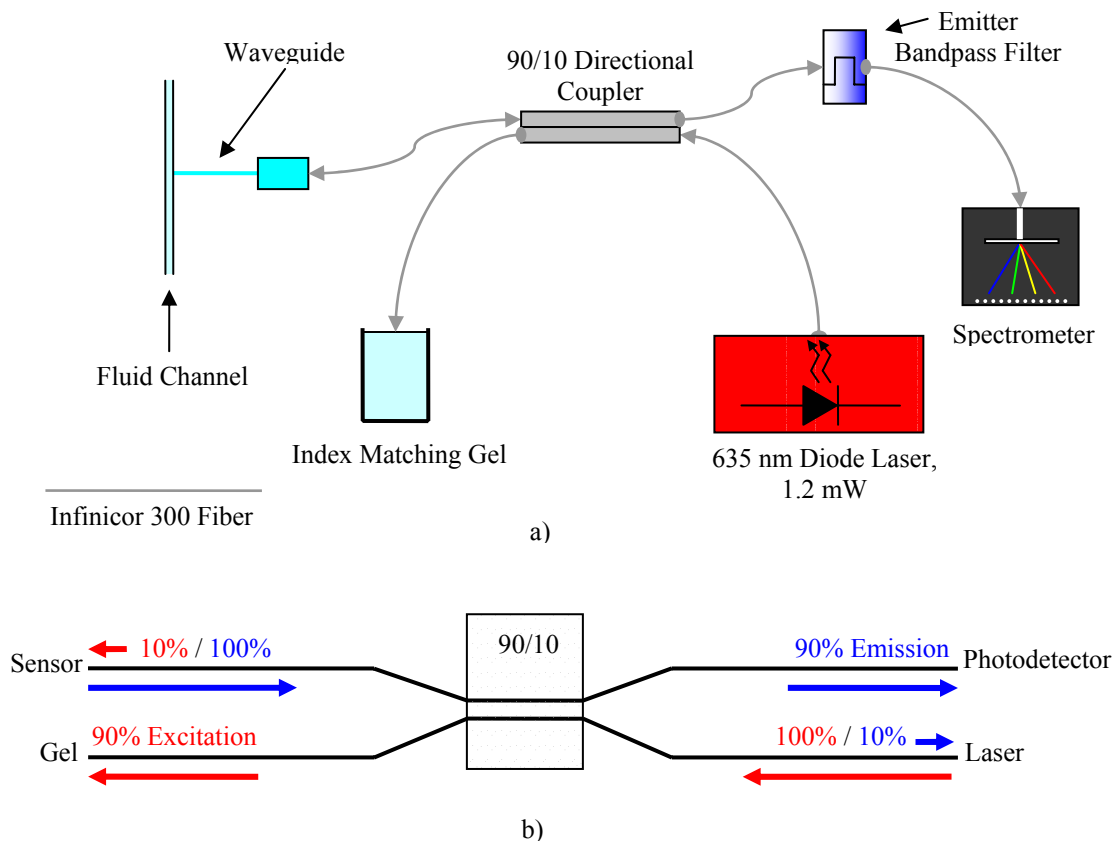
Figure 4.15: a) Reflection Mode System b) Evanescent coupler power flow under ideal conditions with zero reflections.

On an optics bench, the device was connected as shown to the other components. Index matching gel was used on the coupler arm that discards the excess laser power to reduce Fresnel reflections from the fiber facet. The test was carried out with the labeled probe ssDNA (shown in Figure 1.11), which should provide a stronger signal than the hybridization reactions. The glutaraldehyde activated chips described in Section 1.4 were first baselined. The baseline signal represents that backscattering of the excitation light

that will be present regardless of the fluorescent signal. Next, the chip was placed in a

solution of buffer and probe ssDNA for 30 minutes at room temperature. Great care was

taken not to disturb any of the fibers or connections as power fluctuations due to changes

in coupling and bending loss might interfere with the measurement. After the reaction

was completed, the measurement was taken again. Both a spectral and raw power

measurements were taken and recorded. The results demonstrate a clear capture of the

fluorescence signal as shown in Figure 4.16 and Figure 4.17.

DNA Functionalization Signal
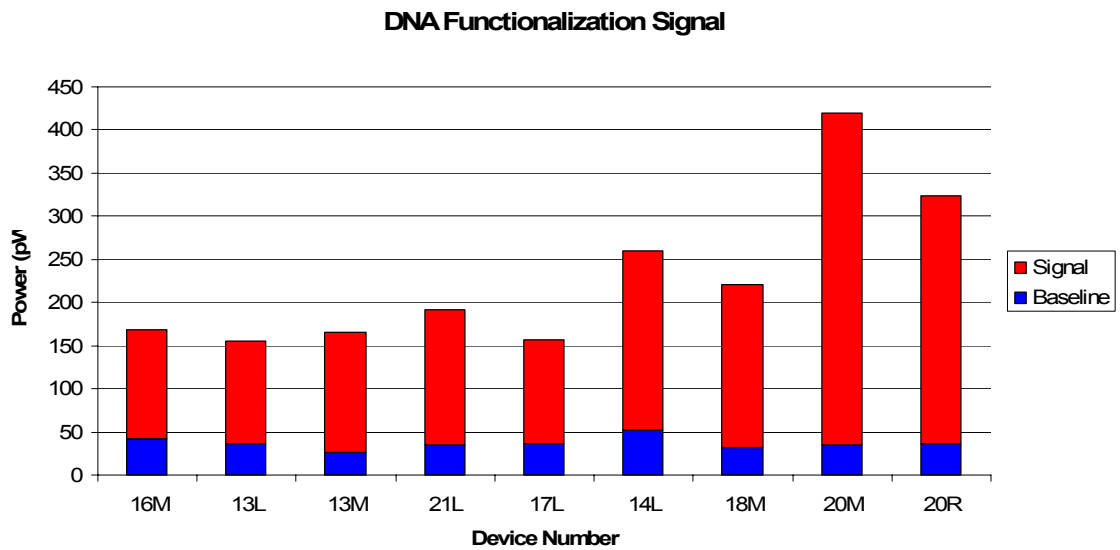
Figure 4.16: Power response of devices

Spectral Response to DNA Functionalization
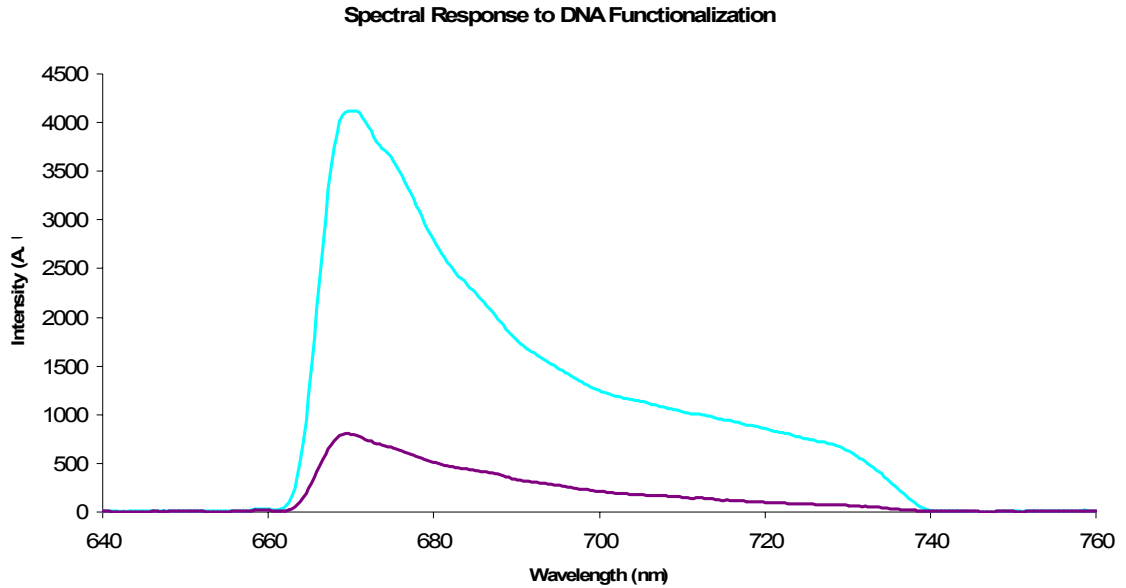
Figure 4.17: Spectral response of devices. Two representative curves are shown. Purple is before DNA functionalization, Light blue is after.

The magnitude of the response signal is highly repeatable and is reasonable when the link budget is considered. It is within the reliable range of the low power Newport 818 SL detector used in the experiments.

5 Conclusion and Future Work

This thesis demonstrated the design, fabrication, and testing of a biophotonic sensor using chitosan. Three different designs were created and fabricated, including the I-Cell, C-Cell, and Z-Cell. Each was quantitatively analyzed for efficiency, and it was found that the I-Cell was the superior choice. The design objectives necessitated that the optically and biologically active material be deposited on the sidewalls of a microfluidic channel. To address this requirement, a specialized sidewall deposition process was developed

using ITO. This work proved ITO to be a suitable substrate material for chitosan deposition, demonstrated that it can be applied for sidewall patterning. This sidewall patterning and the subsequent thick sidewall deposition of chitosan is a reliable means to achieve good optical coupling in microfluidic channels. Furthermore, this work has shown the detection of fluorescent species on the sidewalls of the channels using several optical test setups. In this way, the feasibility of the chitosan platform for in-plane optical detection was evaluated. A robust understanding of the quantitative design trade-offs and techniques for optical test systems have also been developed.

The next waypoint on a roadmap to developing integrated sensor systems will be the demonstration of the sensor in a microfluidic environment, with in-channel reactions and in-channel chitosan deposition. One of the unique advantages to the chitosan platform is the ability to biofunctionalize surfaces within microfluidic channels after the channel has been sealed. This is a dynamic process that could create flexible and user-definable reaction cambers for cellular physiology experiments and bio threat detection. Furthermore, chitosan can be selectively deposited, washed away with acid, and re-deposited. This capability could pave the way for programmable bio-chips, much like EPROMS are today.

Still, new designs and other related avenues can be explored. The end-facet detection method is not the only means to use chitosan as a biophotonic platform. Chitosan deposited on the surfaces of waveguides can exploit the evanescent field for coupling of excitation and emission. Several researchers have tried using other materials in this way,

including using resonating structures. [90, 91] The designs presented here could be tried with other materials. SU-8, while possessing significant advantages, should not be settled upon for future devices. Polymers with higher optical index may be able to increase the capture cross section. Inorganic materials, while not capable of significant thickness could be explored in the future. Silicon Nitride has a refractive index of 2.0, and if fluorescent molecules can be found in a region of significant transmittance this could be a viable option. It is likely that the size of the sensors will have to shrink considerably to use CVD deposited inorganics like Silicon Nitride.

Further work should focus on the integration of the test setup of Figure 4.15. The individual components of that scheme have already been fabricated in other projects as stand-alone components. Evanescent couplers are typically constructed from planar waveguides. Also, waveguide Bragg gratings could take the place of the filter in the setup. One of the key problems will be the integration of sources and detectors on the same chip, since Pyrex is optically inert at the wavelengths of interest. Detectors could be installed by bonding a silicon wafer to the glass with p-i-n or APD diodes. However, indirect-bandgap silicon is certainly unsuitable for excitation sources. Some other researchers have proposed using self-assembled III-V semiconductors as sources. [92, 93]. These could be assembled to interface with integrated waveguides as shown in Figure 5.1.
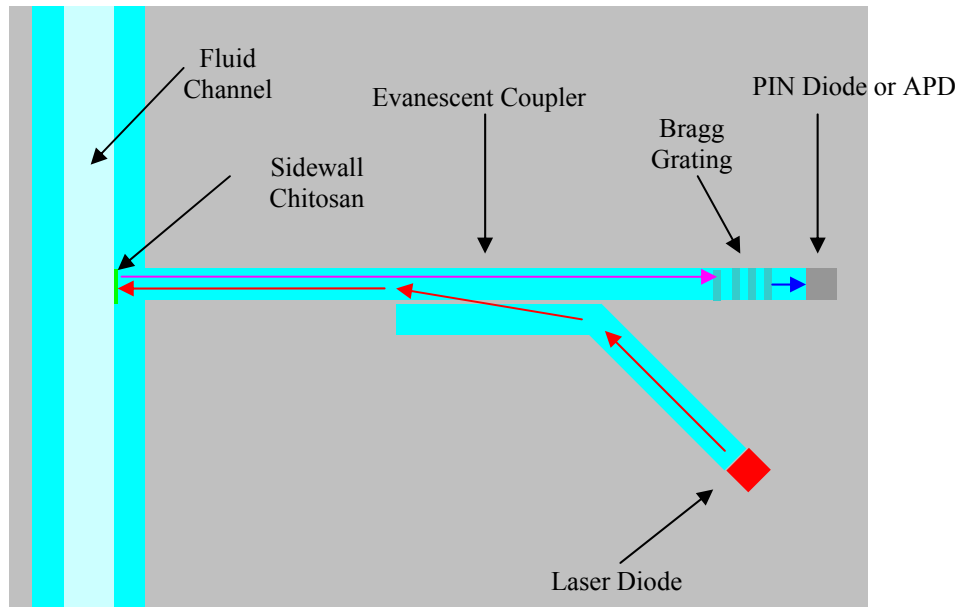
Figure 5.1: An integrated chitosan-based detection system. Wavelength dependent couplers, specific filters, and detectors are integrated with the waveguide and sidewall chitosan sensor.

Lastly, it is hoped that the design, method, and process described here will serve as the foundation for future work using chitosan as a biophotonic sensing platform.

REFERENCES

1 Li, L-Q., Davis, L. M., "Single photon avalanche diode for single molecule detection", *Review of Scientific Instruments*, **64**, 1524-1529 (1993).

2 Orrit, M., Bernard, J., "Single Pentacene Molecules detected by fluorescent emission in a p-terphenyl crystal," *Physical Review Letters,* **65**, 2716-2719 (1990).

3 Moerner, W. E., Kador, L., "Optical detection and spectroscopy of single molecules in a solid", *Physical Review Letters ,* **62**, 2535-2538 (1989).

4 Johnson, P. A., Barber, T. E., Smith, B. W., Wineford, J. D., "Ultralow detection limits for an organic dye determined by fluorescence spectroscopy with laser diode excitation", *Analytical Chemistry*, **61**, 861 (1989).

5 Prasad, P. N. Introduction to Biophotonics, Wiley-Interscience, 2003, Hoboken, New Jersey.

6 Friend, S. H., Stoughton, R. B., "The Magic of Microarrays", *Scientific American*, **286**, 44-53 (2002).

7 Affymetrix Corporation, www.affymetrix.com

8 Krasnoslobodtsev, A. V., Smirnov, S. N., "Effect of Water on Silanization of Silica by Trimethoxysilanes", *Langmuir*, **18**, 3181-3184 (2002).

9 Kuswandi, B., Andres, R., and Narayanaswamy, R., "Optical Fiber Biosensors Based on Immobilized Enzymes", *Analyst*, **126**, 1469-1491 (2001).

10 Wolfbeis, O.S. Fiber Optic Chemical Sensor and Biosensors, Volume I, CRC Press, Boca Raton, Florida, 1991.

11 Abel, A. P., Weller, M. G., Duveneck, G. L., Ehrat, M., Widmer, H. M., "Fiber Optic Evanescent Wave Biosensor for the Detection of Oligonucleotides", *Analytical Chemistry*, **68**, 2905 (1996).

12 Fang, X., Tan, W., "Imaging Single Fluorescent Molecules at the Interface of an Optical Fiber Probe by Evanescent Wave Excitation", *Analytical Chemistry*, **71**, 3101 (1999).

13 Hodzic, V., *Studies of Tapered Single-Mode Optical Fiber Devices for Hybridization-Based Biosensing and Other Applications*, Ph.D. Thesis, University of Maryland, 2002.

14 Rife, J.C., Miller, M. M., Sheehan, P. E., Tamanaha, C. R., Tondra, M., Whitman, L. J., "Design and performance of GMR sensors for the detection of magnetic microbeads in biosensors," *Sensors and Actuators A*, **107**, 309-218 (2003).

15 Baselt, D. R., Lee, G. U., Natesan, M., Metzger, S. W., Sheehan, P. E., Colton, R. J., "A biosensor based on magnetoresistance technology", *Biosensors and Biolectronics*, **13**, 731-739 (1998).

16 Burns, M. A., et. al. *Proc. Natl. Acad. Sci. U. S. A.*, **93**, 5556 (1996).

17 Illic, B., Czaplewski, D., Craighead, H. G., Neuzil, P., Campagnolo, C., Batt, C., "Mechanical resonant immunospecific biological detector", *Applied Physics Letters*, **77**, 450-452 (2000).

18 Nicu, L, Bergaud, C. "Modeling of a tuning for biosensor based on the excitation of one particular resonance mode," *Journal of Micromechanics and Microengineering*, **14**, 727-736 (2004).

19 Hwang, K. S., Lee, J. H., Park, J., Yoon, D. S., Park, J. H., Kim, T. S., "In-situ quantitative analysis of a prostate-specific antigen (PSA) using a nanomechanical PZT cantilever," *Lab on a Chip*, **4**, 547-552 (2004).

20 Baselt, D. R., Lee, G. U., Hansen, K. M., Chrisey, L. A., Colton, R. J., "A High-Sensitivity Micromachined Biosensor", *Proceedings of the IEEE*, **85**, 672-680 (1997).

21 Pandey, S., Mehrotra, R., Wykosky, S., White, M. H., "Characterization of a MEMS BioChip for planar patch-clamp recording", *Solid-State Electronics*, 2061-2066 (2004).

22 Luff, B. J., Wilkinson, J. S., Piehler, J., Hollenbach, U., Igneghoff, J., Fabricius, N., "Integrated Optical Mach-Zehnder Biosensor", **16**, 583-592 (1998).

23 Homola, J., "Present and future of surface plasmon resonance biosensors", *Analytical and Bioanalytical Chemistry*, **377**, 528-539 (2003).

24 Verpoorte, E. "Chip vision – optics for microchips", *Lab-on-a-Chip*, **3**, 42N-52N (2003).

25 Burns, M. A., Johnson, B. N., Brahmasandra, S. N., Handique, K., Webster, J. R., Krishnan, M., Sammarco, T. S., Man, P. M., Jones, D., Heldsinger, D., Mastrangelo, C. H., Burke, D. T., "An Integrated Nanoliter DNA Analysis Device", *Science*, **282**, 484-487 (1998).

26 Baslev, S., Bilenberg, B., Geschke, O., Jorgensen, A. M., Kristensen, A., Kutter, J. P., Mogensen, K. B., Snakenborg, D., "Fully Integrated Optical System for Lab-on-a-Chip Applications", Mikroelektronik Centret (MIC), Technical University of Denmark (DTU).

27 Helbo, B., Kristensen, A., Menon, A., "A micro-cavity fluidic dye laser", *Journal of Micromechanics and Microengineering*, **13**, 307-311 (2003).

28 Mogensen, K. B., Petersen, N. J., Hubner, J., Kutter, J. P., "Monolithic integration of optical waveguides for absorbance detection in microfabricated electrophoresis devices", *Electrophoresis*, **22**, 3930-3938 (2001).

29 Liang, Z., Chiem, N., Ocvirk, G., Tang, T., Fluri, K., and Harrison, J. D., "Microfabrication of a Planar Absorbance and Fluorescence Cell for Integrated Capillary Electrophoresis Devices", *Analytical Chemistry*, **68**, 1040-1046 (1996).

30 Roulet, J-C., Volkel, R., Herzig, H. P., Verpoorte, E., de Rooij, N. F., and Dandliker, R., "Performance of an Integrated Microoptical System for Fluorescence Detection in Microfluidic Systems", *Analytical Chemistry*, **74**, 3400-3407 (2002).

31 Kruger. J., Singh, K., O'Neill, A., Jackson, C., Morrison, A., O'Brien, P., "Development of a microfluidic device for fluorescence activated cell sorting", *Journal of Micromechanics and Microengineering*, **12**, 486-494 (2002).

32 Cui, L., Zhang, T., Morgan, H., "Optical particle detection integrated in a dielectrophoretic lab-on-a-chip", *Journal of Micromechanics and Microengineering*, **12**, 7-12 (2002).

33 Lin, C.-H., Lee, G.-B., "Micromachined flow cytometers with embedded etched optic fibers for optical detection", *Journal of Micromechanics and Microengineering*, **13**, 447-453 (2003).

34 Hubner, J., Mogensen, K. B., Jorgensen, A. M., Friis, P., Telleman, P., Kutter, J. P., "Integrated Optical measurement system for fluorescence spectroscopy in microfluidic channels", *Review of Scientific Instruments*, **72**, 229-233 (2001).

35 Camou, S., Fujita, H., Fugii, T., "PDMS 2D optical lens integrated with microfluidic channels: principle and characterization", *Lab-on-a-Chip*, **3**, 40-45 (2003).

36 Kumar, A., "Features of gold having micrometer to centimeter dimensions can be formed through a combination of stamping with an elastomeric stamp and alkanethiol "ink" followed by chemical etching", *Applied Physics Letters*, **63**, 2002-2004 (1993).

37 Kane, R. S., Takayama, S., Ostuni, E., Ingber, D. E., Whitesides, G. M., "Patterning Proteins and cells using soft lithography", *Biomaterials*, **20**, 2363-2376 1999.

38 Waits, C. M., Modafe, A., Ghodssi, R., "Investigation of Gray-scale Technology for Large Area 3-D Silicon MEMS Structures", *Journal of Micromechanics and Microengineering*, **13**, 170-177 (2003).

39 Wu, L.-Q., Gadre, A., Yi, H., Kastantin, M., Rubloff, G. W., Bentley, W. E., Payne, G. F., Ghodssi, R., "Voltage-Dependent Assembly of the Polysaccharide Chitosan onto an Electrode Surface", *Langmuir*, **18**, 8620-8625 (2002).

40 Wu, L.-Q., Yi, H., Li, S., Rubloff, G. W., Bentley, W. E., Ghodssi, R., Payne, G. F., "Spatially Selective Deposition of a Reactive Polysaccharide Layer onto a Patterned Template", *Langmuir*, **19**, 519-524 (2003).

41 Hyunmin Yi. Private Communication.

42 Yi, H., Wu, L.-Q., Ghodssi, R., Rubloff, G. W., Payne, G. F., Bentley, W. E., "Signal-Directed Sequential Assembly of Biomolecules on Patterned Surfaces", *Langmuir*, **21**, 2104-2107 (2005).

43 Chen, T., Small, D. A., Wu, L.-Q., Rubloff, G. W., Ghodssi, R., Vazquez-Duhalt, R., Bentley, W. E., Payne, G. F., "Nature-Inspired Creation of Protein-Polysaccharide Conjugate and Its Subsequent Assembly onto a Patterned Surface", *Langmuir*, **19**, 9382-9386 (2003).

44 Graham, C. R., Leslie, D., Squirrell, D. J., "Gene Probe Assays on a Fibre-Optic Evanescent Wave Biosensor", *Biosensors and Bioelectronics*, **7**, 487 (1992).

45 Hyunmin Yi, Private Communication

46 http://en.wikipedia.org/wiki/Image:DeoxyriboseLabeled.png, Accessed 13 July 2005.

47 Brown, Le May, Bursten, Chemistry: The Central Science Eighth Edition, Prentice Hall, Upper Saddle River, NJ, (2000)

48 Valeur, B. Molecular Fluorescence Principles and Applications, Wiley-VCH, Weinheim, Germany 2002.

49 NIST Chemistry Webbook (http://webbook.nist.gov/chemistry/) Accessed: 7 August 2005

50 Haughland, R. P., <u>Handbook of Molecular Probes and Research Products, Ninth Edition</u>, Molecular Probes, Eugene OR (2002).

51 Parker, C. A., <u>Photoluminescence of Solutions</u>, Elsevier, Amsterdam, 1968

52 Du, H., Strohsahl, C. M., Camera, J., Miller, B. L., Krauss, T. D., "Sensitivity and Specificity of Metal Surface-Immobilized 'Molecular Beacon' Biosensors", *Journal of the American Chemical Society*, **127**, 7932-7940 (2005).

53 Du, H., Disney, M. D., Miller, B. L., Krauss, T. D., "Hybridization-Based Unquenching of DNA Hairpins on Au Surfaces: Prototypical 'Molecular Beacon' Biosensors", *Journal of the American Chemical Society*, **125**, 4012-4013 (2003).

54 Thorsen, Todd, S. Maerkl, S. Quake, "Microfluidic Large-Scale Integration", *Science*, **298**, 580-584 (2002).

55 Hayt, W. H., Buck, J. A., <u>Engineering Electromagnetics, 6th Edition</u>, McGraw Hill, Boston, 2001.

56 C. C. Davis, <u>Lasers and Electro-Optics: Fundamentals and Engineering</u>, Cambridge University Press, 1995.

57 Saleh, <u>Fundamentals of Photonics</u>, Wiley, New York, 1991.

58 Keiser, G. <u>Optical Fiber Communications, 3rd Edition</u>, McGraw-Hill, Boston, 1999

59 Hecht, E., <u>Optics 3rd Edition</u>, Addison-Wesley, Reading Massachuttsets, 1998

60 Pedrotti and Pedrotti <u>Introduction to Optics, 2nd Edition</u>, Prentice-Hall, Upper Saddle River, NJ, 1993.

61 Wolf, S., Giehl, A. R., Renno, M., Fouckhardt, H., "Metallic waveguide mirrors in polymer film waveguides", *Applied Physics B: Lasers and Optics*, **73**, 623-627 (2001).

62 Leeds, A. R., Van Keuren, E. R., Durst, M. E., Schneider, T. W., Currie, J. F., Paranjape, M., "Integration of microfluidic and microoptical elements using a single-mask photolithographic step", *Sensors and Actuators A: Physical*, **115**, 571-580 (2004).

63 P. C. D. Hobbs, <u>Building Electro-Optic Systems: Making it all work</u>, Wiley, New York, 2000.

64 Brewer Science, www.brewerscience.com

65 Dow Corning Corporation, www.cyclotene.com

66 Microchem Corp. www.microchem.com

67 PMMA Optical Properties, Unknown (2004).

68 Scott Horst. Private Communication.

69 N.LaBianca, J.D. Gelorme, "High aspect ratio resist for thick film applications", *Proceedings of the SPIE*, 1995, **2438**, 846-852.

70 Li, S., Friedhoff, C. B., Young, Y. M., Ghodssi, R., "Fabrication of Micronozzles with Low Temperature Wafer Bonding with SU-8", *Journal of Micromechanics and Microengineering*, **13**, 732-738 (2003).

71 Helbo, B., Kristensen, A, Menon, A. "A micro-cavity fluidic dye laser", *J. Micromech Microeng.*, **12**, 307-311 (2003).

72 Mogensen, K, J. El-Ali, A. Wolff, J. P. Kutter, "Integration of polymer waveguides for optical detection in microfabricated chemical analysis systems", *Applied Optics*, **42**, 4072-4079 (2003).

73 Wikipedia CTE data. www.wikipedia.org. Accessed Fall 2005.

74 Schleunitz, Arne. Studienarbeit: "Fabrication and Characterization of SU-8 Waveguides for Optical Integrated BioMEMS with Sensing Application". University of Maryland and The Technical University of Berlin.

75 Silicon Resources. Private Communication.

76 Bashar, Shabbir A., Study of Indium Tin Oxide (ITO) for Novel Optoelectronic Devices, Ph.D. Thesis, King's College of London, 1998.

77 Hamberg, I., Granqvist, C. G., "Transparent and infrared-reflecting indium-tin-oxide films: quantitative modeling of the optical properties," *Applied Optics*, **24**, 1815-1819 (1985).

78 Gordon, R., "Criteria for Choosing Transparent Conductors", MRS Bulletin, 52-57 August 2002.

79 Wu, W-F., Chiou, B-S., "Effect of oxygen concentration in the sputtering ambient on the microstructure, electrical, and optical properties of radio-frequency magnetron-sputtered indium tin oxide films", *Semiconductor Science and Technology*, **11**, 196-202 (1996).

80 Nigel Shepard (ARL). Private Communication.

81 Rottman, M., Heckner, K.-H., "Electrical and structural properties of indium tin oxide films deposited by reactive DC sputtering", *Journal of Physics D: Applied Physics,* **28**, 1448-1543 (1995).

82 Chen, H., Qiu, C., Wong, M., Kwok, H-S., "DC Sputtered Indium-Tin-Oxide Transparent Cathode for Organic Light-Emitting Diode", *IEEE Electron Device Letters*, **24**, 315-317 (2003).

83 Dill, F. H., et. al. *IEEE Transactions on Electronic Devices*, **ED22**, 445 (1975).

84 Elaine Kokinda, AZ Electronic Materials USA, Private Communication 1 April 2005

85 Park, J. J. et. Al. "BioMEMS Chip and Package Design for Surface-Controlled Bioreaction Processes", AVS 52nd International Symposium, Boston, October 30 – November 4 2005.

86 Stephan T. Koev, Michael A. Powers, Hyunmin Yi, Li-Qun Wu, William E. Bentley, Gary W. Rubloff, Gregory F. Payne, and Reza Ghodssi, *Mechano-Transduction of Chemical and Biochemical Events Through Electrodeposited Chitosan Network*, Lab-on-a-Chip, Submitted for Review, June 2006

87 Bass, M. et. al., Handbook of Optics, Volume IV, 2nd Ed., Fiber Optics and Nonlinear Optics, Section 1.6, Optical Society of America, Mc-Graw Hill Professional, Boston, 2000.

88 Sigma-Aldrich (www.sigma-aldrich.com) PerfectHyb Product Information. Accessed 4 September 2005

89 M. W. Pruessner, K. Amarnath, M. Datta, D. P. Kelly, S. Kanakaraju, P.-T. Ho, and R. Ghodssi, *"InP-Based Optical Waveguide MEMS Switches With Evanescent Coupling Mechanism"*, Journal of Microelectromechanical Systems, **14**, 1070-1081 (2005).

90 Blair, S., Chen, Y., "Resonant-enhanced evanescent-wave fluorescence biosensing with cylindrical optical cavities", *Applied Optics*, **40**, 570-582 (2001).

91 Srivastava, R., Bao, C., Gomez-Reino, C., "Planar-surface-waveguide evanescent-wave chemical sensors", *Sensors and Actuators A*, **51**, 165-171 (1996).

92 Kruger, J., Singh, K., O'Neill, A., Jackson, C., Morrison, A., O'Brien, P., "Development of a microfluidic device for fluorescence activated cell sorting", *Journal of Micromechanics and Microengineering,* **12**, 486-494 (2002).

93 Yeh, H.-J., Smith, J. S., "Fluidic Self-Assembly for the Integration of GaAs Light-Emitting Diodes on Si Substrates", *IEEE Photonics Technology Letters*, **6**, 706-708 (1994).